Terahertz laser radiation induced optoelectronic phenomena in HgTe-based topological insulators and graphene

Dissertation

zur Erlangung des Doktorgrades
der Naturwissenschaften (Dr. rer. nat.)
der Fakultät für Physik
der Universität Regensburg

vorgelegt von

Susanne Candussio

aus Vilshofen a. d. Donau

im Jahr 2022

Promotionsgesuch eingereicht am: 02.05.2022

Die Arbeit wurde angeleitet von: Prof. Dr. Sergey D. Ganichev

Prüfungsausschuss

Vorsitzender: Prof. Dr. Milena Grifoni
1. Gutachter: Prof. Dr. Sergey D. Ganichev
2. Gutachter: Prof. Dr. Christian Schüller
weiterer Prüfer: Prof. Dr. Jörg Wunderlich

Contents

1 Introduction

Two-dimensional systems with a linear energy momentum relation own unique electronic properties [1–4]. Their electrons behave like ultrarelativistic massless Dirac fermions and are protected against disorder in the absence of a magnetic field [5]. These qualities open a way to the study of interesting physics and applications, e.g. Majorana fermions [1, 6, 7], Klein tunnelling [3, 8], the quantum spin Hall effect [2, 9], or novel ultrafast detectors [10, 11]. To describe these unique systems, the Dirac equation [12] is used rather than the non-relativistic Schrödinger equation. Efforts in this field of research have led to the realisation of two remarkable material classes, namely graphene and topological insulators [5].

The first realization of a solid state material with linear dispersion was graphene [4], a two-dimensional allotrope of carbon, which hosts massless Dirac fermions [3, 4, 13]. The charge carriers move with a velocity of 10^6 m/s which is 1/300 of the speed of light. Importantly, this velocity is independent of the carrier energy, which is usually only the case for photons or neutrinos [5]. Stacking two coupled layers of graphene, called bi-layer graphene, results in a material with parabolic dispersion and massive Dirac fermions. An important feature of this material is that the band structure can be simply changed by application of an external electric field. The ease of this tunability makes bi-layer graphene a promising two-dimensional material for future applications [4, 14–16].

Another material class in which linear dispersion has been realized are topological insulators. Similar to graphene these systems can be described within the Dirac theory for massless particles. However, the spin-orbit interaction is fairly large in topological insulators while it is vanishingly small in graphene. Topological insulating materials exhibit a bulk energy gap like an ordinary insulator but have perfectly conducting edge or surface states which are characterized by a linear energy dispersion [1, 2, 17–19]. Importantly, the momentum of the carriers residing at the boundaries is locked to their spin because of the strong spin-orbit coupling, resulting in a counterpropagation of states with oppositely directed spins [1]. In line with this fact, backscattering is forbidden yielding rather high carrier mobilities. These may play a role for the development of novel electronic, optic and optoelectronic applications [1, 20].

Optoelectronic phenomena induced by terahertz radiation provide highly effective means for the characterization of such Dirac fermion systems [21–28].

In these effects the photoresponse is proportional to higher orders of the electric field and, therefore, they are termed as nonlinear. Illumination of the materials may result in the generation of a photocurrent or a change in the sample's conductivity. Particular examples are second harmonic generation, the photogalvanic and photon drag effect, photothermoelectrics, and ratchet effects [29]. The present thesis is aimed to the study of nonlinear optoelectronic phenomena induced by terahertz radiation in topological insulators and graphene. Within this work, the observation of new phenomena are presented, which provide a useful tool to study characteristic material properties. These include: cyclotron resonance of surface states in topological insulators [30], edge photocurrents in mono- and bi-layer graphene [31, 32], resonant edge photocurrents in bi-layer graphene [33] and a circular Hall effect in the absence of a magnetic field [34].

In the first part of this thesis cyclotron-resonance-induced photocurrents in partially strained 200 nm HgTe-based heterostructures were studied. It is well known that by application of strain to bulk HgTe a gap opens in the otherwise gapless semimetal. The two-dimensional surface states can be decoupled from the bulk states and, thus, strained HgTe can be considered as a three-dimensional topological insulator [17, 35–37]. The detection of cyclotron resonance in a strained HgTe film can be used to reveal information that are explicitly about the surface, since bulk and surface carriers have different cyclotron masses [38, 39]. The present work demonstrates that applying this technique to thicker 200 nm HgTe films, resonant photocurrents of both top and bottom surfaces can be observed; although the strain is expected to relax between a film thickness of 100 nm and 200 nm. In addition, their characteristics are similar to those of the surface states of fully strained 80 nm HgTe films [38]. These results are in line with recent magnetotransport and capacitance measurements [40].

The study on cyclotron resonance and other optoelectronic phenomena was extended to graphene-based devices. Since electronic and transport properties of two-dimensional materials are strongly influenced by their edges, it is important to take a closer look on edge effects excited by terahertz radiation. Therefore, photocurrents flowing along the edges of mono- and bi-layer graphene were studied. The current generation belongs to the class of second order electric field phenomena and originates from the alignment of the carrier momenta and P-symmetry breaking at the edges. In bi-layer graphene exposed to a magnetic field, giant resonant edge photocurrents were observed

which are superimposed by $1/B$-periodic oscillations at high carrier densities. It was shown, that the resonances stem from inter and intra Landau level transitions, where the latter ones can be associated with classical cyclotron resonance.

All effects described above scale with the second power of the radiation's electric field. Phenomena proportional to the third order allow a new access to material properties. Within the study of mono-layer graphene, a helicity-dependent photoconductivity signal, normal to the applied bias voltage, was observed which can be controlled by a back gate. The dc Hall effect manifests the time-inversion symmetry breaking induced by the circularly polarized radiation in the absence of a magnetic field. The observed Hall photoconductivity shows a surprising intensity dependence: For low gate voltages the signal is proportional to the radiation intensity, while at higher voltages it varies with the square of it.

The thesis is structured in the following way: In Chap. 2, fundamental principles and phenomena are outlined. It starts with an introduction of the Dirac equation in Sec. 2.1 allowing the description of systems with spin 1/2 particles. On the basis of this, the investigated material classes are depicted. Firstly, in Sec. 2.1.2 HgTe-based topological insulators are introduced. This includes the general depiction of two- and three-dimensional topological insulators and their description within the modified Dirac theory in the zero-mass limit. Secondly, in Sec. 2.1.3 the crystalline and electronic structure of graphene is outlined. The electronic properties of bi-layer graphene are depicted in Sec. 2.1.4. Chapter 2.2 gives a brief description of cyclotron resonance in systems with parabolic and linear dispersion. Furthermore, Chap. 2.3 presents an overview of optoelectronic phenomena which may be induced by terahertz radiation. The description of the experimental methods, given in Chap. 3, starts with the investigated samples in Sec. 3.1 and their characteristic transport properties. Section 3.2 is dedicated to the laser systems and electronic setups employed in this work.

The presentation of the experimental findings begins in Chap. 4 with the data obtained for HgTe topological insulators. The experimental results presented in Sec. 4.1 include photocurrents measured in 200 nm HgTe films which are stongly enhanced under cyclotron resonance. Furthermore, the magneto-transmission is studied and analysed. The discussion of these results is given in Sec. 4.2. In Chap. 5 results on edge photocurrents in mono- and bi-layer graphene are provided. It starts with a presentation of the data for mono-layer

graphene samples in Sec. 5.1. After this, the observed edge photocurrents in bi-layer graphene are presented in Sec. 5.2. The subsequent discussion is given in Sec. 5.2.2. Section 5.3 presents the experimental findings for edge photocurrents resulting from inter and intra Landau level transitions in bi-layer graphene. The discussion of the data, given in Sec. 5.3.2, deals with the identification of the transitions within the Landau level spectrum and gives a brief introduction to the microscopic theory describing the photocurrent generation. In Chap. 6, the results on the circular Hall effect in graphene arising in the absence of a magnetic field are shown. The analysis of the experimental observations is outlined in Sec. 6.2. In the last chapter, Chap. 7, the work is summarized and a short outlook for further studies in this field is given.

2 Fundamentals

2.1 Dirac fermion systems

This section is dedicated to the description of the investigated material classes. It starts with the introduction of the Dirac equation describing massive spin 1/2 particles [4, 14, 41]. On this basis, the studied material systems are described beginning with HgTe-based topological insulators (HgTe TI) which exhibit strong spin-orbit coupling. Then, the electronic and crystalline structures of graphene are outlined which, unlike HgTe, has vanishing spin-orbit interaction and posses a pseudospin. Although these two materials have different properties, the electrons in both systems manifest a linear dispersion relation and can be described by the Dirac equation in the zero-mass limit [1, 3, 14, 42]. In contrast, bi-layer graphene, whose crystalline and electronic structure is introduced in the last section of this chapter, has a parabolic dispersion and hosts massive Dirac fermions [14–16].

2.1.1 The Dirac equation

In the year 1928 Paul A.M. Dirac wrote down a relativistic wave equation describing elementary particles which posses a spin of $\frac{1}{2}$. This equation is known as the Dirac equation [12, 43]. It can be found by linearization of the general relativistic classical Schrödinger equation [44] and is given by [12, 43]

$$H = c\boldsymbol{p} \cdot \boldsymbol{\alpha} + mc^2\beta \tag{1}$$

with the particle mass m, the momentum operator $\boldsymbol{p}$, the speed of light c and the Dirac matrices α_i and β. The latter ones are given by [43, 44]

$$\alpha_i = \begin{pmatrix} 0 & \sigma_i \\ \sigma_i & 0 \end{pmatrix}, \beta = \begin{pmatrix} \mathbf{1}_2 & 0 \\ 0 & -\mathbf{1}_2 \end{pmatrix} \tag{2}$$

with the 2×2 identity matrix $\mathbf{1}$. The components of the spinoperator $\boldsymbol{\sigma}$ are the 2×2 Pauli matrices [43]

$$\sigma_x = \begin{pmatrix} 0 & 1 \\ 1 & 0 \end{pmatrix}, \sigma_y = \begin{pmatrix} 0 & -i \\ i & 0 \end{pmatrix}, \text{ and } \sigma_z = \begin{pmatrix} 1 & 0 \\ 0 & -1 \end{pmatrix}. \tag{3}$$

This shows that in three dimensions the Dirac matrices are at least four dimensional. Corresponding energy eigenvalues are [43]

$$E_{\pm} = \pm\sqrt{m^2c^4 + p^2c^2} \tag{4}$$

yielding four possible solutions of the Dirac equation. The two positive solutions correspond to the description of electron-states with spin up and spin down. The two negative solutions describe positrons, the electrons' antiparticles, with spin up and spin down.

The positive and negative energy states are separated by an energy gap of $2mc^2$ [43]. In vacuum all negative energy states are filled, while only one positive energy state is occupied. If the energy gap closes, i.e. $m \to 0$, then the energy dispersion reduces to $E(m \to 0) = \pm|cp|$ which is linear in c and p. This limit is described by the Weyl equation [45], which evolves from the reduction of the Dirac equation. The Dirac equation is invariant under transformations $m \to -m$ if $\beta \to -\beta$ which satisfies the mutual anticommutation relations. This indicates that the equation is symmetric in its positive and negative energy solutions [43].

2.1.2 HgTe-based topological insulators

After the introduction of the Dirac formalism, in the following an example of its implementation in condensed matter physics will be given. Topological insulators have a bulk energy gap which separates the highest occupied electronic band from the lowest empty band. At the edges, or on the surface, however, gapless states exist which are protected against disorder by time-reversal ($\mathcal{T}$) symmetry [1].

A two-dimensional (2D) topological insulator is also known as a quantum spin Hall insulator. In systems exhibiting the quantum spin Hall effect, the spin-up states propagate in a different direction than the spin-down states resulting from spin-momentum locking. These states are called helical edge states [1, 9] and differ from the chiral edge states existing in the quantum Hall effect where up and down states propagate in the same directions [1, 46]. These one-dimensional (1D) helical edge states evolve to 2D surface states in the case of a three-dimensional (3D) topological insluator. The bulk band structure of topological insulators is similar to an ordinary insulator, with an energy band gap separating the conduction and the valence band. In contrast, in the vicinity of the boundary to a trivial insulator, gapless surface states

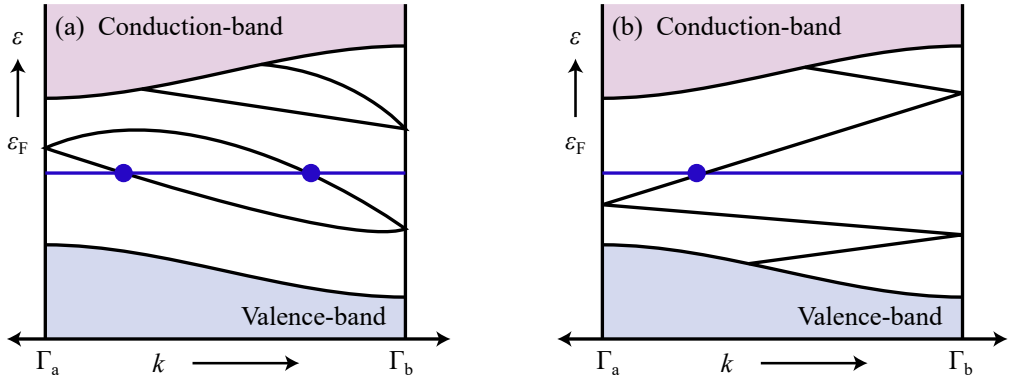

Figure 1: Dispersion relation between two Kramers degenerate points $\Gamma_a = 0$ and $\Gamma_b = \pi/a$ at the boundary of a $\mathcal{T}$ invariant 2D insulator. The shaded regions illustrate the bulk conduction and valence band. (a) The bands cross the Fermi energy an even number of times. (b) An odd number of Fermi energy crossings leads to topologically protected conducting states at the boundary. Note that only one half of the Brillouin zone is shown, because the other half is just mirrored due to time-reversal symmetry. Adapted from Ref. [1].

with a momentum locked to the electron spin exist with energies that lie in the bulk energy gap [43]. A topological insulator is invariant under $\mathcal{T}$.

In 2D topological insulators, $\mathcal{T}$ symmetry is described by an antiunitary operator Θ which for spin 1/2 electrons fullfills $\Theta^2 = -1$. From this follows that all eigenstates of the corresponding Hamiltonian have to be at least twofold degenerate. This is known as Kramer's theorem and results from the following assumption. Imagine a nondegenerate state $|\chi\rangle$ would exist, this would mean $\Theta|\chi\rangle = c|\chi\rangle$ with c being some constant. This yields $\Theta^2|\chi\rangle = |c|^2|\chi\rangle$ which is not allowed since $\Theta^2 = -1$ and $|c|^2 \neq -1$ [1]. In systems without spin-orbit coupling Kramer's theorem simply describes the degeneracy of spin-up and spin-down states. In contrast, in systems with spin-orbit coupling this means that there always exists a pair of states at a certain energy that have opposite spin and momenta [1, 43] making the states resistant against backscattering. Figure 1 illustrates the electronic dispersion between two Kramers degenerate points, $\Gamma_a = 0$ and $\Gamma_b = \pi/a$, at the edge of a 2D insulator which is invariant under $\mathcal{T}$ reversal. Here, an energy gap separates the bulk conduction and valence band. The states existing at the edge of the insulator must fullfill Kramer's theorem, i.e. they have to be twofold degenerate at the $\mathcal{T}$ invariant points $\Gamma_a = 0$ and $\Gamma_b = \pi/a$. Away from these momenta the spin-orbit interaction will split the degeneracy. Two cases can be distinguished: In the

first case, shown in Fig. 1(a), the states at Γ_a and Γ_b connect pairwise and cross the Fermi energy ε_{F} an even number of times, while in the second case, Fig. 1(b), the bands cross ε_{F} an odd number of times. The latter results in topologically protected conducting edge states.

In the case of 3D topological insulators the Fermi circle encloses an odd number of Kramers degenerate points, which in the simplest case is a single Dirac cone. These surface states form a perfectly conducting 2D plane [47]. However, different to an ordinary metal these states are not spin degenerate. $\mathcal{T}$ symmetry forces the spins to rotate around the Fermi surface.

Modified Dirac theory The Dirac equation reveals that at the interface between two media with positive and negative mass a pair of helical bound states exist. However, in its raw form it cannot be used to describe topological insulators due to its symmetry between the negative and positive masses (or energy gaps). This makes it impossible to distinguish which state is topologically trivial or non-trivial. To overcome this problem a modified Dirac Hamiltonian with a quadratic correction $-B\boldsymbol{p}^2$ to the mass-term is introduced [42]

$$H = v\boldsymbol{p}\cdot\alpha + (mv^2 - B\boldsymbol{p}^2)\beta \tag{5}$$

where mv^2 defines the particle's band gap and m and v are the mass and speed, respectively. This introduced quadratic term breaks the symmetry of the Dirac equation regarding positive and negative masses.

To find bound state solutions to the modified Dirac equation in two dimensions, the modified Hamiltonian (Eq. (5)) is separated into two independent equations given by [42]

$$h_{\pm} = vp_x\sigma_x \pm vp_y\sigma_y + (mv^2 - Bp^2)\sigma_x. \tag{6}$$

This yields a one dimensional model for the helical edge states in two dimensions. At $x = 0$ the dispersion relation for the bound states is given by [43, 48]

$$\varepsilon_{p_y,\pm} = \pm vp_y\mathrm{sgn}(B), \tag{7}$$

which shows that the two bound states have opposite velocities and form a pair of helical edge states. To distinguish a topologically trivial system from

a nontrivial one, in two dimensions the Chern number is used. In relation to the Hall conductance $\sigma_\pm = n_\pm e^2/h$ the Chern number $n_\pm$ is given by [49, 50]

$$n_\pm = \pm(\mathrm{sgn}(m) + \mathrm{sgn}(B))/2. \tag{8}$$

Here, two cases can be distinguished. If m and B have opposite sign, then $n_\pm = 0$ describing a topologically trivial system. The other case, where m and B have the same sign, refers to a topologically non-trivial system. This describes the bulk-edge relation of the integer quantum Hall effect [43, 51].

In three dimensions the modified Dirac Hamiltonian for a yz-plane at $x = 0$ is given by [42]

$$H_{3\mathrm{D}} = vp_y\alpha_y + vp_z\alpha_z - B(p_y^2 + p_z^2)\beta \tag{9}$$

The corresponding gapless dispersion relation for two-dimensional surface states is found as

$$\varepsilon_{p,\pm} = \pm vp\,\mathrm{sgn}(B) \tag{10}$$

with $p = \sqrt{p_y^2 + p_z^2}$. This describes an effective model for a single Dirac cone on the surface of a topologically nontrivial system.

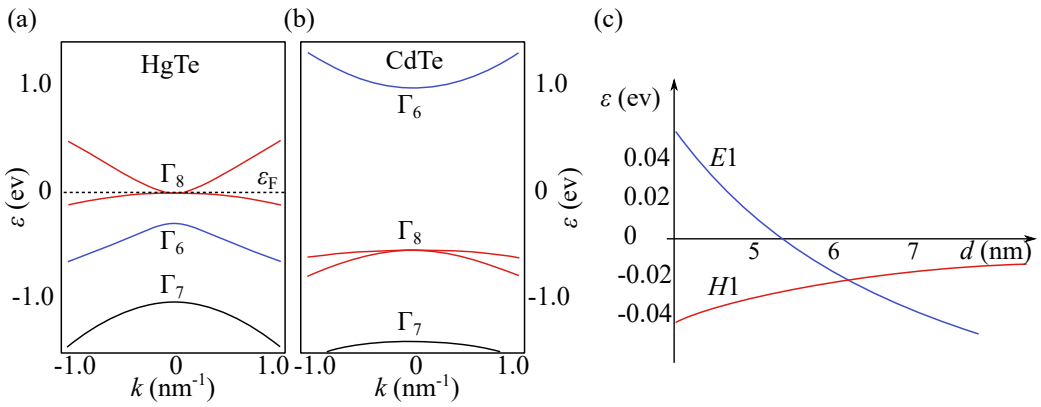

Figure 2: Bulk band structure for (a) HgTe having an inverted band ordering and (b) CdTe having a normal band ordering. The Fermi energy ε_F is illustrated as dashed line in panel (a). (c) Energy of the $E1$ and $H1$ band as a function of the HgTe thickness. Adapted from Ref. [52]

2.1.2.1 HgCdTe topological insulators Materials made of heavy elements, i.e. with strong spin-orbit coupling, are good candidates for realisation of topological insulators. In 2006, Bernevig, Hughes, and Zhang [52] proposed a quantum spin Hall insulator consisting of HgCdTe quantum wells. Soon after the prediction the experimental realisation followed by König et al. [53].

Both, HgTe and CdTe have a zinc-blende lattice structure. The existence of two types of atoms reduces the point group symmetry from O_h to T_d where the inversion symmetry is broken [54]. In both materials the energy gap is smallest near the Γ-point in the Brillouin zone, see Fig. 2. The band structure of the barrier material CdTe contains a s-type (Γ_6) conduction band separated from the p-type valence bands (Γ_7 and Γ_8) by a gap of approximately 1.6 eV, see Fig. 2(b). The well material HgTe has an inverted band structure where the conduction band is formed by the light-hole (LH) bulk subband of the Γ_8 band and the first valence band by its heavy-hole (HH) subband, see Fig. 2(a). The s-type Γ_6 band lies below the Γ_8 band and above the Γ_7 band [52]. HgTe can be viewed as a zero-gap semiconductor because of the degeneracy of the Γ_8's heavy- and light-hole band at the Γ-point [54]. From this follows the unique property of HgTe quantum wells that the band structure can be tuned by the well thickness. Figure 2(c) illustrates the band alignment with increasing HgTe thickness. Note that $H1$ and $E1$ are two QW subbands which are formed from the Γ_6 and Γ_8 bulk bands. $H1$ denotes the hole like band formed from the Γ_8 HH bulk states, whereas $E1$ is the electron like band formed from the Γ_6 and the Γ_8 LH bulk states [52]. For a quantum well thicknesse smaller than the so called critical thickness d_c, the confinement is rather high and the band structure is more similar to CdTe, i.e. the quantum wells exhibit a normal band ordering where $E1 > H1$. By increasing the QW thickness the material behaves more like HgTe, and thus has an inverted band structure, where $H1 > E1$. In between, a critical thickness exists where the two bands $E1$ and $H1$ cross [54].

An important parameter to describe the band ordering is the mass term in the Dirac equation giving the energy gap between the two bands, see Eq. (1). In two-dimensional materials with inverted band structure $m < 0$, whereas in those with a normal band ordering $m > 0$. This means that the Dirac mass parameter in HgTe quantum wells can be tuned from $m > 0$ for a thickness $d < d_c$ to $m < 0$ for $d > d_c$. At the crossing point of the two bands, the mass term changes its sign and a quantum phase transitions occurs [52, 54]. Here,

the system can be effectively described by the massless Dirac theory, similar to graphene.

2.1.3 Graphene

Graphene, well known for the existence of massless Dirac fermions, exhibits a vanishing spin-orbit interaction in strong contrast to the above described HgTe topological insulators. Its first experimental realisation was accomplished in 2004 by the group around A. K. Geim from the University of Manchester [4]. The first calculations on its electronic band structure, however, were already performed around 1946 by Wallace [55]. Due to its intriguing properties, graphene became an active field of research in condensed matter physics [56]. In the following its crystalline structure as well as its fundamental electronic properties are outlined.

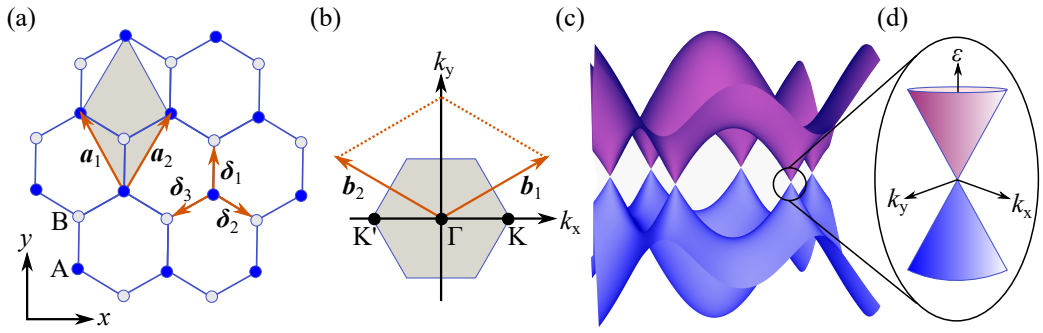

Figure 3: (a) Hexagonal lattice structure of graphene with the two-atomic basis A and B in real space. The primitive cell is illustrated by the grey area spanned by two lattice unit vectors $\boldsymbol{a}_1$ and $\boldsymbol{a}_2$. The vectors $\boldsymbol{\delta}_i$ are the three nearest neighbour vectors. (b) First BZ with its centre Γ, the two non-equivalent corner points K and K', and the reciprocal vectors $\boldsymbol{b}_1$ and $\boldsymbol{b}_2$. (c) Energy spectrum of graphene with an enlargement (panel (d)) close to the Dirac points K and K', showing a Dirac cone. Panel (a) and (b) adapted from Ref. [3] and panels (c) and (d) adapted from Ref. [14].

Graphene consists of carbon atoms arranged on a hexagonal honeycomb structure, see Fig. 3(a). It can be considered as a triangular lattice with a basis consisting of two atoms per unit cell, A and B. The primitive cell vectors can be written as [3]

$$\boldsymbol{a}_1 = \frac{a}{2}(3, \sqrt{3}), \quad \boldsymbol{a}_2 = \frac{a}{2}(3, -\sqrt{3}) \tag{11}$$

with $a \approx 1.42\,\text{Å}$ being the distance between the carbon atoms. The nearest neighbour vectors are given by

$$\delta_1 = -a(1,0),\ \delta_2 = \frac{a}{2}(1,\sqrt{3}),\ \delta_3 = \frac{a}{2}(1,-\sqrt{3}). \tag{12}$$

The Brillouin zone (BZ) is shown in Fig. 3(b) with the reciprocal vectors being

$$\boldsymbol{b}_1 = \frac{2\pi}{3a}(1,\sqrt{3}),\ \boldsymbol{b}_2 = \frac{2\pi}{3a}(1,-\sqrt{3}). \tag{13}$$

Of particular importance are the points of high symmetry Γ, being the centre of the BZ, and the two points K and K', also called Dirac points, which lie at the corners of the BZ.

Within the tight-binding approach, which takes second-nearest neighbour hopping into account, the Hamiltonian for electrons in graphene in one of the sublattices is given by [1] [3]

$$\begin{aligned} H = &- t \sum_{\langle i,j\rangle,\sigma} (a^\dagger_{\sigma,i} b_{\sigma,j} + \text{h.c.}) \\ &- t' \sum_{\langle\langle i,j\rangle\rangle,\sigma} (a^\dagger_{\sigma,i} a_{\sigma,j} + b^\dagger_{\sigma,i} b_{\sigma,j} + \text{h.c.}). \end{aligned} \tag{14}$$

Here $a_{i,\sigma}$ and $a^\dagger_{i,\sigma}$ are annihilation and creation operators for electrons with spin σ ($\sigma = \uparrow, \downarrow$) and h.c. is the hermitian conjugate. The two energies t and t' correspond to the nearest neighbor (inter-sublattice) and next-nearest neighbor (intra-sublattice) hopping, respectively, and $t(\approx 2.8\,\text{eV}) > t'(\approx 0.1\,\text{eV})$ [3, 57]. The summation over the nearest and next-nearest neighbours is indicated by $\langle i,j\rangle$ and $\langle\langle i,j\rangle\rangle$, respectively. From the tight-binding Hamiltonian an analytical formula for the energy spectrum can be found

$$\varepsilon_\pm(\boldsymbol{k}) = \pm t\sqrt{3 + f(\boldsymbol{k})} - t' f(\boldsymbol{k}), \tag{15}$$

with

$$f(\boldsymbol{k}) = 2\cos\left(\sqrt{3}k_y a\right) + 4\cos\left(\frac{\sqrt{3}}{2}k_y a\right)\cos\left(\frac{3}{2}k_x a\right). \tag{16}$$

[1] Note that here units are chosen such that $\hbar = 1$.

Here (+) accounts for the π^* conduction band and (-) for the π valence band. Equation (15) shows that the energy is symmetric around zero in the case $t' = 0$. The resulting energy spectrum corresponding to Eq. (15) and with $t' = 0$ is shown in Fig. 3(c). Close to the Dirac points K and K', where conduction and valence band intersect, the dispersion exhibits a linear energy-momentum relation. A zoom in this region is shown in Fig. 3(d) illustrating a single Dirac cone. The almost universal equation for the band structure can be obtained from Eq. (15) close to the K (or K') point for small momenta relative to the Dirac points and $t' = 0$. With $\boldsymbol{k} = \boldsymbol{K} + \boldsymbol{q}$ where $|\boldsymbol{q}| \ll |\boldsymbol{K}|$ the energy is given by [3, 55]

$$\varepsilon_{\pm}(\boldsymbol{q}) \approx \pm v_{\mathrm{F}}|\boldsymbol{q}| + \mathcal{O}((q/K)^2) \tag{17}$$

with the relative momentum $\boldsymbol{q}$ and the Fermi velocity $v_{\mathrm{F}} \simeq 1 \times 10^6\,\mathrm{m/s}$ [55]. Strikingly, different to systems with parabolic dispersion, the Fermi velocity v_{F} is independent of energy or momentum [3].

Dirac theory The analogy between the description of the graphene electronic structure and the Dirac theory in the zero-mass limit is almost perfect. However, the Hamiltonian for electrons in graphene has distinguishing features. One of great importance is the Fermi velocity being 1/300 of the speed of light and the 2D nature of graphene [14]. The fact that the graphene lattice consists of two independent sublattices A and B indicates the existence of a chiral pseudo-spin analogous to the electron spin, however, completely independent of it. The two linear bands which cross at the Dirac points, see Fig. 3(d), become independent of each other [14]. The Hamiltonian for spinless charge carriers in graphene at the K point (valley) is given by [3, 14]

$$H_{\mathrm{K}} = v_{\mathrm{F}}\boldsymbol{\sigma} \cdot \boldsymbol{k} \tag{18}$$

with $\boldsymbol{\sigma} = (\sigma_x, \sigma_y)$ describing the pseudo-spin. The eigenfunctions $\psi(k)$ obeying the 2D Dirac equation for massless chiral Fermions in momentum space for K and K' points have the form [3]

$$\psi_{\pm,\mathrm{K}}(\boldsymbol{k}) = \frac{1}{\sqrt{2}}\begin{pmatrix} e^{-i\theta_k/2} \\ \pm e^{i\theta_k/2} \end{pmatrix},\ \psi_{\pm,\mathrm{K}'}(\boldsymbol{k}) = \frac{1}{\sqrt{2}}\begin{pmatrix} e^{-i\theta_k/2} \\ \pm e^{-i\theta_k/2} \end{pmatrix}, \tag{19}$$

being 2D pseudo-spinors. Here $\theta_k = \arctan(k_y/k_x)$ and the $\pm$ signs are attributed to valence and conduction band. In one of the two energy eigenstates the pseudo-spin is either parallel or anti-parallel to the momentum [56] following from the definition of helicity. Note that helicity is defined for the real spin, the coupling of the momentum to the pseudo-spin is called chirality. Therefore, in the K valley electrons have an opposite chirality than holes and the situation is reversed in the K' valley, making the chirality a good quantity to characterize the eigenfunctions [3].

Close to the Dirac points, the well defined chirality resulting from the intrinsic coupling of the carrier momentum to the pseudo-spin is a good quantum number. At higher energies and finite t' this description, however, becomes inappropriate [3].

2.1.4 Bi-layer graphene

Bi-layer graphene, previously shown to be a zero-gap semiconductor, owns unique properties [16, 58–60]. In particular, the possibility to open and control a band gap simply by applying a gate voltage to the system makes it a very promising material [16, 58]. To understand its remarkable properties, in the following bi-layer graphene's lattice structure and its electronic structure are introduced.

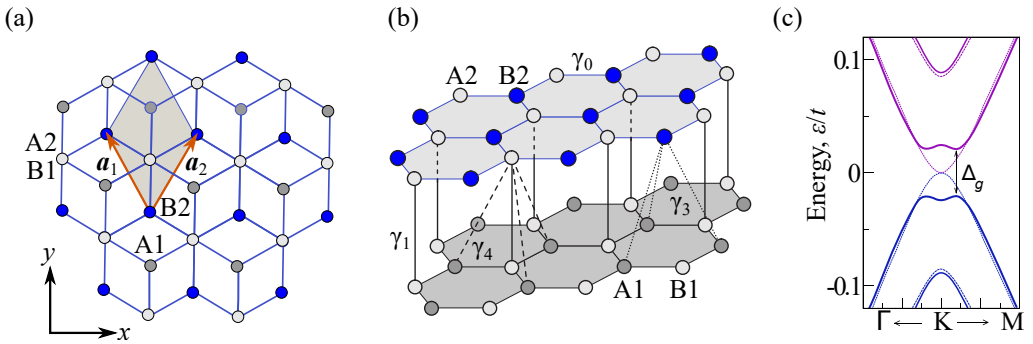

Figure 4: Lattice structure of bi-layer graphene: top view (panel (a)) and side view (panel (b)). A1/B1 and A2/B2 correspond to the atoms of the bottom/top layer. The unit cell with primitive lattice vectors $\boldsymbol{a}_1$ and $\boldsymbol{a}_2$ is illustrated by the shaded area. γ_i are the hopping parameters. Panel (a) and (b) are adapted from Ref [61]. (c) Band structure near the K (or K') point for $eV = 150\,\text{meV}$ (full line) and $V = 0$ (dashed line) with band gap Δ_g. Adapted from Ref. [62]

Bi-layer graphene consists of two coupled mono-layers of graphene where

each has a hexagonal lattice structure as shown above in Fig. 3(a). For AB Bernal stacking, the top layer (label 2) has its sublattice A on top of the sublattice B of the bottom layer (label 1). This is illustrated in Figures 4(a) and (b) showing the lattice structure of bi-layer graphene in top and side view, respectively. The corresponding unit cell owns twice the number of atoms as mono-layer graphene, while the primitive lattice vectors are equal (Eq. (11)) [58].

In the tight binding approximation, the relevant Hamiltonian H_{BLG} can be written as [3]

$$\begin{aligned} H_{\mathrm{BLG}} = &- \gamma_0 \sum_{\langle\langle i,j\rangle\rangle,m,\sigma} (a^\dagger_{m,i,\sigma} b_{m,j,\sigma} + \mathrm{h.c.}) \\ &- \gamma_1 \sum_{j,\sigma} (a^\dagger_{1,j,\sigma} a_{2,j,\sigma} + \mathrm{h.c.}) \\ &- \gamma_3 \sum_{j,\sigma} (a^\dagger_{1,j,\sigma} b_{2,j,\sigma} + a^\dagger_{2,j,\sigma} b_{1,j,\sigma} + \mathrm{h.c.}) \\ &- \gamma_4 \sum_{j,\sigma} (b^\dagger_{1,j,\sigma} b_{2,j,\sigma} + \mathrm{h.c.}) \end{aligned} \tag{20}$$

with annihilation operators $a_{m,i,\sigma}$ and $b_{m,i,\sigma}$ for electrons with spin σ in sublattices A and B, respectively. The label $m = 1, 2$ accounts for the two mono-layer graphene planes. The hopping parameters are: $\gamma_0 = t$ the in-plane hopping energy, $\gamma_1 = t_\perp$ the energy describing inter-layer hopping between atoms B1 and A2, γ_3 corresponds to hopping between A1 and B2, and γ_4 is the hopping energy between B1 and B2 [3]. Applying an external perpendicular electric field (e.g. with a gate voltage) induces an electrostatic energy difference between the two layers, defined by the parameter V.

In unbiased bi-layer graphene ($V = 0$) the band structure is given by [62]

$$\varepsilon_k^{\pm\pm} = \pm\sqrt{\varepsilon_\pm^2 + t_\perp^2/4} \pm t_\perp/2, \tag{21}$$

with the electron dispersion of mono-layer graphene $\varepsilon_\pm$ (see Eq. (15)). The result is presented with dashed lines in Fig. 4(c) showing four parabolic bands where two touch at the Dirac points K and K' [3, 62].

Strikingly, in the case $V \neq 0$, i.e. in the presence of a perpendicular electric field, the situation changes. The corresponding energy spectrum is given by

[15]

$$\varepsilon_k^{\pm\pm} = \pm\sqrt{\varepsilon_\pm^2 + t_\perp^2/2 + V^2/4 \pm \sqrt{t_\perp^4/4 + (t_\perp^2 + V^2)\varepsilon_\pm^2}}. \tag{22}$$

This yields a band structure which exhibits a gap Δ_g between valence and conduction band whose size can be controlled by V. The calculated energy is shown as full line in Fig. 4(c). The induced band gap reads [15]

$$\Delta_g = \sqrt{t_\perp^2 V^2/(t_\perp^2 + V^2)}. \tag{23}$$

This demonstrates that bi-layer graphene can be tuned from a gapless system into a semiconductor with a gap which can be controlled externally by the electric field effect. In the region $V \ll t_\perp$ and $V \gg t$ the size of the gap is approximately $\Delta_g \approx V$. The electrostatic energy difference V is related to the perpendicular electric field $\boldsymbol{E} = E\hat{e}_z$. It can be calculated when assuming that the electric field results exclusively from the external applied electric field, $E = E_{\text{ext}}$ [15]. Within the simple parallel plate capacitor model, the gap parameter V in gated exfoliated bi-layer graphene is given by [15]

$$V = (n/n_0 - 2)e^2 n_0 d/(2\epsilon_r \epsilon_0). \tag{24}$$

Here n_0 is the intrinsic carrier density and $n = n_g + n_0$ the total one, where n_g is the charge carrier density induced by the gate voltage U_{g}. The dielectric constants in free space and in bi-layer graphene are defined by ϵ_0 and ϵ_r, respectively.

The energy dispersion of bi-layer graphene is parabolic (if $V = 0$) and thus, unlike in mono-layer graphene, its fermions are massive ($m^* = t_\perp/(2v_{\text{F}}^2) \approx 0.03\, m_{\text{e}}$). Although this behaviour is non-Dirac like, the existence of the A/B sublattices still results in a conserved pseudospin quantum number at low energies making it different to standard two-dimensional electron gases [14–16].

2.2 Cyclotron resonance

In this work various techniques were used to investigate the different samples. An effect of particular importance is introduced in this section.
Cyclotron resonance (CR) measurements provide an unique tool to study char-

acteristic electronic properties of the materials. To understand the significance of this technique it is important to provide an extended description of the effect behind. Therefore, in the following chapter, the quasiclassical description within the Drude-Boltzmann picture as well as the quantum mechanical limit of CR are discussed.

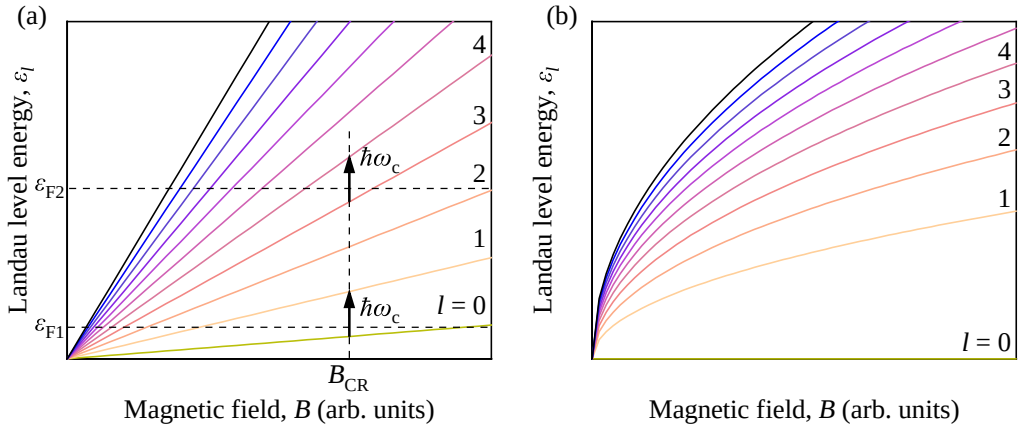

Figure 5: Energies of the Landau level ε_l as a function of the magnetic field. (a) Landau level spectrum in a system with parabolic dispersion. The levels are labelled with $l \in \mathbb{N}$ and are shown for $l = 0$ to $l = 10$ at $\varepsilon(k_z) = 0$ and $l > 0$. Allowed transitions are shown by vertical arrows for two different Fermi energies $\varepsilon_{F1,F2}$ and fixed radiation frequency ω_c. (b) Landau level energy in a two-dimensional system with linear energy momentum relation. Here, for $\varepsilon_F < \hbar\omega_c$ the levels are not equally spaced, while at higher Landau levels, $\varepsilon_F \gg \hbar\omega_c$, the levels become almost equidistant. Adapted from Refs. [63, 64]

In the classical picture, a particle with charge q subjected to an uniform magnetic field $\boldsymbol{B}$ propagates on cyclotron orbits due to the Lorentz force $\boldsymbol{F} = q(\boldsymbol{v} \times \boldsymbol{B})$ acting on it [65, 66]. The circular movement is described by the cyclotron frequency given by [63, 66, 67]

$$\omega_c = \frac{qB}{m} \tag{25}$$

with the carrier mass m as well as the magnetic field strength B. In a solid-state system the carriers experience an additional site dependent potential, which can be taken into account by using the effective mass m^*. [67]. The corresponding equation of motion for carriers in the presence of a magnetic field B and an external ac electric field $\boldsymbol{E}$ is given by [66, 67]

$$m^* \frac{\mathrm{d}\boldsymbol{v}}{\mathrm{d}t} = q(\boldsymbol{E} + \boldsymbol{v} \times \boldsymbol{B}) - \frac{m^* \boldsymbol{v}}{\tau} \tag{26}$$

with the term proportional to the inverse momentum relaxation time τ^{-1} describing the scattering of the carriers e.g. on lattice impurities. If the frequency of the external electric field $\boldsymbol{E}$ is equal to the cyclotron frequency of the carriers and $\omega_c\tau \gg 1$, a strong absorption of the incoming radiation takes place [65, 66]. This effect is called cyclotron resonance and for a fixed radiation frequency ω its position at a certain magentic field strength is given by

$$B_{\mathrm{CR}} = \frac{m^*\omega}{q}. \tag{27}$$

Under CR condition the time-averaged power P which is absorbed per unit volume for circularly polarized radiation has the form [65, 68]

$$P_{\pm}(\omega, \omega_c) = \sigma_0 E_0^2 \frac{1}{1 + (\omega \pm \omega_c)^2\tau^2}. \tag{28}$$

Here, P_+ and P_- account for right-handed and left-handed circularly polarized radiation, respectively. Furthermore, σ_0 is the static dc conductivity of the carriers. Equation (28) shows that the polarization of the ac driving field determines if resonant absorption takes place or not. The polarization of the radiation has to match the direction of the carriers cyclotron motion determined by the magnetic field polarity in order to enable CR. [68]. Due to the fact that linear polarization is a superposition of circularly right- and left-handed polarization states, in this case, resonant absorption is stimulated for both magnetic field polarities.

In the quantum mechanical limit, CR can be described in terms of optical transitions between adjacent quantized Landau levels [69], which are labelled with $l \in \mathbb{N}$. Assuming a system with parabolic band dispersion subjected to a magnetic field applied in z-direction $\boldsymbol{B} = (0, 0, B)$ the energy of electrons is given by [66]

$$\varepsilon = \varepsilon_l + \varepsilon(k_z) = \hbar\omega_c \left(l + \frac{1}{2}\right) + \frac{\hbar^2 k_z^2}{2m^*}, \tag{29}$$

with the energy in direction of the magnetic field $\varepsilon(k_z)$ and the Landau level energy ε_l. This follows from the eigenvalue problem which is similar to that for a harmonic oscillator. The resulting Landau level spectra are shown in Fig. 5(a) exhibiting an equidistant energy spacing of $\Delta_l = \hbar\omega_c = \hbar qB/m^*$. Allowed optical transitions can be found only between adjacent Landau levels

due to dipole selection rules [69]. As illustrated in Fig. 5(a) the corresponding magnetic field strength $|B_{\mathrm{CR}}| = |m^*\omega/q|$ is independent of the Fermi energy but scales linearly with the radiation frequency.
In two-dimensional systems with a linear band structure, like e.g. graphene or surface states of a 3D TI, the situation changes. In this case the Landau level energy has the form [70–72]

$$\varepsilon_l = \mathrm{sgn}(l)\hbar v_{\mathrm{F}}\sqrt{\frac{2eB|l|}{\hbar}} \tag{30}$$

with v_{F} being the Fermi velocity and $l \in \mathbb{Z}$ the Landau level number. Here the values $l < 0$ and $l > 0$ belong to Landau levels within the valence and conduction band, respectively. Equation (30) shows that the energy has a square root dependence on the magnetic field and, therefore, the Landau levels are no longer equidistant. The corresponding energy spacing between neighbouring levels is given by

$$\Delta_l = \hbar\omega_c = \hbar v_{\mathrm{F}}\sqrt{\frac{2eB}{\hbar}}\left(\mathrm{sgn}(l+1)\sqrt{|l+1|} - \mathrm{sgn}(l)\sqrt{|l|}\right) \tag{31}$$

with the cyclotron frequency ω_c depending not only on B but also on l. The calculated Landau level energy is presented in Fig. 5(b) showing a non-equidistant Landau level spectrum. It is important to mention that Eq. (31) is valid in the quantum mechanical limit only, i.e. $\varepsilon_{\mathrm{F}} < \hbar\omega_c$. In this regime due to the non-equidistant spacing of the levels optical transitions appear at different magnetic fields B_{CR} at a fixed radiation frequency.

However, if $\varepsilon_{\mathrm{F}} \gg \hbar\omega_c$, i.e. in the semi-classical regime, the dependence of ω_c on B approaches a linear behaviour [71] which results in an almost equidistant spacing between adjacent Landau levels. The cyclotron frequency is then approximately given by

$$\omega_c \approx \frac{eB}{m^*} \tag{32}$$

This differs from the parabolic case because in systems with linear dispersion the cyclotron mass depends on the carrier density, whereas in systems with parabolic dispersion it is independent of n [71].

2.3 THz induced optoelectronic phenomena

Homogeneous illumination of uniform materials with ac electric fields may lead to several photoelectric effects. In particular, applying terahertz (THz) radiation with photon energies much smaller than the energy gap of most semiconductors, leads to a photocurrent generation due to carrier redistribution in momentum space and in energy [29]. Such phenomena are called nonlinear if they are proportional to the second or higher order of the driving field $\boldsymbol{E}$. The following section devotes to the phenomonological description of a second order phenomenon, the photogalvanic effect, supported by an exemplary microscopic model. In addition, the last section presents third order effects, in particular photoconductivity phenomena.

2.3.1 The photogalvanic effect

The electric field of the radiation can be described by a plane wave yielding

$$\boldsymbol{E}(\boldsymbol{r},t) = \boldsymbol{E}(\omega,\boldsymbol{q})\mathrm{e}^{-i\omega t+i\boldsymbol{q}\cdot\boldsymbol{r}} + \boldsymbol{E}^{*}(\omega,\boldsymbol{q})\mathrm{e}^{i\omega t-i\boldsymbol{q}\cdot r} \tag{33}$$

with the electric field's angular frequency ω, the photon wavevector $\boldsymbol{q}$ and the complex conjugate marked by an asterisk.

Phenomenologically, the interaction of the electric field $\boldsymbol{E}$ with the current density in the material can be expressed as a series of powers of $\boldsymbol{E}$. Thus, the current density $j_\alpha(\boldsymbol{r},t)$ up to the second order of $\boldsymbol{E}$ is given by [26]

$$\begin{aligned} j_\alpha(\boldsymbol{r},t) =& \sum_\beta \left[\sigma^{(1)}_{\alpha\beta}E_\beta(\omega,\boldsymbol{q})\mathrm{e}^{-i\omega t+i\boldsymbol{q}\cdot\boldsymbol{r}} + c.c.\right] \\ &+ \sum_{\beta,\gamma}\left[\sigma^{(2')}_{\alpha\beta\gamma}E_\beta(\omega,\boldsymbol{q})E_\gamma(\omega,\boldsymbol{q})\mathrm{e}^{-i2\omega t+2i\boldsymbol{q}\cdot\boldsymbol{r}} + c.c.\right] \\ &+ \sum_{\beta,\gamma}\left[\sigma^{(2)}_{\alpha\beta\gamma}E_\beta(\omega,\boldsymbol{q})E^{*}_\gamma(\omega,\boldsymbol{q})\right] + ... \end{aligned} \tag{34}$$

Here, σ denotes the conductivity tensor, the greek letters α, β, and γ take the values of the Cartesian coordinates x, y, and z and $c.c$ is the complex conjugate. The first term $\propto E(\omega,\boldsymbol{q})$ describes Ohm's law, which is the change of the current density induced by a static electric field. This part vanishes in the case of an ac electric field, and is therefore not relevant in case of terahertz radiation. The second order term $\propto \mathrm{e}^{-2i\omega t}$ describes second harmonic generation. Such effects are not further discussed here, however, a detailed discussion on this can be found in Ref. [26]. The last term in Eq. (34) $\propto E_\beta(\omega,\boldsymbol{q})E^{*}_\gamma(\omega,\boldsymbol{q})$

describes the dc current generation in response to an ac electric field. The corresponding second-order conductivity $\sigma^{(2)}_{\alpha\beta\gamma}(\omega, \boldsymbol{q})$ can be written as a sum of parts dependent and independent of the photon momentum [26, 73]

$$\sigma^{(2)}_{\alpha\beta\gamma}(\omega, \boldsymbol{q}) = \sigma^{(2)}_{\alpha\beta\gamma}(\omega) + \sigma^{(2)}_{\alpha\beta\gamma}(\omega, \boldsymbol{q}). \tag{35}$$

These two parts can be redefined as follows

$$\sigma^{(2)}_{\alpha\beta\gamma}(\omega) = \chi_{\alpha\beta\gamma}(\omega), \text{ and } \sigma^{(2)}_{\alpha\beta\gamma}(\omega, \boldsymbol{q}) = T_{\alpha\delta\beta\gamma} q_\delta \tag{36}$$

with the coefficients $\chi_{\alpha\beta\gamma}$ and $T_{\alpha\delta\beta\gamma}$ being third and fourth rank tensors, respectively. Using Eq. (35) the current density from Eq. (34) can be rewritten to [29]

$$j_\alpha = \underbrace{\sum_{\beta,\gamma} \chi_{\alpha\beta\gamma} E_\beta E^*_\gamma}_{\text{photogalvanic effect}} + \underbrace{\sum_{\delta,\beta,\gamma} T_{\alpha\delta\beta\gamma} E_\beta E^*_\gamma q_\delta}_{\text{photon drag effect}} \tag{37}$$

Here, the first term represents the photogalvanic effect (PGE) and the second one the photon drag effect (PDE). In the following the PGE is considered in more detail. It is important to note that the PGE is only allowed in noncentrosymmetric systems because of the fact that $j_\alpha(-r) = -j_\alpha(r)$ accounts only for $\chi_{\alpha\beta\gamma} = 0$ [26, 29]. To go on, the external product $E_\beta E^*_\gamma$ can be decomposed into a sum of a symmetric $\{E_\beta E^*_\gamma\} = \frac{1}{2}(E_\beta E^*_\gamma + E_\gamma E^*_\beta)$ and an antisymmetric products $[E_\beta E^*_\gamma] = \frac{1}{2}(E_\beta E^*_\gamma - E_\gamma E^*_\beta)$, which yields [29]

$$E_\beta E^*_\gamma = (\{E_\beta E^*_\gamma\} + [E_\beta E^*_\gamma]). \tag{38}$$

Here, the first term on the right hand side is real and symmetric, while the second one is purely imaginary and antisymmetric. Using the totally antisymmetric Levi-Civita tensor $\epsilon_{\nu\beta\gamma}$ the third rank tensor $\chi_{\alpha\beta\gamma}$ can be reduced to a second rank pseudotensor $\zeta_{\alpha\nu}$ in the antisymmetric part [29]

$$\sum_{\beta,\gamma} \chi_{\alpha\beta\gamma}[E_\beta E^*_\gamma] = i \cdot \sum_{\nu,\beta,\gamma} \zeta_{\alpha\nu}\epsilon_{\nu\beta\gamma}[E_\beta E^*_\gamma] = \sum_\nu \zeta_{\alpha\nu} i(\boldsymbol{E} \times \boldsymbol{E}^*)_\nu \tag{39}$$

Concluding, the total PGE photocurrent density $J_{\alpha,\mathrm{PGE}}$ is given by [29]

$$j_{\alpha,\mathrm{PGE}} = \underbrace{\sum_{\beta,\gamma} \chi_{\alpha\beta\gamma}\{E_\beta E_\gamma^*\}}_{\mathrm{LPGE}} + \underbrace{\sum_{\nu} \zeta_{\alpha\nu} i(\boldsymbol{E}\times\boldsymbol{E}^*)_\nu}_{\mathrm{CPGE}} \tag{40}$$

with the first term on the right hand side describing the linear photogalvanic effect (LPGE) and the second one the circular photogalvanic effect (CPGE). Equation 40 demonstrated that the LPGE can be observed under excitation with linear polarized radiation, while for the CPGE circularly polarized radiation is required. Since $\chi_{\alpha\beta\gamma}$ has non-zero components only in non-centrosymmetric media of piezoelectric crystal classes the LPGE is only allowed in these materials. In contrast, the CPGE depends on the helicity of the radiation and is not excited by linear polarized radiation. This effect depends on the second-rank pseudotensor $\zeta_{\alpha\nu}$ and is therefore only allowed in gyrotropic media [29].

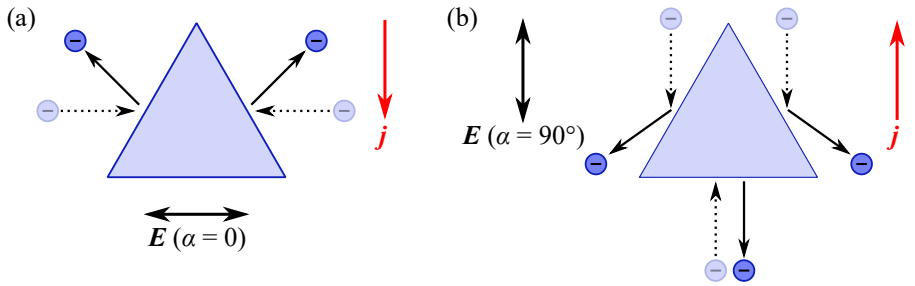

Figure 6: Schematic illustration of the microscopic model of the LPGE in systems with C_{3v} symmetry exemplary shown for electrons (blue circles). The electrons move along the oscillating electric field $\boldsymbol{E}$ (illustrated by dashed arrows) and scatter on the equally oriented wedges. This causes an alignment of the carrier momenta (solid arrows) and, consequently, a generation of an electric current $\boldsymbol{j}$ (red arrow). The preferred scattering direction depends on the orientation of the electric field vector, defined by the azimuthal angle α. In panels (a) and (b) the scattering process is shown for two perpendicular polarization states, resulting in opposite directions of the generated photocurrent. Adapted from Refs. [29, 74, 75]

.

Microscopic model for LPGE In the following, an exemplary microscopic model for the LPGE in systems with C_{3v} symmetry is provided. Such systems lack an inversion centre which results in an asymmetric scattering even for scatterers without anisotropy [74–76]. The scattering is described by the probability for a transition of a particle from a state with momentum $\boldsymbol{p}$ to a

state with $\boldsymbol{p'}$, given by $W_{\boldsymbol{p},\boldsymbol{p'}}$. Assuming elastic scattering the symmetry relation $W_{\boldsymbol{p},\boldsymbol{p'}} \neq W_{-\boldsymbol{p},-\boldsymbol{p'}}$ holds. The photocurrent generation within the LPGE can be visualized by asymmetric elastic scattering of charge carriers on randomly distributed, but equally oriented triangle shaped wedges. Latter one is characteristic for the symmetry in systems belonging to the C_{3v} symmetry group [29, 76, 77].

Figure 6 illustrates the elastic scattering on wedges and the subsequent photocurrent generation. Exciting a material with an ac electric field $\boldsymbol{E}$ oriented at an angle α results in an optical alignment of the carrier momenta along the polarization direction[2] which on its own does not result in an net electric current. The subsequent asymmetric scattering on the wedges, however, results in a predominant scattering direction and consequently in a photocurrent. The magnitude and direction of this current strongly depends on the relative orientation of the radiation's electric field vector $\boldsymbol{E}$ with respect to the wedges. In Fig. 6(a) the radiation is polarized horizontally and the generated photocurrent flows in a direction normal to the electric field. The photocurrent reverses its direction if the radiation is polarized vertically, see Fig. 6(b). This polarization dependence is characteristic for the LPGE, for reviews see e.g. Refs. [29, 74, 76, 81].

2.3.2 Photoconductivity

Equation (34) gives a phenomenological description of the current density up to the second order of the electric field. Third order effects, in general, can as well be excited by terahertz radiation. In particular, in the special case if a static field $\boldsymbol{E}^{(\mathrm{dc})}(0,0)$ is applied. Latter one can be realized by application of a bias voltage to the system. This can result in photoconductivity phenomena like $\mu-$photoconductivity. The understanding of these effects is particularly important since the high power terahertz radiation leads to a strong heating of the electron gas, and, consequently, to a change of the sample conductivity. Here, the generated current is given by [26, 76]

$$j_\alpha(\boldsymbol{r},t) = \sum_{\beta\gamma\delta} \sigma^{(3'')}_{\alpha\beta\gamma\delta} E_\beta(\omega,\boldsymbol{q}) E^*_\gamma(\omega,\boldsymbol{q}) E^{(\mathrm{dc})}_\delta(0,0), \tag{41}$$

[2] Note that this is valid only for intraband transitions and Drude absorption [31, 78]. In the case of interband transition the momenta get aligned perpendicular to the electric field vector [79, 80].

where $\sigma^{(3'')}_{\alpha\beta\gamma\delta}$ is the fourth-order conductivity tensor. Equation 41 shows that this effect is proportional to the static electric field and to the intensity $I \propto |\boldsymbol{E}|^2(\omega, \boldsymbol{q})$. In the following the microscopic model of electron gas heating and $\mu-$photoconductivity is provided.

Electron gas heating and $\mu-$photocondcutivity Variations of the sample conductivity induced by absorption of high power terahertz radiation may result from changes in the carrier density n, e.g. due to electron-hole pair generation or light impact ionization. Another possible mechanism for photoconducitvity phenomena are based on changes of the carrier mobility μ. The corresponding change of the conductivity $\Delta\sigma$ then reads

$$\Delta\sigma = |e| n \Delta\mu, \tag{42}$$

where $\Delta\mu$ is the change of the mobility induced by the radiation. In relation to this, the effect is termed $\mu-$photoconductivity. The terahertz radiation gets absorbed by free carriers which may result in a strong heating of the electron gas [29]. If the carrier density n is large enough, the electron-electron scattering time τ_{ee} is much shorter than the energy relaxation time τ_ε. From this follows that the absorption leads to an electron temperature T_{e} which differs form the temperature of the surrounding lattice T_{lattice} due to electron-electron scattering. The magnitude of T_{e} depends on the competition between power absorption and energy loss. This temperature T_{e} can be found from the balance equation for bulk materials [29]

$$\frac{K(\omega) I \varepsilon_{\mathrm{eff}}}{\hbar\omega} = \langle Q(T_{\mathrm{e}}) \rangle \, n, \tag{43}$$

where $K(\omega)$ is the absorption coefficient, $\varepsilon_{\mathrm{eff}}$ the effective energy released from one photoexcited electron to the electron system in equilibrium, and $\langle Q \rangle = \langle \mathrm{d}\varepsilon/\mathrm{d}t \rangle$ gives the energy loss per unit of time for a single carrier.

The variation of the conductivity, normalized to the dark conductivity $\sigma_0 = |e| n \mu$, induced by the radiation can be approximated by [29]

$$\frac{\Delta\sigma}{\sigma_0} = \frac{1}{\mu} \frac{\partial\mu}{\partial T_{\mathrm{e}}}\bigg|_{T_{\mathrm{e}}=T_{\mathrm{lattice}}} \Delta T_e. \tag{44}$$

This equation indicates that the sign of the $\mu-$photoconductivity depends on the sign of $\frac{\partial\mu}{\partial T_e}$. The sign may give information about the predominant

scattering mechansim. For instance, if impurity scattering dominates $\frac{\partial \mu}{\partial T_e}$ is positive while it is negative for scattering on phonons [65, 82].

Highly intense THz radiation may also affect the lattice temperature T_{lattice}. In this case the response time of the photoconductivity process is usually longer than in electron-temperature driven processes, where the time corresponds to the energy relaxation time τ_ε ($\approx$ ps). However, due to rather low pulse energies used in this work lattice-involving processes are neglected.

3 Methods

The following chapter is dedicated to the investigated samples and the applied experimental techniques. It begins with a description of the samples based on HgTe and graphene. Furthermore, the used laser systems, their mode of operation as well as the experimental setups are outlined, including optical and electrical components.

3.1 Investigated samples

3.1.1 HgTe/CdTe heterostructures

The measurements on HgTe were carried out on HgTe films having different thicknesses of either 80 nm or 200 nm. All films have been grown on GaAs substrates with (013) or (001) crystal orientation by molecular beam epitaxy (MBE). A schematic cross section of the systems under study is depicted in Fig. 7(a). The layer ordering is similar for all investigated samples with the HgTe film being sandwiched between $Hg_{0.4}Cd_{0.6}Te$, a well known technique to increase the mobility of the material and to decrease the number of bulk impurities [83].

Since the lattice mismatch of HgTe on GaAs is rather large the substrate is covered by a thin ZnTe layer and a 4 µm thick fully relaxed CdTe layer having a 0.3 % larger lattice constant as HgTe. If the latter fully adopts the lattice constant of CdTe this results in uniaxial strain and in an opening of an indirect bulk bandgap of 15 meV in the HgTe layer [38, 40]. In general, it is expected that the thickness of the pseudomorphic growth of HgTe films on CdTe substrates lies in the order of 100-150 nm [37, 40]. Under this assumption the 200 nm system under study should have a bulk bandgap close to zero. Fig. 7(b) shows a two crystal high resolution x-ray diffraction measurement performed in Ref. [40] to study the average strain on a 200 nm HgTe film arising from the lattice mismatch between HgTe and CdTe . Note that the data were measured on a structure fabricated from a wafer which is also investigated in this work (wafer #B), see sample description below. The diffraction curves were obtained for a [026] reflex in opposite directions, which correspond to azimuthal angles $\delta = 0$ and 180°. Looking at the peak position values it can be concluded that the HgTe, though already partly relaxed, still adopts to the CdTe layer. This means that the investigated 200 nm thick HgTe film still exhibits an average strain of approximately 60 % (100 % would be a fully

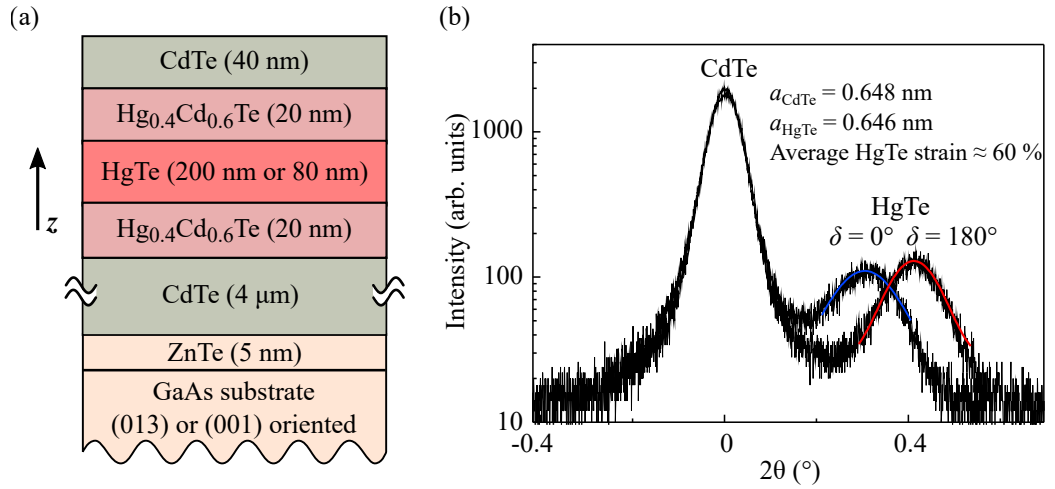

Figure 7: (a) Layer ordering of the investigated samples. By means of MBE the HgTe layer (80 nm or 200 nm thick) is grown on a GaAs substrate with (013) or (001) crystal orientation. The film is sandwiched between two $Hg_{0.4}Cd_{0.6}Te$ layers serving as cap and buffer layer. The fully relaxed CdTe film covering the GaAs substrate is the cause for the strain in the HgTe film opening an indirect bulk band gap. Panel (b) shows an x-ray diffraction measurement of a system with a 200 nm HgTe film in a symmetrical Bragg geometry. The data reveal an average strain of 60 % in the HgTe film arising from the lattice mismatch between CdTe and HgTe. Figure adapted from Ref. [40]

strained HgTe film with an indirect bulk band gap of about 15 meV [37, 38, 84] and 0 % a fully relaxed one where the valence and conduction band overlaps). Comparing this value with thinner films, e.g. 80 nm HgTe studied in Refs. [38, 83], the reduced strain in 200 nm thick HgTe films should result in a significantly smaller but still existent bulk band gap.

To vary the Fermi level position ε_F some of the 200 nm samples were equipped with semitransparent gates on top. For this purpose 14 nm thick NiCr was deposited on 100 nm Al_2O_3 grown by atomic layer deposition.

For the measurements presented in this work several samples were fabricated in the group of Dr. Sergey Dvoretsky and Dr. Sergey Mikhailov at the A.V. Rzhanov Institute of Semiconductor Physics, Novosibirsk, Russia. Wafer #A owns a 80 nm thick HgTe film grown on GaAs with (001) crystal orientation whereas wafer #B, mostly studied in this work, has a 200 nm thick HgTe layer on a (013) oriented substrate. The samples were shaped in either van der Pauw (VdP) or Hall bar geometry and mounted on 8 pin sample holders. Figure 8(a) shows a photograph of a 200 nm HgTe VdP sample made from wafer #A and

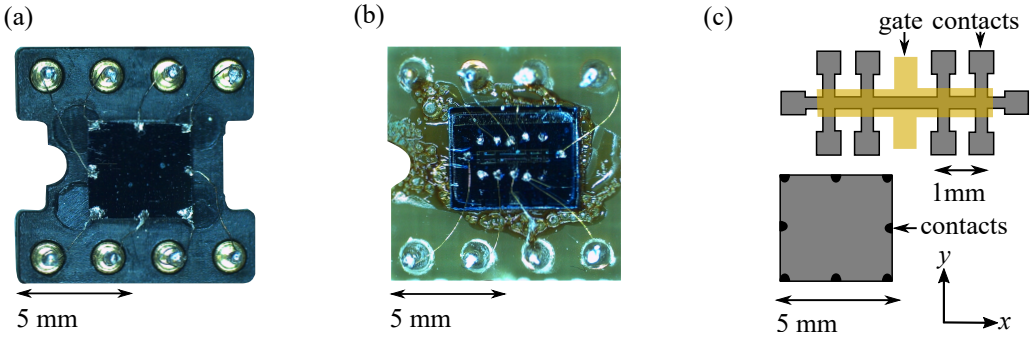

Figure 8: (a) Photograph of the 200 nm-HgTe sample in van der Pauw (VdP) geometry and (b) in Hallbar geometry with a semitransparent top gate. The samples are from the same wafer #B. (c) Schematic illustration of the samples and cartesian coordinates: Top one shows the Hallbar geometry with ten contacts and a top gate. The bottom one illustrates the VdP geometry with eight ohmic contacts.

(b) a Hall bar structure from the same wafer additionally equipped with a top gate. A sketch of the samples is presented in Fig. 8(c) where the top structure shows the conducting channel of a rather big Hall bar corresponding to panel (b) and the bottom scheme shows a typical VdP sample with eight ohmic contacts, one at each corner and in the middle of each edge which are oriented along $x \parallel [100]$. The contacts are soldered with indium and connected via goldwires to the sample holder.

To characterize the samples transport measurements were carried out. Here, exemplary the results obtained for partially relaxed 200 nm HgTe samples from wafer #B are shown. Figure 9(a) depicts the longitudinal sheet resistance ρ_{xx} at $B = 0$ as a function of the applied gate voltage U_g. It shows an asymmetric behaviour around a maximum located at $U_g \approx 0.6\,\mathrm{V}$. While the resistance at the right side of the peak drops sharply at about $U_g = 2\,\mathrm{V}$ to well below 100 Ω it is about twice as high on the left side. A similar behaviour was already detected in thinner 80 nm HgTe films, see Refs. [40, 83], and can be well understood by considering a schematic band diagram of such thicker 200 nm HgTe films, presented in Fig. 9(b). Since the film is partially relaxed it has a much smaller indirect bulk energy gap of approximately 3 meV as compared to 80 nm films [38, 83]. Different to bulk HgTe the valence band edge lies beside the Γ point whereas the conduction band has its minimum at the centre of the Brillouin zone. Topologically protected surface states with almost linear dispersion exist in the system having a Dirac point situated deep

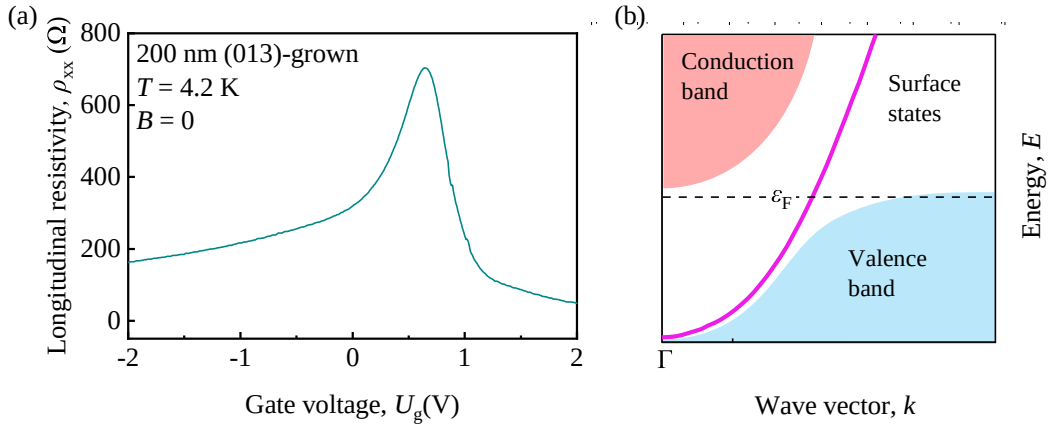

Figure 9: (a) Gate dependence of the longitudinal resistance, measured in a 200 nm thick HgTe sample at a temperature of $T = 4.2$ K without a magnetic field applied. Panel (b) shows a schematic illustration of the energy dispersion of a 200 nm HgTe system at zero effective gate voltage. The Dirac point of the surface states which are illustrated by the magenta solid line is situated deep in the valence band. The Fermi level position is depicted by the vertical dashed line. Figure adapted from Ref. [40].

in the valence band [37, 40]. By changing the applied gate voltage the Fermi level ε_F can be tuned from the valence band across the charge neutrality point (CNP) (maximum of ρ_{xx}) all over to the conduction band. The behaviour of the longitudinal resistance observed in the transport, see Figure 9(a), supports this assumption. At negative gate values ε_F lies in the valence band meaning that bulk holes and surface electrons coexist. Changing the gate voltage to positive values shifts the Fermi level towards the conduction band, where bulk electrons contribute to the transport as well as the high-mobility electrons on the surface. Thus, the comparison of the longitudinal resistivity between left and right side of the CNP indicates a significant difference between the bulk electron and hole mobilities.

Figure 10(a) shows the Hall resistance as a function of the magnetic field at selected temperatures for a 200 nm thick HgTe film (wafer #B). For low fields a nonlinear N-shape can be observed which is an indication for the co-existence of electrons and holes, similarly observed in previously investigated 80 nm HgTe films [38, 83]. It is noticeable, that the Hall resistance changes its sign for higher temperatures, indicating thermal activation of charge carriers. At low temperatures the current is mainly transported by holes since in ungated HgTe the Fermi level lies in the valence band, see Fig. 9(b) [38, 83]. The smaller contribution stemming from electrons can be attributed to the high-mobility surface states. However, at higher temperature the electron

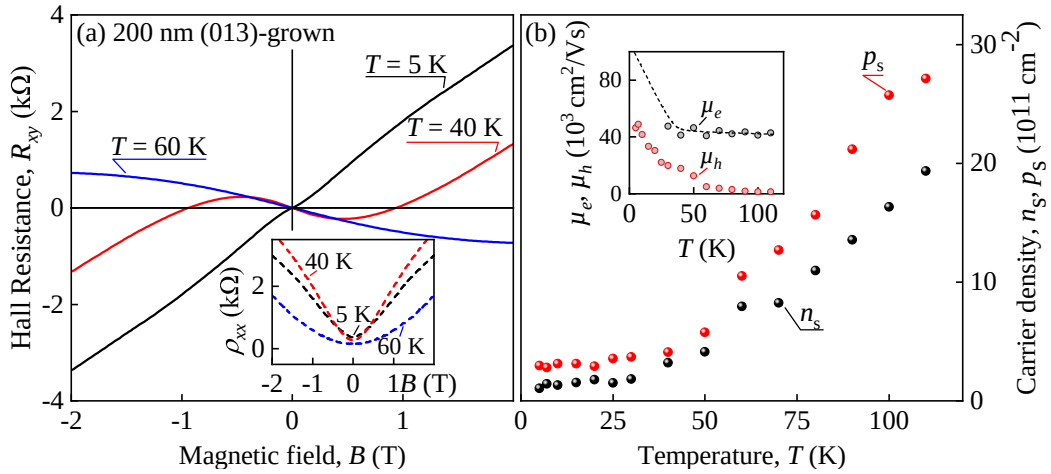

Figure 10: Magnetotransport of a sample from the 200 nm HgTe wafer #A. Panel (a) shows the Hall resistance as a function of the magnetic field for selected temperatures. During the same measurement the longitudinal sheet resistance ρ_{xx} was also detected and is presented in the inset. Panel (b) depicts the extracted carrier densities, n_s and p_s respective to electron and hole conductivity, as a function of the temperature in the sample chamber. The inset shows the electron and hole mobilities μ_e and μ_h, respectively. These characteristics where obtained by applying the classical two-carrier Drude model. Figures adapted from Ref. [30]

.

contribution increases due to increasing bulk electron concentration.

The corresponding longitudinal sheet resistance as a function of the magnetic field is shown in the inset revealing always positive values and a symmetric behaviour around zero field. From the magnetotransport data the carrier density can be extracted and is presented in Fig. 10(b) as function of the temperature. It shows the electron and hole density n_s and p_s, respectively, extracted by fitting $R_{xy}(B)$ and $\rho_{xx}(B)$ applying the classical two-carrier Drude formalism [83]. The corresponding hole and electron mobilities μ_e and μ_h are presented in the inset. Note that the electron mobility for low temperatures is not shown, because the fitting gets more inaccurate here due to the low electron density. An expected trend of the electron mobility at low temperatures is indicated by the dashed line [38, 83].

3.1.2 Graphene-based systems

Beside HgTe films also several systems based on graphene were studied in this work including mono-and bi-layer graphene samples. The Hall bar shaped mono-layer graphene samples (MLG #1, MLG #2, and MLG #4) were fab-

ricated in collaboration with the group of Dr. Jonathan Eroms/Prof. Dr. Dieter Weiss. The bilayer graphene samples (BLG #1 and #2) fabricated as VdP and Hall bar structures were produced at Manchester university from the group of Prof. Dr. Artem Mischenko.

The investigated devices consist of exfoliated graphene layers sandwiched between hexagonal boron nitride (h-BN) layers, see Fig. 11(a). H-BN being an insulating isomorph of graphite is an ideal substrate candidate to improve the quality and durability of graphene-based devices. It was demonstrated that such devices exhibit enhanced mobilities, reduced carrier inhomogenities as well as an intrinsic doping being lower than in SiO_2 supported devices [85].

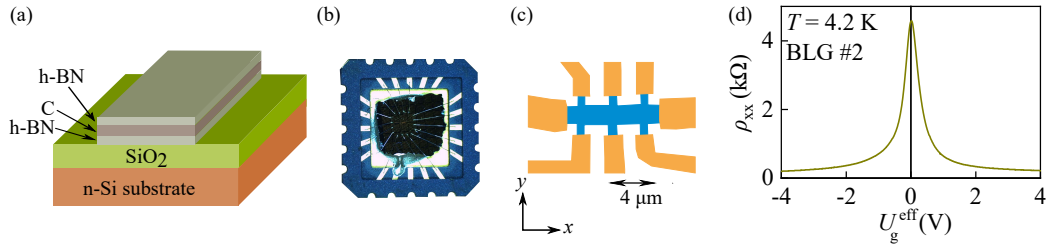

Figure 11: (a) Layer ordering of the studied graphene devices. The graphene flake is sandwiched between h-BN layers and transferred to a Si wafer. Panel (b) shows a picture of the mono-layer graphene sample MLG #2 glued into a 20 pin chip carrier. Two Hall bar structures on the graphene flake are connected via gold wires with the holder. (c) Schematic of the Hall bar geometry showing the conducting channel and Cr/Au contacts as well as Cartesian coordinates. (d) Longitudinal sheet resistance as a function of the effective gate voltage U_g^{eff} obtained in sample BLG #2 at $T = 4.2\,\text{K}$.

To produce these high mobility graphene samples the exfoliated graphene flakes are picked up by van der Waals interactions with an h-BN flake and further transferred onto a second h-BN flake supported by a SiO_2 substrate. After an annealing procedure the stacks are patterned into a Hall bar geometry by means of electron beam lithography and reactive ion etching, and then contacted using Cr/Au [86, 87]. Afterwards the samples are glued into 20 pin chip carriers ($8 \times 8\,\text{mm}^2$) using silver filled epoxy to contact the back gate and then electrically wire-bonded, see Fig. 11(b). Figure 11(c) exemplary shows the Hall bar shape of samples MLG #1 and #2. An overview of the samples studied in this work is given in table 1 presenting their dimensions as well as the corresponding carrier densities.

To characterize the devices transport measurements were performed by applying an ac current of $I_{\text{ac}} = 10\,\text{nA}$. Upon variation of the applied gate voltage

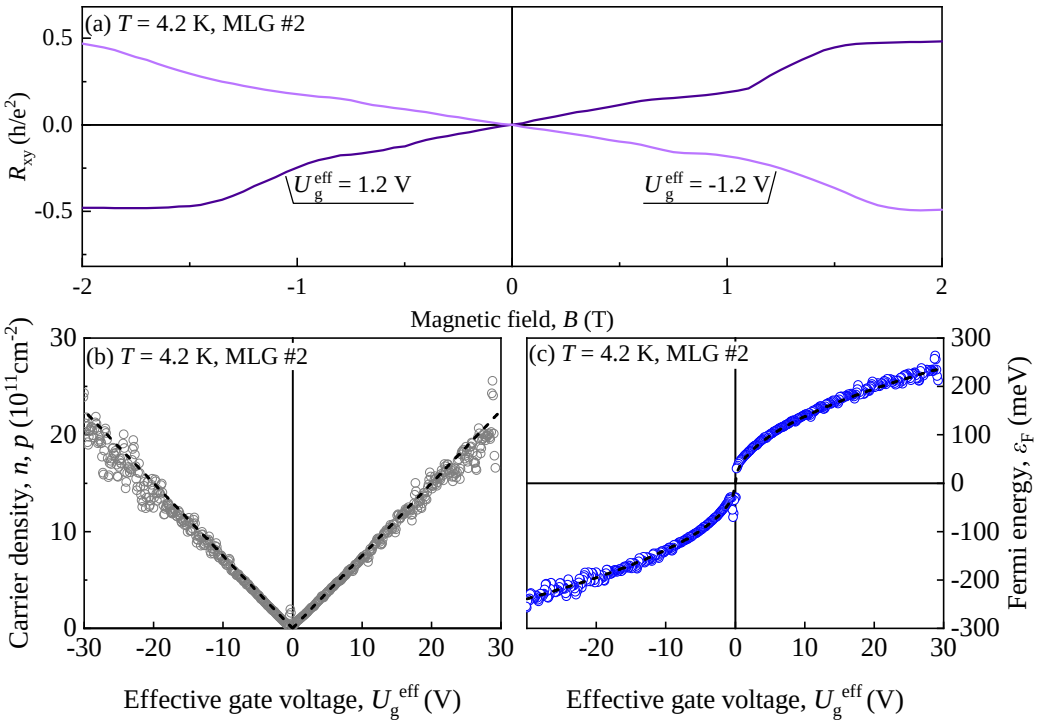

Figure 12: Characteristics of sample MLG #2 obtained from magnetotransport measurements. (a) Transverse resistance R_{xy} as a function of the magnetic field for two different effective gate voltages $U_{\mathrm{g}}^{\mathrm{eff}} = \pm 1.2\,\mathrm{V}$. (b) The carrier densities n, p (grey open circles) for electron and hole transport with a linear fit after $\pm 0.75 \cdot 10^{11} U_{\mathrm{g}}^{\mathrm{eff}}$ (dashed line). (c) Variation of the Fermi energy ε_{F} with the effective gate voltage $U_{\mathrm{g}}^{\mathrm{eff}}$. Dashed line shows the calculated ε_{F} using the linear fit from panel (b)

the CNP can be detected as the maximum of the longitudinal resistance, see exemplary Fig. 11(d). Since the CNP can slightly shift for different sample cool downs an effective gate voltage is introduced $U_{\mathrm{g}}^{\mathrm{eff}} = U_{\mathrm{g}} - U_{\mathrm{g}}^{\mathrm{CNP}}$. The sample characteristics, presented in table 1 were obtained from magnetotransport measurements at $T = 4.2\,\mathrm{K}$, exemplary shown in Fig. 12 for sample MLG #2.

Figure 12(a) shows the transverse Hall resistance R_{xy} as a function of the magnetic field B for two effective gate voltages $U_{\mathrm{g}}^{\mathrm{eff}} = +1.2$ and $-1.2\,\mathrm{V}$. The slopes have opposite signs revealing different carrier types, i.e. n- and p-type conductivity for positive and negative $U_{\mathrm{g}}^{\mathrm{eff}}$, respectively. The quantum Hall effect is well observable showing the first Hall plateau with filling factor $\nu = 2$ already below $B = 2\,\mathrm{T}$[3]. The variation of the carrier density for n and p type conductivity with the gate voltage is presented in Fig. 12(b) where the black dashed line follows the linear fit after $\pm 0.75 \cdot 10^{11} U_{\mathrm{g}}^{\mathrm{eff}}$. The carrier densities

[3]Note that in the bi-layer graphene samples no Hall plateaus in the transverse resistance were detected in this magnetic field range.

Sample name	Size [µm/µm]	$n\,[\mathrm{cm}^{-2}]/\lvert U_\mathrm{g}^\mathrm{eff}\rvert\,[\mathrm{V}]$	$p\,[\mathrm{cm}^{-2}]/\lvert U_\mathrm{g}^\mathrm{eff}\rvert\,[\mathrm{V}]$
MLG #1	W/L = 2/9	$0.90 \cdot 10^{11}$	$0.55 \cdot 10^{11}$
MLG #2, #4	W/L = 2/9	$0.75 \cdot 10^{11}$	$0.75 \cdot 10^{11}$
BLG #1	W/L = 7/7	$2.50 \cdot 10^{11}$	$2.50 \cdot 10^{11}$
BLG #2	W/L = 9/31	$0.46 \cdot 10^{11}$	$0.65 \cdot 10^{11}$

Table 1: Characteristics of the mono-layer graphene samples MLG #1 and #2 as well as the bi-layer graphene samples BLG #1 and #2. The carrier densities are obtained from magnetotransport measurements at $T = 4.2\,\mathrm{K}$. Note that all samples, except BLG #1 (VdP), are shaped in Hall bar geometry.

for the other samples under study can be found in table 1. Figure 12(c) shows the Fermi energy ε_F as a function of the effective gate voltage. From the magnetotransport measurements also the charge carrier mobilities of the graphene devices studied in this work can be extracted which lie in the range 0.9×10^5 to $1.5 \times 10^5\,\mathrm{cm}^2/\mathrm{Vs}$ at $T = 4.2\,\mathrm{K}$.

3.2 Measurement technique

3.2.1 THz laser systems

Optically pumped THz molecular gas laser [29, 88] were used to excite the investigated samples. The THz lasers are pumped by CO_2 lasers exciting vibrational-rotational transitions of molecules having a permanent electric dipole moment. Such laser systems are well approved since they are robust, can achieve very high powers and cover a wide range of frequencies in the THz range [29]. To accomplish the desired THz laser line the CO_2 laser provides monochromatic radiation between approximately 9 and 11 µm coming from rotational-vibrational transitions of two P- and R-branches. Note that P and R indicate the change of the rotational quantum number $\Delta J = +1$ and -1, respectively.

In the molecules chosen for generation of THz radiation, the vibrational levels characterized by quantum numbers ν split up into rotational levels with angular momentum J. The mid infrared (MIR) CO_2 radiation results in vibrational-rotational transitions leading to population inversion in the vibrational states. The relaxation transitions between the rotational modes are used to emit photons with energies in the THz range. The frequency of this

emitted radiation depends on the one hand on the laser gas and on the other hand on the pump line coming from the CO_2 laser. Molecules used in this work are NH_3, CH_3OH, CH_3F,CH_2F_2, D_2O and CH_2O_2, yielding several frequency lines between 0.6 and 8.5 THz. The distance of the rotational levels is determined by the molecules weight [67], and therefore, lighter molecules generate radiation with higher frequency. However, laser operation is also possible with pump lines being different from the molecular transition. This is due to stimulated Raman scattering which emerges in pulsed THz lasers depending on excitation energy and gas pressure [29, 89].

In this work two types of THz molecular lasers were used, a pulsed THz molec-

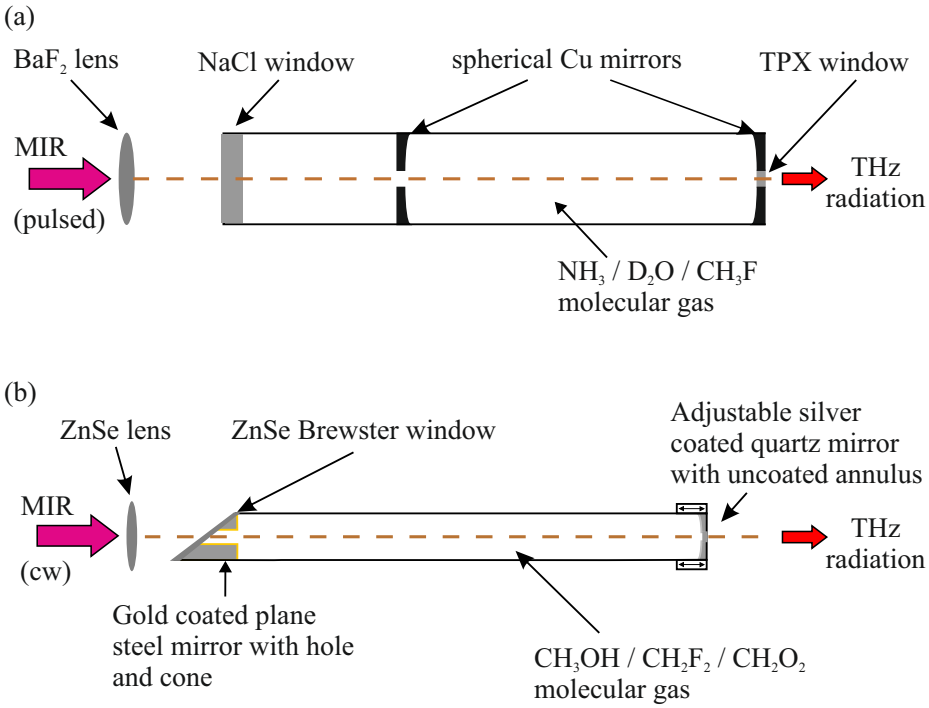

Figure 13: Sketch of the used molecular THz laser systems pumped by MIR radiation from CO_2 lasers. (a) Pulsed THz laser and (b) cw THz laser. Adapted from Ref. [90].

ular laser pumped by a transversely-excited atmospheric pressure (TEA) CO_2 laser and a continous wave (cw) THz molecular laser pumped by a longitudinally excited cw CO_2 laser. Their build-up is very similar, see Fig. 13 (a) and (b), and both lasers exhibit a fundamental Gaussian beam profile. The latter one is checked by a pyroelectric camera [91], which is also used to determine the full width at half maximum in x and y direction lying between 1.5 and 3.5 mm depending on the wavelength. These values guarantee a homogeneous illumination of the µm-sized samples. The knowledge of the full width at half

maximum is particularly important for the calculation of the radiation intensity at the sample position. In the following the main differences of the used laser systems are depicted.

Molecule	λ (µm)	f (THZ)	$\hbar\omega$ (meV)	pump line
NH_3	90	3.33	13.7	9R(16)
NH_3	148	2.02	8.4	9P(36)
NH_3	280	1.07	4.4	10R(8)
D_2O	385	0.78	3.2	9R(22)
CH_3F	496	0.61	2.5	9R(20)

Table 2: Characteristics of the THz laser lines used in this work pumped by a pulsed TEA-CO_2 laser. After Ref. [29]

Pulsed molecular THz laser The pulsed MIR radiation coming from a (TEA) CO_2 laser has a pulse duration of approximately 100 ns and peak powers up to MW. Figure 13 (a) shows a typical build-up of a pulsed molecular THz laser. The MIR radiation focused with a BaF_2 lens is coupled through a NaCl window into a resonator. The latter one contains of a glass tube with two spherical Cu mirrors having an in/outcoupling hole and is filled with the active media. To prevent the remaining MIR radiation from leaving the resonator a TPX (poly-4-methyl-1-penthen) window which is transparent for THz radiation but not for MIR radiation is placed at the output. This laser system generates pulses with a similar temporal shape as the pump source (≈ 100 ns) and a frequency dependent peak power of several tens of kW. An overview of the used molecules with corresponding wavelengths, frequencies and photon energies is given in table 2. The used pump line coming from the CO_2 laser is indicated with the vibrational transition (10.4 µm or 9.4 µm), the branch P or R and the angular momentum number J of the final state.

Continuous wave molecular THz laser In contrast to the pulsed THz laser system the pumping energy for the cw THz laser comes from a longitudinally excited cw CO_2 laser with powers up to 50 W. The MIR radiation is focused with a ZnSe lens and coupled into the resonator through a ZnSe Brewster window, see Fig. 13 (b). The resonator filled with molecular gas consists of a gold-coated steel mirror at the entrance and semi-transparent silver coated

z-quartz mirror at the output. This quartz mirror is adjustable allowing to control the generated mode structure and wavelength by changing the resonator length. To ensure an absorption of the MIR radiation an additional uncoated central z-cut quartz annulus is placed at the output being transparent for the generated THz radiation. For the cw THz laser system CH_3OH,CH_2F_2 and CH_2O_2 are used as active media yielding frequencies $f = 2.54, 1.63$ and 0.69 THz with line-dependent powers up to 80 mW.

3.2.2 Experimental setup

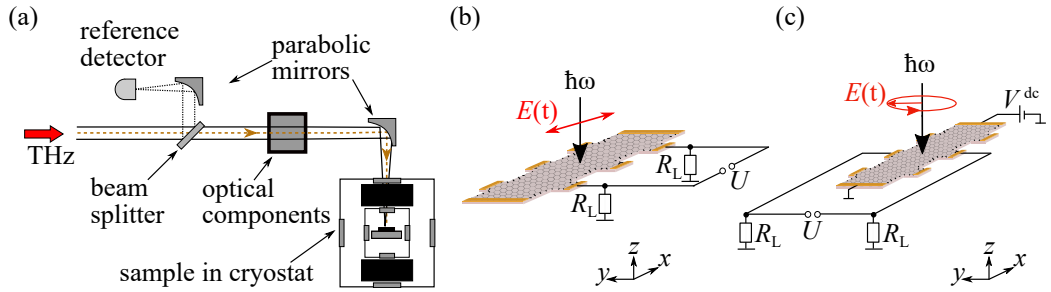

Figure 14: (a) Exemplary sketch of the measurement setup. Adapted from Ref. [90]. (b) Photocurrent measurement setup. The photocurrent signal is measured as a voltage drop over load resistors. (c) Four terminal photoconductivity measurement setup. A dc bias voltage is applied to the sample and the signal is picked up at contacts across the Hall bar. Note that in some measurements a two terminal setup is used where the signal is picked up in same direction as the bias voltage is applied.

Leaving the resonator the generated THz radiation passes through several optical components, e.g. polarizers or wave plates, and is focussed by a parabolic mirror into an optical cryostat where the sample is mounted, see an exemplary sketch of the setup in Fig. 14 (a). In this work three different types of cryostats where used: For most of the measurements with the pulsed laser system a liquid helium flow cryostat was employed. Note that in this setup the application of a magnetic field is not provided. At the cw laser systems either a helium bath cryostat or a variable temperature helium cryostat where the temperature can be varied from $T = 2\,\mathrm{K}$ to room temperature was used. In these cryostats the sample is mounted between two superconducting split coils which are able to provide magnetic fields up to $\pm 7\,\mathrm{T}$. In all measurements the magnetic field was applied in Faraday geometry, i.e. normal to the sample surface. However, it is not only the influence of the magnetic field and temperature on the sample that is crucial, also polarization state and inten-

sity of the incoming THz radiation play an important role for optoelectronic phenomena excited in the graphene or HgTe samples. Therefore, the following subchapters are dedicated to the optical components and methods used in this work to manipulate or characterize the used THz radiation.

Variation of the radiation's polarization state THz radiation induced effects, in particular photogalvanic currents studied in this work, strongly depend on the polarization state of the incoming radiation. The generated THz radiation is almost perfectly linear polarized making it a good candidate for manipulation. In the following a brief introduction of the stokes parameters [92] describing the radiation polarization state and the wave plates [29] applied to manipulate this state is given.
The light's polarization state is well described in terms of the four Stokes parameter. The first one s_0 describing the light's total intensity, s_1 and s_2 the degree of linear polarization and the last one s_3 characterizes the degree of circular polarization. Latter one vanishes in case of purely linear polarization.

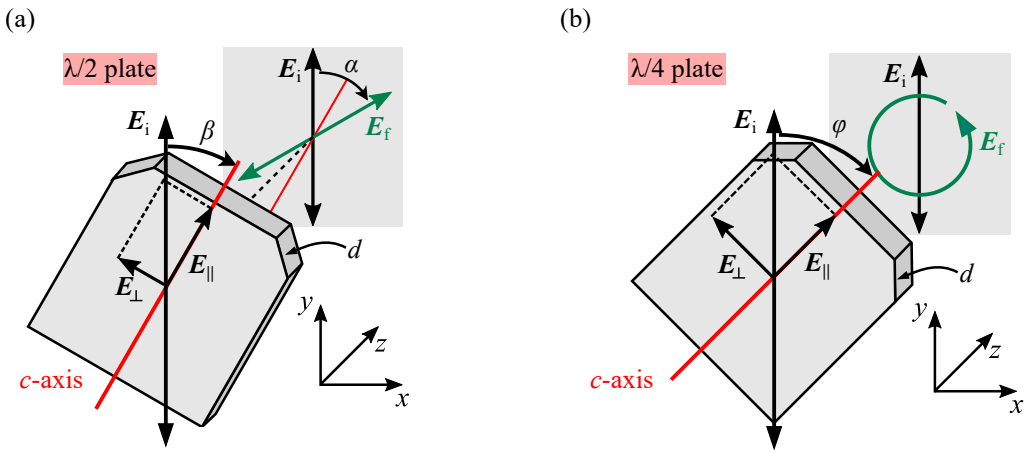

Figure 15: Sketch of the geometry of (a) $\lambda/2$ and $\lambda/4$-plates with Cartesian coordinates. Adapted from Ref. [90]

To control the polarization either $\lambda/2$ or $\lambda/4$-plates made of x-cut crystal quartz are used. The functionality of this birefringent plates is illustrated in Fig. 15 (a) and (b). Considering the $\lambda/2$-plate, panel (a), an incoming linearly polarized beam with an electric field vector $\boldsymbol{E}_\mathrm{i}$, oriented along the a-axis, is rotated with respect to the c-axis around an angle β. $\boldsymbol{E}_\mathrm{i}$ is composed of an ordinary beam $\boldsymbol{E}_{\mathrm{i}\perp}$ being perpendicular to the c-axis as well as an extraordinary beam $\boldsymbol{E}_{\mathrm{i}\parallel}$ being parallel. After passing the plate the two beam components

have different velocities since for THz radiation the refractive index n of quartz is different for the ordinary and the extraordinary axis, n_{o} and n_{eo}, respectively. Therefore, the beams exhibit a phase shift [93]

$$\Delta\phi = (2\pi d)/\lambda \cdot \Delta n \tag{45}$$

with the thickness of the plate d and $\Delta n = n_{\mathrm{eo}} - n_{\mathrm{o}}$. Here, two cases can be distinguished: If $\Delta\phi$ is an odd multiple of π the plate rotates the incident electric field vector E_{i} by an angle α being twice as big as the rotation angle β. These plates are well known as $\lambda/2$-plates, see Fig. 15 (a). This illustration shows that if β is a multiple of 90° the initial polarization state does not get influenced, i.e. $\boldsymbol{E}_{\mathrm{i}} = \boldsymbol{E}_{\mathrm{f}}$. In the second case $\Delta\phi$ is an odd multiple of $\pi/2$ and the incident radiation is converted into elliptically, or even circularly polarized light controlled by the angle φ with the plate known as $\lambda/4$-plate, see Fig. 15 (b). If the angle φ is chosen to be 45° or 135° the radiation becomes left- or right-handed circularly polarized, respectively, and at angles in between it becomes elliptically. In contrast, at $\varphi = 0°, \varphi = 90°$ and $\varphi = 180°$ the initial polarization remains unchanged, and is therefore linearly polarized.

The Stokes parameter describing the polarization state of a beam initially polarized along the y-axis ($\boldsymbol{E}_{\mathrm{i}} \parallel y$) and propagating along the z-axis can be expressed in terms of the rotation angles $\alpha = 2\beta$ for linear polarization. Exemplary, for the pulsed laser setup they are given by

$$\begin{aligned} \frac{s_1}{s_0} &= -\cos 2\alpha \\ \frac{s_2}{s_0} &= -\sin 2\alpha. \end{aligned} \tag{46}$$

For elliptical polarization with the rotating angle φ they are expressed by

$$\begin{aligned} \frac{s_1}{s_0} &= -\frac{\cos 4\varphi + 1}{2} \\ \frac{s_2}{s_0} &= -\frac{\sin 4\varphi}{2} \\ \frac{s_3}{s_0} &= \sin 2\varphi = -P_{\mathrm{circ}}, \end{aligned} \tag{47}$$

where P_{circ} defines the degree of circular polarization. Equations 46 and 47 help to analyse measurements performed with polarized radiation, where α or φ are varied. The last term which describes the degree of circular polarization P_{circ} vanishes if the radiation is linearly polarized.

Calibration and manipulation of radiation intensity To monitor the power P of the THz radiation during the measurements a beam splitter (Mylar sheet) is placed in the optical path and the reflected part is focused onto a photon drag power detector [29], see Fig. 14(a). Since the power on the reference detector position slightly differs to that at the sample position calibration measurements are performed. To do so a second reference detector is placed at the sample position and then the ratio between the part reflected at the beam splitter and the transmitted part can be calculated. Taking this ratio into account, which varies for different setups and radiation frequencies, the power entering the sample during measurements can be determined. To calculate the intensity at the sample position, it is also important to monitor the spatial beam profile, typically done with a pyroelectric camera. Consequently, the radiation intensity can be calculated as

$$I = \frac{P}{A} \tag{48}$$

with the area A of the Gaussian beam. Note that this parameter may also change with radiation wavelength and laser setup.

To study THz induced optoelectronic phenomena it is fundamental to measure intensity dependencies. In this work, the control of the intensity exciting the sample was done by means of crossed linear polarizes. First the linearly polarized radiation coming from the laser passes through a rotatable polarizer resulting in a decrease of the radiation intensity and the rotation of the polarization state. Then it passes through a second polarizer, which has a fixed position. This on the one hand causes a further decrease of the radiation intensity and on the other hand returns the polarization state to the initial one.

Measurement configurations All components of the experimental setup are connected to a computer via GPIB (General Purpose Interface Bus) allowing to control them during the measurements with a software written in Labview. The electronic setups of the pulsed an cw THz laser setups are slightly different. In the first case signals coming from the sample are amplified and then further processed by a digital storage oscilloscope. In the cw laser setup a chopper was placed additionally in the optical path allowing to use standard lock-in technique to process the photosignals.

The THz radiation induced photosignals were measured as a voltage drop over load resistors, see exemplary setups in Figs. 14. Figure 14(b) shows a photocurrent measurement where the detected photovoltage U is proportional to the photocurrent J. Here no external bias voltage is applied while for the photoconductivity measurements, as exemplary shown for circularly polarized radiation in Fig. 14(c), an external dc bias voltage V^{dc} is applied perpendicular to the measurement direction. In some measurements a two terminal photoconductivity setup was used where the signal is picked up in same direction as the bias voltage was applied.
By definition, the linear-in-V^{dc} signal has opposite signs for opposite bias voltage polarities whereas the photogalvanic current is independent of the V^{dc} polarity. Consequently, the photoconductivity signal U_{pc} can be extracted as

$$U_{\mathrm{pc}} = \frac{U(V^{\mathrm{dc}}) - U(-V^{\mathrm{dc}})}{2}. \tag{49}$$

For the two terminal measurements of the photoconductivity signal, the relative photo-induced change in conductivity $\Delta\sigma$ normalized to the dark conductivity σ was calculated.

4 CR-enhanced photovoltage in HgTe topological insulators

In this chapter experiments on HgTe-based three-dimensional topological insulators are presented and discussed. It starts with the experimental results, where the observation of cyclotron resonances in samples with different HgTe thickness is outlined. After that the discussion of the data is given which also includes the introduction of the theory behind. All results in this chapter are obtained using the cw terahertz laser. The corresponding data are published in Ref. [30].

4.1 Experimental results

By applying normally incident THz radiation to three-dimensional HgTe topological insulators a strong enhancement of the photocurrent under cyclotron resonance condition can be observed [30, 38]. Complementary measurements of the radiation transmission [38, 39, 94] by placing a pyroelectric detector behind the sample support the analysis of the photocurrent data. The photocurrent J was studied in the presence of a magnetic field up to 7 T and picked up across the sample as Photovoltage $U_{x,y} \propto J_{x,y}$, see Fig. 14(b).
To analyse the transmission data obtained from the HgTe samples fit functions were used. Before presenting the experimental results the model behind the fit functions is briefly addressed, for review see Refs. [95–99].

Transmission fits The excited sample is assumed as a dielectric plate with a thickness w, which represents the thick GaAs substrate having a refractive index of $n = 3.6$. The, in comparison, negligibly thin HgTe layer on top of the substrate hosts conducting surface and bulk carriers. The incident radiation with a frequency of $\omega/2\pi$ is considered circularly polarized and hits the sample at a normal incidence. In order to describe the THz wave transmitted through the sample, one needs to take into account possible multiple reflections between the dielectric interfaces (Fabry-Perot interferences) since the optical phase shift $\phi = n\omega w$ across the substrate is much larger than unity. These interferences influence the electrons in the HgTe layer and may result in a deviation of the CR dip from a symmetrical Lorentzian form (see Sec. 4.2 below). The power

transmission can be written as [95, 96]

$$T = \left| (1+\tilde{\sigma})\cos\phi - i\frac{1+n^2+2\tilde{\sigma}}{2n}\sin\phi \right|^{-2} \tag{50}$$

with ϵ_0 being the vacuum permittivity and the dimensionless parameter $\tilde{\sigma} = \sigma/2\epsilon_0 c$ where $\sigma = \sigma_{xx}(\omega) + i\sigma_{xy}(\omega)$ is the complex dynamic conductivity. Note that in HgTe an isotropic transport is assumed, meaning that $\sigma_{xx} = \sigma_{yy}$ and $\sigma_{yx} = -\sigma_{xy}$. Within the Drude model the ac conductivity is given by

$$\sigma_{\pm} = \frac{e^2 n_e/m}{\tau^{-1} - i(\omega \pm \omega_c)} \tag{51}$$

where τ is the momentum relaxation time and $\omega_c = eB_{\mathrm{CR}}/m$ the cyclotron frequency. From this follows

$$\tilde{\sigma} = \frac{\Gamma}{\gamma - i(1 \pm \omega_c/\omega)}. \tag{52}$$

Here, Γ represents the radiative decay rate [96–99] which is given as

$$\Gamma = \frac{e^2 n_e}{2\epsilon_0 cm\omega} = \frac{0.301\mathrm{T}}{B_{\mathrm{CR}}}\frac{n_e}{10^{12}\,\mathrm{cm}^{-2}}. \tag{53}$$

From this it becomes apparent that Γ only depends on the electron density n_e and the cyclotron resonance magnetic field B_{CR}. On the other hand

$$\gamma = \frac{1}{\omega\tau} = \frac{1}{\mu B_{\mathrm{CR}}} \tag{54}$$

is determined by τ and the corresponding mobility μ. Thus, the transmitted power, Eq. (50), depends on the Fabry-Perot interference phase ϕ, the cyclotron masses, carrier densities and corresponding carrier mobilities. If several carrier types contribute to transport, $\tilde{\sigma}$ is written as the sum of the respective conductivities of the different transport channels. The above equations are valid for left-handed circularly polarized radiation an can be translated to right-handed polarization by substitution ($\omega_c \to -\omega_c$).

After the introduction of the fit functions employed to analyse the transmission data the experimental findings are presented in the following. Irradiation of samples based on 200 nm thick HgTe films with THz radiation results in the observation of two distinct resonances in the photovoltage $U_{x,y} \propto J_{x,y}$ at

magnetic fields $B_{\mathrm{CR1}} = 1.6\,\mathrm{T}$ and $B_{\mathrm{CR2}} = 2.5\,\mathrm{T}$, see Fig. 16(a). The data were obtained at $T = 30\,\mathrm{K}$ and with normally incident THz radiation (circularly and linearly polarized) with a frequency of $f = 1.63\,\mathrm{THz}$ and the magnetic field applied perpendicular to the sample surface.

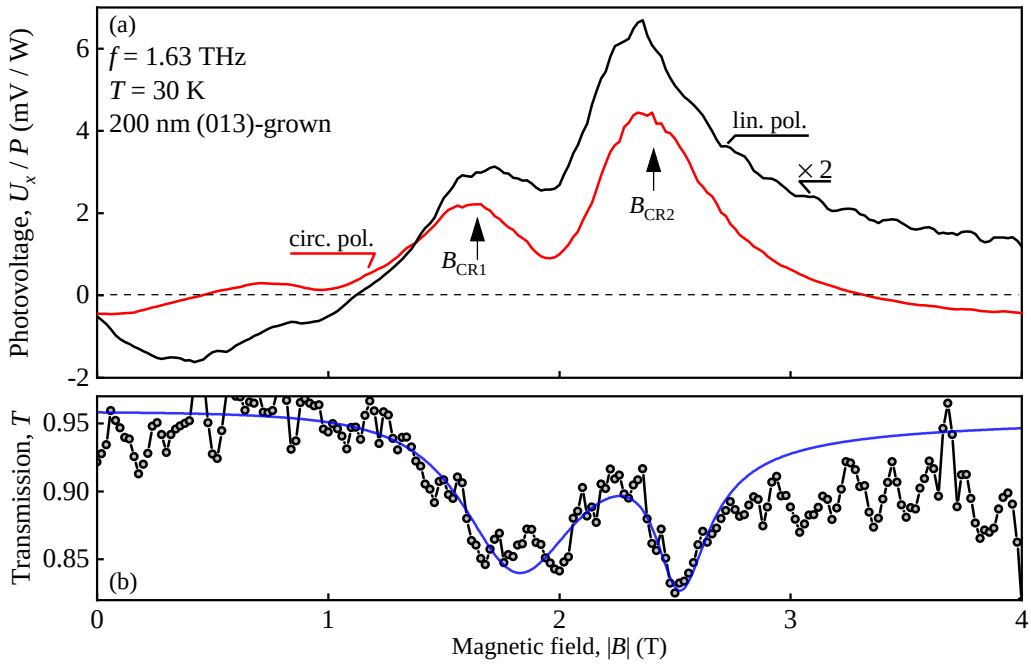

Figure 16: (a) Magnetic field dependence of the photosignals $U_x \propto J_x$ excited with linearly and circularly polarized light. (b) Radiation transmission. Data were obtained on a 200 nm HgTe film (wafer #B) at $T = 30\,\mathrm{K}$ and at a radiation frequency $f = 1.63\,\mathrm{THz}$. Solid line in (b) shows a fit after Eq. (50) and (52) with fitting parameters: $B_{\mathrm{CR1}} = 1.8\,\mathrm{T}$ and $B_{\mathrm{CR2}} = 2.5\,\mathrm{T}$; $\phi = 8°$; $n_1 = 1.0 \times 10^{11}\,\mathrm{cm}^{-2}$ and $n_2 = 0.4 \times 10^{11}\,\mathrm{cm}^{-2}$; $\mu_1 = 3.5 \times 10^4\,\mathrm{cm}^2/\mathrm{Vs}$ and $\mu_2 = 8 \times 10^4\,\mathrm{cm}^2/\mathrm{Vs}$. Adapted from Ref. [30]

For circularly polarized radiation, the resonances appeared only for one magnetic field polarity, see Fig. 17. For right-handed circular polarization, σ^+, they emerge at positive fields, and for left-handed circular polarization, σ^-, at negative magnetic fields. Using linear polarization which is described by a superposition of left and right-handed circular polarizations, the resonances were consequently detected for both magnetic field polarities. The simultaneously measured radiation transmission is presented in Fig. 16(b) and shows dips at similar magnetic fields as the resonant features observed in U_x. The transmission fit shown as solid blue line in Fig. 16(b) is based on Eqs. (50) and (52) introduced above. Corresponding fit parameters, B_{CR1} and B_{CR2}, carrier densities, and mobilities of top and bottom surface states as well as the Fabry-Perot interference phase ϕ are given in the caption of Fig. 16.

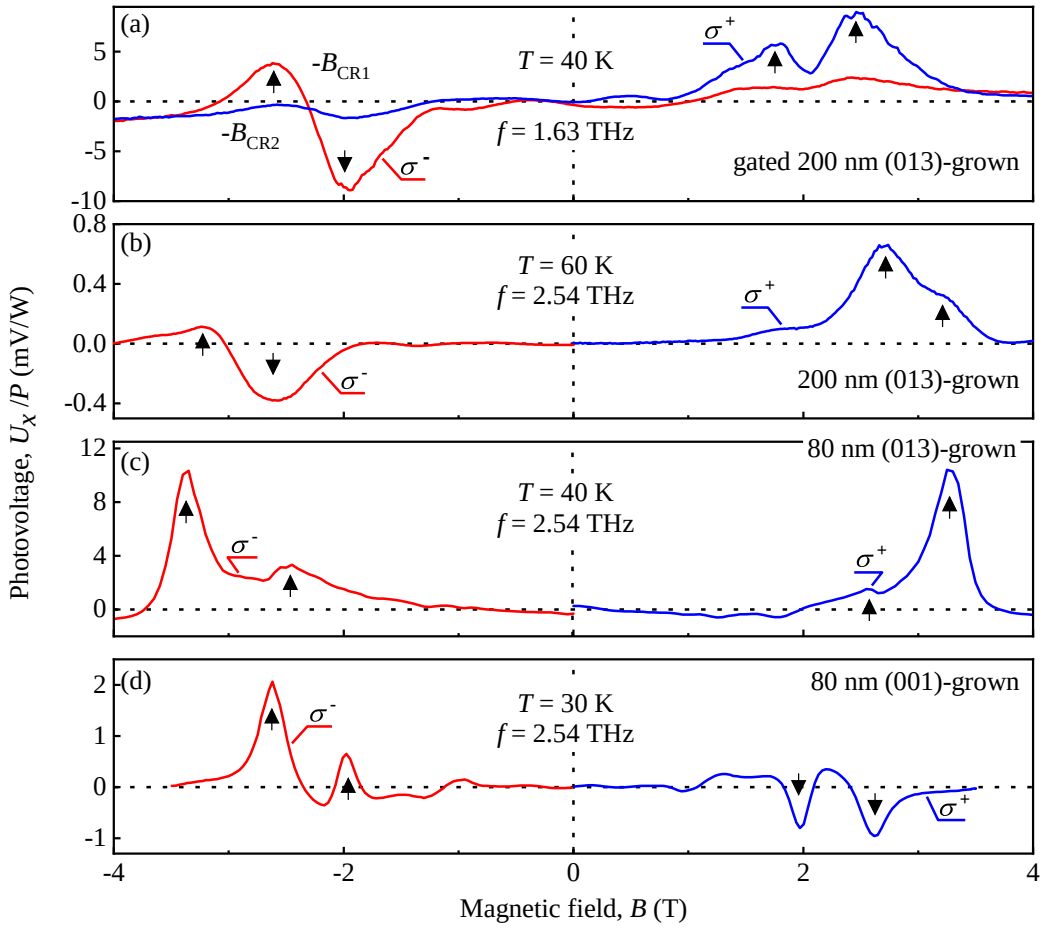

Figure 17: Photovoltage U_x as a function of the magnetic field for various samples with different HgTe film thicknesses, different crystal orientations and different measurement temperatures. (a) Photosignal in a gated 200 nm thick film for σ^+ and σ^- polarized light with frequency $f = 1.63\,\mathrm{THz}$. Panels (b) to (d) show typical resonances detected in the various samples with excitation frequency $f = 2.54\,\mathrm{THz}$. Adapted from Ref. [30]

In addition to the 200 nm HgTe samples, films with a thickness of 80 nm were studied. Qualitatively similar results were observed in these thinner films. Figure 17 shows an overview of the photovoltage measured in different samples with different thicknesses of the HgTe film and different crystal orientations of the GaAs substrate. In all samples two well separated resonances are detected which exhibit similar polarization dependencies. Notably, the resonant photocurrent can either be positive or negative, depending on the experimental conditions. This is e.g. seen in Fig. 17(a) where the sign of the resonant photocurrent is the same at magnetic fields $+B_{\mathrm{CR2}}$ and $-B_{\mathrm{CR2}}$ but different at magnetic fields $+B_{\mathrm{CR1}}$ and $-B_{\mathrm{CR1}}$.

While in the photocurrent signals, the resonances always appear as two

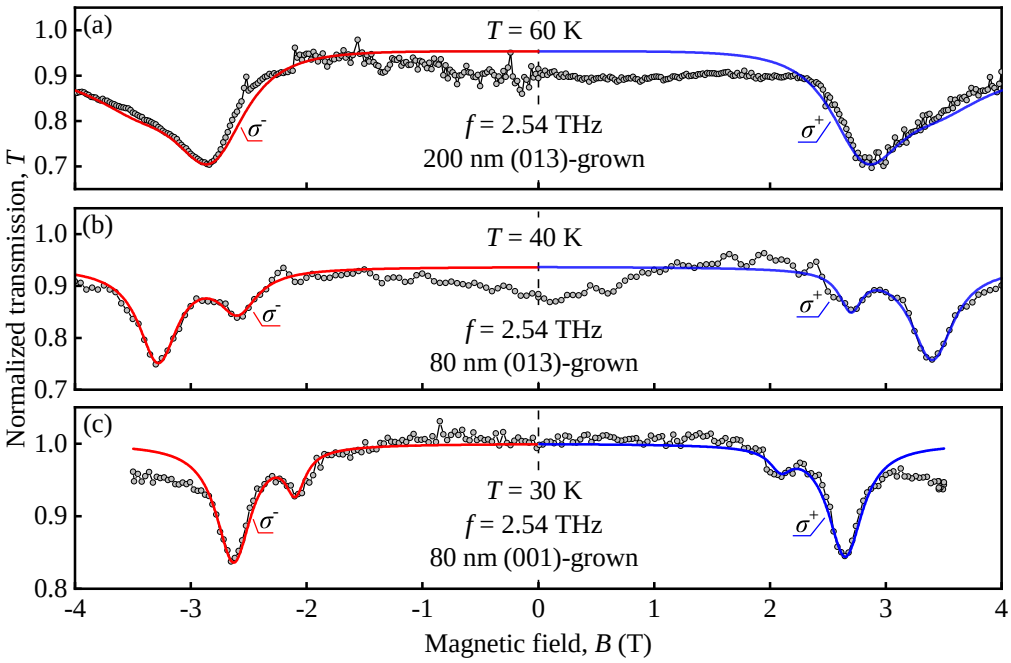

Figure 18: Normalized transmission as a function of the perpendicular applied magnetic field obtained for right-handed (positive B) and left-handed (negative B) polarized radiation on various samples with different HgTe thickness and at different temperatures. Solid lines show fits after Eq. (50) and (52). The fitting parameters are: Panel (a) $B_{\mathrm{CR1}} = 2.8\,\mathrm{T}$ and $B_{\mathrm{CR2}} = 3.4\,\mathrm{T}$; $\phi = 12°$; $n_1 = 2.5 \times 10^{11}\,\mathrm{cm}^{-2}$ and $n_2 = 0.7 \times 10^{11}\,\mathrm{cm}^{-2}$; $\mu_1 = 3 \times 10^4\,\mathrm{cm}^2/\mathrm{Vs}$ and $\mu_2 = 2.3 \times 10^4\,\mathrm{cm}^2/\mathrm{Vs}$; panel (b) $B_{\mathrm{CR1}} = 2.6\,\mathrm{T}$ and $B_{\mathrm{CR2}} = 3.3\,\mathrm{T}$; $\phi = 0°$; $n_1 = 0.8 \times 10^{11}\,\mathrm{cm}^{-2}$ and $n_2 = 0.34 \times 10^{11}\,\mathrm{cm}^{-2}$; $\mu_1 = 5.6 \times 10^4\,\mathrm{cm}^2/\mathrm{Vs}$ and $\mu_2 = 10 \times 10^4\,\mathrm{cm}^2/\mathrm{Vs}$; and panel (c) $B_{\mathrm{CR1}} = 2.1\,\mathrm{T}$ and $B_{\mathrm{CR2}} = 2.6\,\mathrm{T}$; $\phi = 0°$; $n_1 = 0.5 \times 10^{11}\,\mathrm{cm}^{-2}$ and $n_2 = 0.1 \times 10^{11}\,\mathrm{cm}^{-2}$; $\mu_1 = 6 \times 10^4\,\mathrm{cm}^2/\mathrm{Vs}$ and $\mu_2 = 10 \times 10^4\,\mathrm{cm}^2/\mathrm{Vs}$. Adapted from [30]

separated extrema, in complementary radiation transmission the dips tend to merge at higher temperatures, see Fig. 18. In the 200nm film, the observed resonances appear as a merged resonance at $T = 60\mathrm{K}$, whereas below $T = 40\mathrm{K}$ the two resonances are well resolved in all studied samples, see Fig. 18 and 16(b).

For further analysis different laser lines were applied resulting in different resonance positions $B_{\mathrm{CR1,2}}$, see Fig. 19(a). The positions scale linearly with the frequency f for all HgTe devices studied. Together with the polarization dependencies and the observations in magnetotransmission it can be concluded that the observed features in the photovoltage stem from cyclotron resonance.

Depending on the experimental conditions the observed CR enhanced photocurrents can be positive or negative. Figure 20 shows typical photovoltage

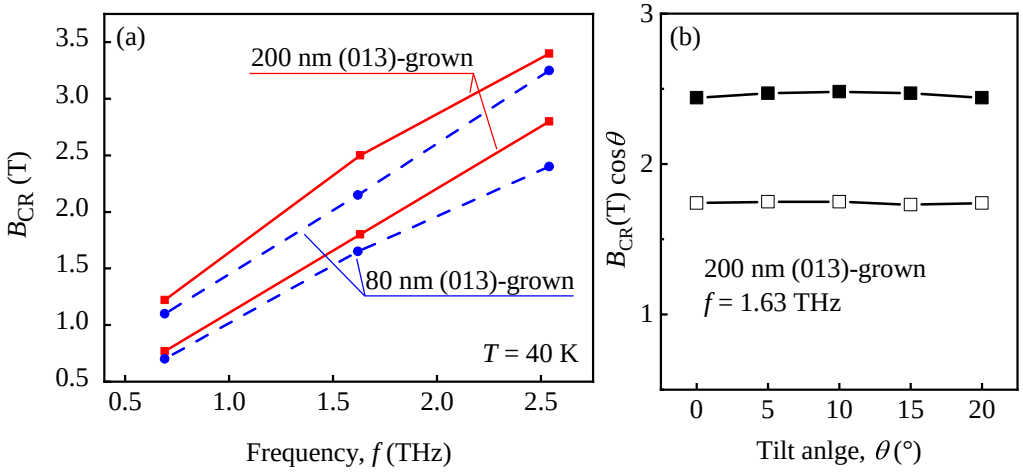

Figure 19: (a) Magnetic field position at cyclotron resonance as a function of the frequency f detected from transmission measurements in two different samples. (b) Dependence of the magnetic field's z-component $B_{\mathrm{CR1,2}} \cos\theta$ on the tilt angle θ. Adapted from Ref. [30]

traces measured in x- and y-direction. Here, panels (a) and (b) show data obtained on the same sample, based on a 200 nm thick HgTe film, at different temperatures. While at $T = 40\,\mathrm{K}$ the photocurrent at B_{CR1} has different polarities for the two perpendicular directions, it has the same at B_{CR2}. On the other hand, at $T = 60\,\mathrm{K}$ the direction of the photocurrent is opposite at both CR positions. Moreover, the current can have opposite signs for the same measurement directions, see e.g. Fig. 17, where it has opposite polarity at $\pm B_{\mathrm{CR1}}$ but same polarity at $\pm B_{\mathrm{CR2}}$. Changes of the observed photocurrent sign under experimental conditions like temperature or frequency have also been reported previously in HgTe QWs with and without magnetic field [38, 100]. A sketch of the photocurrent projections in x- and y-direction measured in the experiment together with the total photocurrent $\boldsymbol{J}$ are shown in the inset of Figs. 20(a) and (b).

To get evidence whether the CR traces in the photocurrent stem from two-dimensional or three-dimensional states measurements with a tilted magnetic field were performed. Therefore the sample was rotated by an angle θ and the CR positions B_{CR1} and B_{CR2} were detected. By increasing the angle θ, the resonances shift to higher magnetic fields, which indicates that they are determined by the magnetic field component B_z normal to the sample surface. Indeed, calculating the z-component of the fields $B_{\mathrm{CR1,2}}$ the positions $B_{z,\mathrm{CR1,2}}$ do not change with the angle θ, see Fig. 19(b). This is a clear evidence that the detected cyclotron resonance traces in photocurrent and transmission

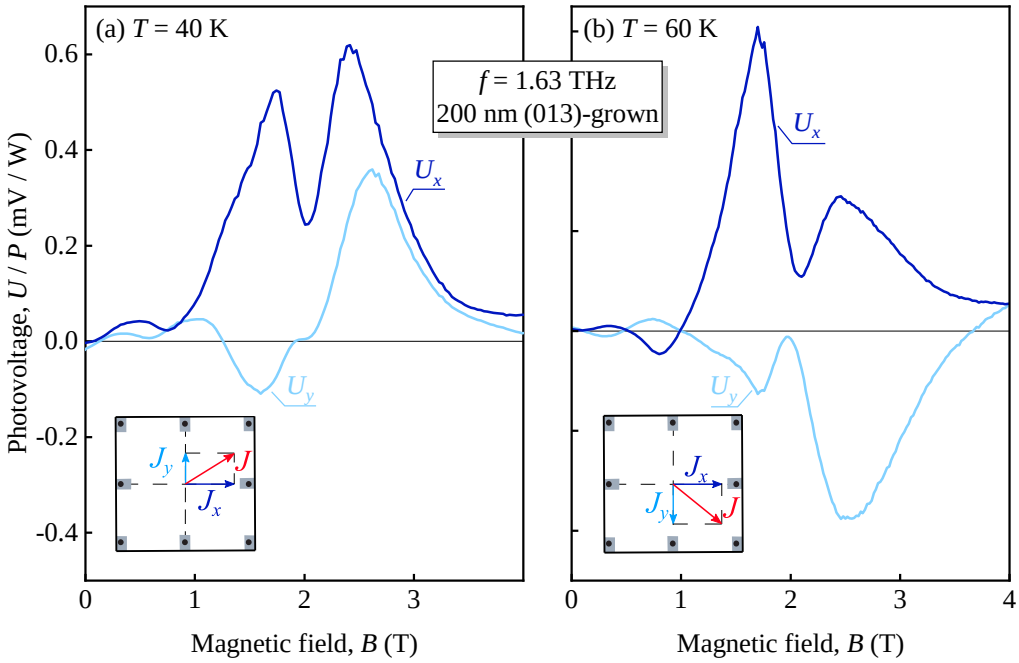

Figure 20: Magnetic field dependencies of the photosignal $U \propto J$ measured in x and y-direction at (a) $T = 40\,\mathrm{K}$ and (b) $T = 60\,\mathrm{K}$. The insets display the direction of the total photocurrent (red arrow) and its projections in x- and y-direction (horizontal and vertical arrows). Adapted from Ref. [30]

stem from carriers occupying the two-dimensional surface states and not from bulk carriers. An overview of the detected cyclotron resonance positions with corresponding masses in various HgTe systems is given in Tab. 3.

Sample	B_{CR1}, (T)	B_{CR2}, (T)	m_{CR1}/m_0	m_{CR2}/m_0
200 nm HgTe (013)	1.8	2.5	0.031	0.043
80 nm HgTe (013)	1.6	2.2	0.028	0.038
80 nm HgTe (001)	1.3	1.7	0.023	0.030

Table 3: Cyclotron resonance position and corresponding cyclotron masses extracted from transmission measurements on various samples at $T = 40\,\mathrm{K}$ and with $f = 1.63\,\mathrm{THz}$.

Furthermore, measurements of the CR enhanced photocurrent at different Fermi level positions were performed. In order to do so, samples based on 200 nm thick HgTe films with a semitransparent gate were fabricated. Figure 21(a) shows photovoltage measurements as a function of the magnetic field for various effective gate voltages $U_{\mathrm{g}}^{\mathrm{eff}}$. It shows that on the one hand, the resonance at B_{CR1} shifts to higher magnetic fields with increasing $U_{\mathrm{g}}^{\mathrm{eff}}$, and, on the

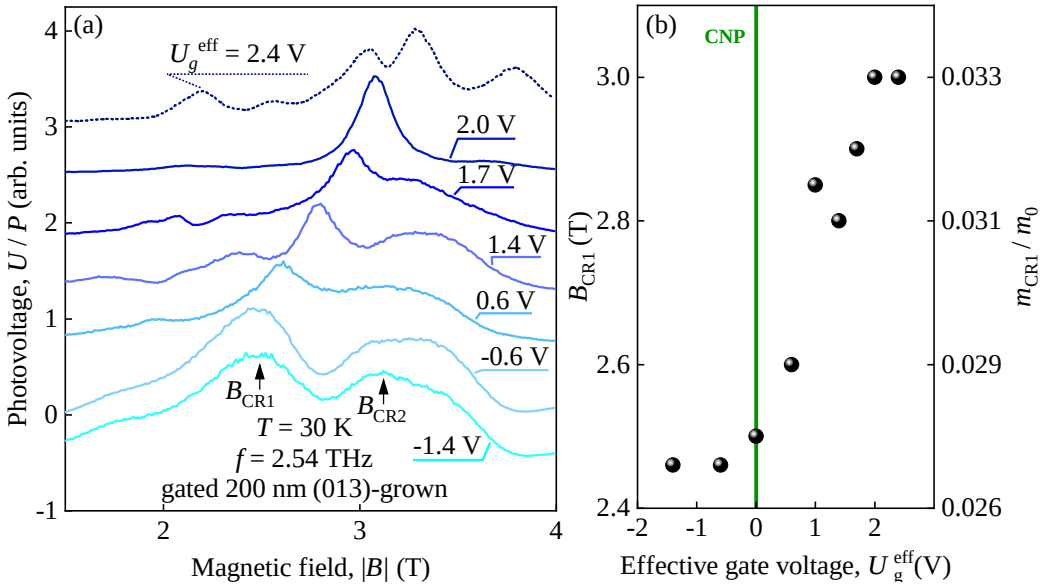

Figure 21: (a) Photosignal U as a function of the magnetic field B for various effective gate voltages $U_g^{eff} = U_g - U_g^{CNP}$. Data are vertically shifted for clarity. (b) The extracted positions B_{CR1} as a function of U_g^{eff} with U_g^{CNP} shown as vertical green line. The right axis shows the corresponding cyclotron masses m_{CR1} normalized to the electron mass m_0. Adapted from Ref. [30]

other hand, the position of the second resonance B_{CR2} almost stays the same. In general, in systems with linear dispersion the cyclotron resonance position B_{CR} depends on the Fermi level position for $\varepsilon_F < \hbar\omega_c$ which is in contrast to systems with parabolic dispersion. However, the independence of B_{CR2} on U_g^{eff} demonstrates that the carrier density of only one surface gets influenced by the gate voltage. This was already observed in previous works on CR in 80 nm HgTe films [38], as well as in magnetotransport measurements of 80 nm [83] and 200 nm thick HgTe films [40]. Due to electrostatic screening of the bottom surface by the top one the filling rates dN_s/dU_g for the top and bottom surface states are substantially different. Consequently, the resonance at B_{CR2} can be attributed to the bottom surface and the one at B_{CR1} to the top. The shifting of the top carrier resonance upon variation of the gate voltage becomes clearly visible in Fig. 21(b) where the corresponding positions B_{CR1} are plotted. From this the cyclotron masses of the top surface states were determined and are depicted on the right axis.

Previous measurements on fully strained 80 nm thick HgTe films [38, 83] provide additionally support to the conclusion that the cyclotron resonances come from top and bottom surface states. Here it was shown that these systems

are 3D topological insulator exhibiting a gap between valence and conduction band. Reference [38] reports on the observation of two separate CR traces in transmission as well as in the photocurrent originating from top and bottom interfaces of the HgTe film. Comparing the resonant peak positions, see table 3, extracted from transmission measurement shown in Fig. 18, it is conspicuous that the positions $B_{\mathrm{CR1,2}}$ in the 200 nm thick HgTe filme with (013) crystal orientation match up well with that in the 80 nm thick HgTe film having the same substrate orientation. This coincidence is a further indication that resonances coming from top and bottom surfaces can also be detected in samples having a thicker HgTe film. The resonance positions in the 80 nm thick HgTe film with (001) crystal orientation lie at about 25% lower magnetic fields. However, they exhibiting the same characteristic properties as the samples with (013) crystallographic orientation like helicity sensitivity and linear frequency dependence, see Figs. 17(d) and 18(c).

4.2 Discussion

As addressed above, the two features observed in photovoltage as well as transmission data can be attributed to cyclotron resonance of top an bottom surface states of the investigated HgTe film. In fact, this observation is not obvious in HgTe films with 200 nm thickness, where the lattice mismatch-induced strain was expected to be already relaxed [37, 83]. Therefore, in this chapter the CR response is further analysed as well possible reasons for the remaining partial strain are discussed. Moreover, the origin of the CR-enhanced photocurrent in (013)-grown films is presented and the observed differences in its sign are explained in more detail.

Strain relaxation in 200 nm thick HgTe films The conclusion that traces of the surface states in 200 nm thick HgTe films can be detected, despite the thickness being larger than the estimated critical thickness for lattice relaxation [37, 83] arise from the following facts: (i) two-dimensional origin of the CR (Fig. 19 b), (ii) observation of two CRs attributed to excitation of top and bottom surface states (see Figs. 16, 17, 19 and 20) and (iii) good coincidence of the cyclotron masses for both resonances obtained in (013)-oriented 200 nm and 80 nm thick HgTe films (Fig. 19). Furthermore, the magnetotransport, magnetocapacitance and x-ray measurements performed in Ref. [40] support this reasoning. In this work [40], Shubnikov–de Haas (SdH) oscillations in

both conductivity and capacitance are analysed which makes it possible to distinguish the different electrons contributing to transport, namely the ones occupying states in the bulk as well as on top and on the bottom surface. It was demonstrated that on the one hand the surface states are spin nondegenerate whereas on the other hand the bulk electrons are spin degenerate. Moreover, the X-ray measurements, briefly introduced in chap. 3.1.1, show that about 60% of the strain remains.

To understand the origin of the remaining strain one has to consider the calculations of the critical thickness for lattice relaxation which usually are performed in the framework of Matthews model [101]. This approximation is an equilibrium thermodynamic approach to the formation of misfit dislocations in epitaxial grown thin films where kinetic factors associated with the formation of misfit dislocations at a finite rate of epitaxial growth are neglected. Above a specific critical thickness, the strain partially relaxes by the generation of energetically more favourable dislocations at the interface. For a large lattice mismatch between the substrate and the epitaxially grown layer, this model is in good agreement with experimental findings. However, it becomes more imprecisely for small lattice misfits, which are typical for HgTe/CdTe heterostructures. The discrepancy between the existing models and the experimental data was already observed in low-misfit semiconductor systems [102, 103]. For instance, it was demonstrated that the difference between experimentally obtained and calculated values of the critical thickness in Ge_xSi_{1-x}/Si is about two orders of magnitude [104].

Another factor that should be considered in calculations of the critical thickness is the substrate orientation. For example, reported theoretical values of HgTe grown on (001)-oriented CdTe having a lattice mismatch of about 0.3% lie between 50 nm [105] to 200 nm [37, 106, 107]. Looking at values reported on $Hg_{0.7}Cd_{0.3}Te$ on (013)-oriented CdTe (which have a lattice mismatch of about 0.216%) the situation is similar, and the critical thickness range from 47.5 nm to 344 nm for 12 possible slip systems of dislocations [108]. In Ref. [108] it was experimentally observed that the formation of dislocations, necessary for the system to relax the strain, start at about 80 nm thickness and at 150 nm the strain is relaxed by about 40%.

Another important factor that should not be disregarded are the intermediate ZnTe and CdTe layers introduced to retain the crystal orientation of the HgTe layer [108]. The consideration of such multilayer heterostructures is very complex because the substrate and the different epitaxial layers have differ-

ent thermal expansion coefficients. Since the samples are cooled down to low temperatures in the experiment, this presents a further parameter that can influence the cirtical thickness. All these effects reinforce the assumption that some residual strain remains even in thicker thicker HgTe films.

Evaluation of transmission data The transmission fits applied in Fig. 16 and 18 are based on Eqs. (50) and (52). As it was introduced in chapter 4.1, the transmitted power depends on the Fabry-Perot interference phase ϕ, the cyclotron masses and the densities and mobilities of the carriers. Knowledge of these parameter allows an advanced analysis of the cyclotron resonances in the transmitted power. The corresponding used fit parameters are provided in the captions of the figures which present transmission data. Taking a closer look at the shape of the CR dips in transmission, it is conspicuous that it often is asymmetric, and therefore, deviates from a symmetric Lorentzian form, see for example Fig. 18(a). Responsible for this effect are the Fabry-Perot like interferences of the THz radiation between substrate and HgTe layer introduced in the fit functions as the optical phase shift ϕ. If ϕ/π is close to an integer value, one obtains constructive interference whereas for half-integer values, destructive interference prevails. Note that only in case of either constructive or destructive interference, a Lorentzian shape of the resonance can be observed.

Another parameter that influences the shape of the CR traces in transmission are the superradiant decay rate Γ which depends on the carrier density, and γ which is proportional to the inverse carrier mobility. These two parameters affect the broadening of the dip and have similar values in the fits used in this work. The different shapes of the CR dips at different temperatures, e.g. at $T = 30\,\mathrm{K}$ in Fig. 16 showing two separated sharp dips, and at $T = 60\,\mathrm{K}$ in Fig. 18(a) showing one merged broad dip, are in line with transport data presented in Fig. 10(b). While the carrier density ($\propto \Gamma$) increases for higher temperatures, the mobility ($\propto 1/\gamma$) decreases. The employed fit parameters are in good agreement with the characteristic parameters reported in Ref. [40]. Here, the carrier densities and corresponding mobilities from surface and bulk carriers were separately determined from magentotransport measurements. Analysis of the transmission data shown above yields an electron density of the carriers occupying the top surface states being about three times larger than the density in the bottom surface. This result is very similar to the one obtained in the magnetotransport characterisation, shown in Fig. 3 in Ref. [40].

Origin of CR enhanced photocurrent The origin of the enhanced photocurrent under cyclotron resonance condition has already been studied and theoretically described in different material systems. It was detected for example in InSb/InAlSb quantum wells (QW)s [109], in 3D TI HgTe strained films [38] and in HgTe QWs having either the critical thickness (≈6.6 nm) or slightly larger [23]. The phenomenological description of this effect is similar for all these systems. The underlying microscopic origin, however, is not universal because it is sensitive to the band dispersion and can have spin as well as orbital degrees of freedom. In the following, the theoretical model for photocurrent generation in systems with linear dispersion provided by Dr. G. V. Budkin from the Ioffe Institute in St. Petersburg is presented. It is based on the process of asymmetric energy relaxation of photoexcited carriers in the presence of a magnetic field which is well known for two-dimensional systems lacking spatial inversion symmetry [110].

In the samples under study the extension of the wave function of both surface states is much smaller than the thickness of the HgTe film, which allows one to neglect the coupling between the surface states. Therefore, the process of energy relaxation of top and bottom surface states can be considered independently. The incident THz radiation heats up the spin nondegenerate 2DEG and after that the photoexcited carriers begin to relax. In the regime of low temperatures relevant for this work, on the one hand, the energy relaxation is dominated by the interaction of the carriers with acoustic phonons and, on the other hand, their momentum relaxation appears mainly due to elastic scattering on static defects.
The THz radiation incident on the HgTe samples is partially absorbed by the charge carriers in the film. After that the carriers provide the energy to the phonon bath. This energy transfer is naturally accompanied by a heating of the electron subsystem. It is assumed that frequent collisions between electrons support a fast exchange of the energy and result in a thermalization of the photoexcited carriers. Due to this assumption, the isotropic part of the steady-state nonequilibrium distribution function can be written as: $f_k^{(0)} = 1/[\exp((\varepsilon_k - \varepsilon_F)/T_e) + 1]$ coming from Fermi-Dirac statistics. Here, k and ε_k are the momentum and energy dispersion of the electrons, respectively, and ε_F is the chemical potential. The effective temperature of the electron bath, given by $T_e = T + \Delta T$, is assumed to be higher than the one of the phonon bath T.

In the presence of a magnetic field the electron scattering in momentum space is asymmetric leading to an anisotropic correction δf_k to $f_k^{(0)}$ which can be extracted from the Boltzmann equation

$$\frac{\delta f_k}{\tau} + \frac{e}{\hbar}[\boldsymbol{v}_k \times \boldsymbol{B}]\frac{\partial \delta f_k}{\partial \boldsymbol{k}} = \mathrm{St}^{(\mathrm{ph})}[f_k^{(0)}]. \tag{55}$$

This equation consists of three parts: the first one is attributed to the momentum relaxation with τ being the transport relaxation time, the second one to the cyclotron motion with group velocity $\boldsymbol{v}_k$, and the third part describes the electron-phonon collision with its integral $\mathrm{St}^{(\mathrm{ph})}$ where the full distribution function is replaced by $f_k^{(0)}$. This is the leading first-order pertubation theory where the anisotropic correction δf_k involves a weak asymmetry in the electron-phonon collision integral $\mathrm{St}^{(\mathrm{ph})}$. The latter one is given by [111]

$$\mathrm{St}^{(\mathrm{ph})}[f^{(0)}] = \sum_{\boldsymbol{k'},\boldsymbol{q},\pm} W^{\pm}_{k'k}(\boldsymbol{q}) f^{(0)}_{k'}(1-f^{(0)}_k)N^{\pm}_q - W^{\pm}_{k'k}(\boldsymbol{q}) f^{(0)}_k(1-f^{(0)}_{k'})N^{\pm}_q. \tag{56}$$

Here, $W^{\pm}_{k'k}(\boldsymbol{q}) = \frac{2\pi}{\hbar}|M^{\pm}_{k'k}(\boldsymbol{q})|^2\delta(\varepsilon_{k'} - \varepsilon_k \pm \hbar\Omega_q)$ is the the scattering rate with the matrix elements $M^{\pm}_{k'k}(\boldsymbol{q})$ being Hermitian conjugates $M^{-}_{k',k}(\boldsymbol{q}) = |M^{+}_{kk'}(\mathbf{q})|^*$. The phonon wave vector is defined by $\boldsymbol{q}$, and the phonon occupation numbers by N^-_q and $N^+_q = N^-_q + 1$ where $\pm$ is attributed to phonon emission/absorption.

The photocurrent is given by

$$\boldsymbol{j} = e\sum \boldsymbol{v}_k f_k \tag{57}$$

with the anisotropic correction δf_k obtained from Eq. (55).

If no static magnetic field is applied to the system, the time reversal symmetry (TRS) holds and the current is absent. In turn, if the system is exposed to a magnetic field, the inversion of the magnetic field direction appears in the time-reversal operation $W^{-}_{k'k}(\boldsymbol{q}, \boldsymbol{B}) = W^{-}_{-k'-k}(-\boldsymbol{q}, -\boldsymbol{B})$ resulting in an asymmetry of the electron scattering on phonons. The matrix elements of the scattering rate can be written in the lowest order correction proportional to B_z

$$|M^{-}_{k'k}(\boldsymbol{q})|^2 = \delta_{\boldsymbol{k'},\boldsymbol{k}+\boldsymbol{q}_{||}}[\omega_o + \omega_1 B_z \boldsymbol{g}\cdot(\boldsymbol{k'}+\boldsymbol{k})], \tag{58}$$

where $\delta_{\boldsymbol{k'},\boldsymbol{k}+\boldsymbol{q}_{||}}$ is the Kronecker delta describing the momentum conservation law, $\boldsymbol{q}_{||}$ the in-plane component of the phonon momentum, ω_0 corresponds to

scattering at $B = 0$, and the scattering anisotropy is described by the in-plane vector $\boldsymbol{g}$. The phenomenology of this asymmetry in electron scattering is the same as reported in QWs in Ref. [112] or for the spin-dependent scattering described in Refs. [113–115]. Two-dimensional systems on (013)-oriented surfaces, as studied in this work, belong to the C_1 point group where any nontrivial symmetry elements are absent. In this specific case, the two-dimensional vector $\boldsymbol{g}$ does not have any restrictions regarding its orientation.

The fact that the out-of-plane component of the phonons is typically large, i.e. $q_z \gg |k - k'| = q_{||}$, allows an explicit summation in Eq. (57) over $\boldsymbol{k}, \boldsymbol{k'}$ and $\boldsymbol{q}$ with usage of the scattering probability given in Eq. (58). Altogether, the photocurrent can be written as

$$\boldsymbol{j} = -eI\eta(\omega)B_z \frac{\boldsymbol{g} + \omega_c\tau\boldsymbol{g}_\perp}{1+\omega_c^2\tau^2}\xi\frac{\langle|q_z|\omega_1\rangle}{\langle|q_z|\omega_0\rangle} \tag{59}$$

with the cyclotron frequency $\omega_c = eB_z/m$, the in-plane vector $\boldsymbol{g}_\perp$ normal to $\boldsymbol{g}$, the average over q_z and the direction of $\boldsymbol{k}$ and $\boldsymbol{k'}$ denoted with the angle brackets. The factor $\xi = 1+m\partial^2\varepsilon_p/\partial p^2$ represents the charge carriers spectrum and becomes numerical $\xi = 1$ or $\xi = 2$ for linear and parabolic dispersion, respectively. Note that all equations were defined at $\varepsilon_k = \varepsilon_F$.

Looking at Eq. (59) it can be concluded that under cyclotron resonance condition ($\omega = \omega_c$) the increase in the absorbance $\eta(\omega)$ also results in a resonant enhancement of the photocurrent. This is in agreement with the experimental findings obtained in all HgTe films studied, see Figs. 16-19. The cyclotron masses, obtained in experiments (see Tab. 3), depend on the band structure and are therefore different for top and bottom surface states. These values are in good agreement with previously performed band structure calculations [38] based on the $\boldsymbol{k}\cdot\boldsymbol{p}$ method [116, 117].

Solving Eq. (59) the projections of the generated total photocurrent for two perpendicular in-plane directions can be written as

$$\begin{aligned} j_x &= -eI\eta(\omega)B_z\frac{g_x + \omega_c\tau g_y}{1+\omega_c^2\tau^2}\xi\frac{\langle|q_z|\omega_1\rangle}{\langle|q_z|\omega_0\rangle} \\ j_y &= -eI\eta(\omega)B_z\frac{g_y + \omega_c\tau g_x}{1+\omega_c^2\tau^2}\xi\frac{\langle|q_z|\omega_1\rangle}{\langle|q_z|\omega_0\rangle}. \end{aligned} \tag{60}$$

Furthermore, from these equations it can be concluded that, on the one hand, the magnitude of the photocurrent depends on $|\boldsymbol{g}|$, and on the other hand, its directions are determined by the orientation of $\boldsymbol{g}$ as well as by $\omega_c\tau$. The

direction of $\boldsymbol{g}$ in systems belonging to the C_1 point group, where the non-trivial in-plane point symmetry operation is absent, is not forced to a certain crystallographic axis and therefore may change with temperature, gate voltage, radiation frequency or other conditions, see Ref. [100]. This was also observed in the experiment, see Fig. 20, where the resonant photocurrent may be odd or even in the magnetic field $\boldsymbol{B}$ depending on the experimental conditions. A change of temperature, for example, can change the direction of $\boldsymbol{g}$ so that resonances change from an even to an odd behaviour in magnetic field, as demonstrated in Fig. 20. A similar behaviour of the photocurrent was previously detected also in (013) oriented HgTe films, see Ref. [100].

Concluding, Eq. (60) demonstrates that the current projections in x- and y-directions may change their sign under variation of experimental parameters or the reversal of the magnetic field. This depends on the relative orientation of the vector $\boldsymbol{g}$ to the orientations of the contacts as well as on the magnetic field strength determining $\omega_c\tau$.

5 Edge photocurrents in mono- and bi-layer graphene

As discussed above another example of a massless Dirac fermion system is graphene. Beside the differences to HgTe, e.g. vanishingly small spin-orbit interaction and existance of chiral edge states, the observation of cyclotron-resonance-enhanced photocurrents is expected. However, before dealing with CR, first effects excited at the edges at zero magnetic field are studied in more detail. Therefore, this chapter devotes to THz induced photocurrents flowing at the edges of mono- and bi-layer graphene samples. In the first section, results of edge currents in mono-layer graphene are discussed. The second one presents the experimental results of edge photocurrents observed in bi-layer graphene and provides a detailed discussion of the microscopic model and underlying kinetic theory. The last section deals with resonant edge photocurrents in bi-layer graphene induced by inter-level and CR-involved intra-level transitions between Landau levels. Here a distinction between the quantum mechanical and semi-classical regime will be given. The corresponding results are published in Refs. [31–33].

5.1 Edge photocurrents in mono-layer graphene

Irradiation of the Hall-bar-shaped mono-layer graphene samples with linearly polarized and pulsed THz radiation results in the formation of a photocurrent which was measured between two contacts along the long side of the sample, see Fig. 22(a). Here, the photocurrents, picked up at opposite lying contact pairs, is presented as a function of the radiation intensity I. The corresponding contact labelling can be found in the inset of Fig. 22(b). The photosignal consistently has an opposite sign at the opposite edges indicating that it primary originates from the current flowing along the edges and not from the bulk. Moreover, looking at the behaviour of the detected current with respect to I, it is conspicuous that it shows a linear dependency at low intensities but tends to saturate at higher ones.

The magnitude of the photocurrent can be controlled not only by the radiation intensity but also by the relative orientation of the radiation electric field vector $\boldsymbol{E}$ to the corresponding edge defined by the angle α, see inset in Fig. 22(b). Figure 22(b) shows typical dependencies of the edge photocurrent on α, which can be easily extracted by $J_{\mathrm{edge}} = (J_{\mathrm{AC}} - J_{\mathrm{GE}})/2$. The behaviour of

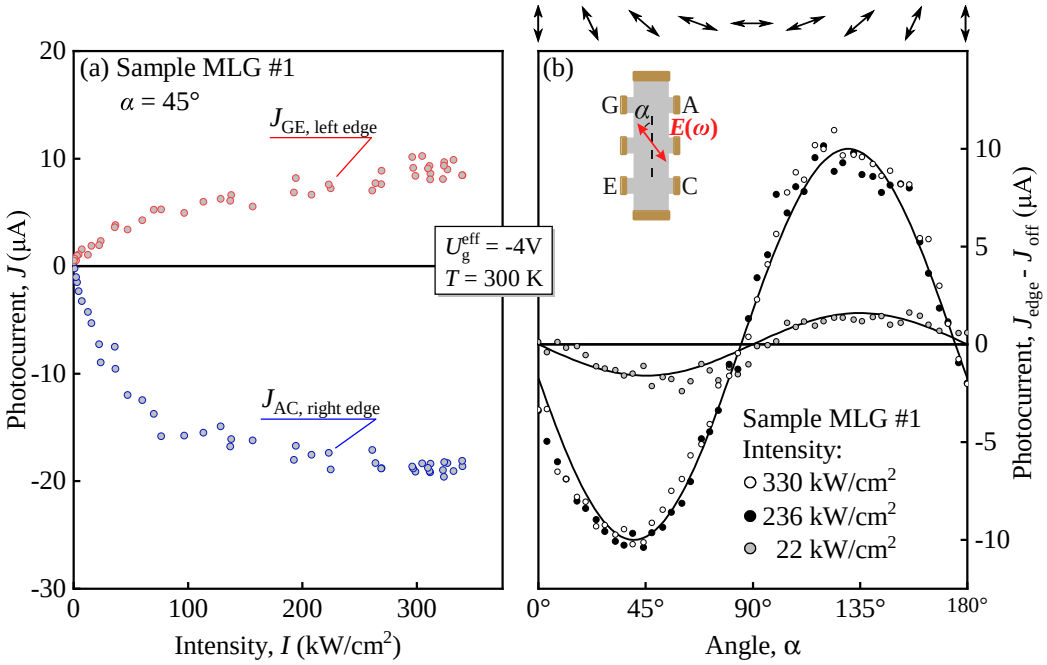

Figure 22: (a) Photocurrents as a function of the radiation intensity obtained at contact pairs along the edge of MLG sample #1. The curves were obtained at an azimuthal angle $\alpha = 45°$ and with a frequency $f = 2.02\,\mathrm{THz}$. (b) Polarization dependence of the edge photocurrent $J_{\mathrm{edge}} = (J_{\mathrm{AC}} - J_{\mathrm{GE}})/2$ at different excitation intensities. Here the fits are curves after Eq. (61). A small polarization-independent offset J_{off} was substracted. The azimuthal angle α as well as the used contacts are illustrated in the inset. Arrows on top show the orientation of the radiation electric field vector $\boldsymbol{E}$ with respect to the samples' long side. Adapted from Ref. [32]

the photoresponse as a function of the azimuthal angle α presented for various radiation intensities can be well fitted by [28]

$$J_{\mathrm{edge}} = J_{\mathrm{L}} \sin(2\alpha + \psi) + J_{\mathrm{off}} \tag{61}$$

with the polarization-dependent and -independent amplitudes J_{L} and J_{off}, respectively. The introduced phase shift ψ is close to zero and the small offset $J_{\mathrm{off}} \ll J_{\mathrm{L}}$ may result from a photothermoelectic effect [118]. At low intensities, the photogalvanic current flowing along the edges and obeying the behaviour described through Eq. (61) was previously observed and discussed in several works [26, 27, 119–121]. At higher intensities, the dependence of the edge photocurrent on the azimuthal angle α is similar. Moreover, by comparing the two highest intensities in Fig. 22(b) a saturation of the photocurrent's

magnitude is clearly visible, which agrees well with the observations in Fig. 22(a). This nonlinearity in the photocurrent can be controlled by the back gate voltage, temperature and radiation frequency and shows for certain gate voltages also a sign alternating behaviour.

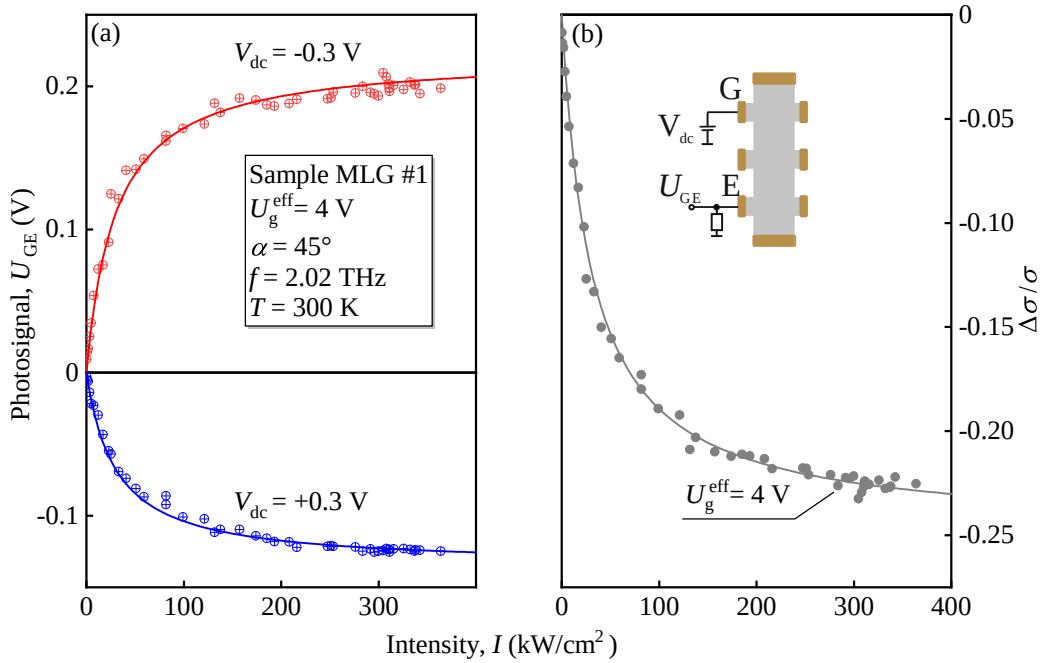

Figure 23: (a) Photosignal measured in the photoconductivity setup as a function of the radiation intensity. The data were obtained with an applied bias voltage of $V_{dc} = \pm 0.3\,V$. (b) Normalized photoconductivity $\Delta\sigma/\sigma$ as a function of the intensity. Solid lines are fits after $\Delta\sigma/\sigma \propto I/(1 + I/I_s)$. The inset shows the used measurement setup. Adapted from Ref. [32]

Furthermore, Fig. 23 presents the change of the sample's conductivity under THz radiation. Here, a dc bias voltage $V_{dc} = 0.3\,V$ was applied to the sample, see corresponding setup in the inset in Fig. 23(b). Applying bias voltages with opposite polarities results in photoresponses having opposite signs, see Fig. 23(a). As introduced in chapter 3.2.2, the photoconductivity signal U_{pc} can be extracted with following equation: $U_{pc} = (U(V_{dc}) - U(-V_{dc}))/2$, which cancels out possible photocurrent contributions. However, Fig. 23(a) shows that the latter are rather small and that the detected signal is dominated by the radiation-induced change of the sample's conductivity, the photoconductivity, shown in Fig. 23(b), where it is normalized to the dark conductivity. Increasing the radiation intensity yields a decrease in the photoconductivity. This behaviour is well known in terms of the μ-photoconductivity mechanism in which an increasing electron gas temperature results in a decrease in carrier

mobility due to scattering on acoustic phonons [29], see Sec. 2.3. These complementary measurements demonstrate that under the prevailing experimental conditions the THz radiation induces a strong electron gas heating. The solid lines in Fig. 23 are fits after $\Delta\sigma/\sigma \propto I/(1 + I/I_s)$ with the saturation intensity I_s. Alike the photocurrent data shown above, the photoconductivity first behaves linearly and then exhibits a saturation behaviour at higher radiation intensities.

A detailed analysis and discussion of the edge photogalvanic currents at high intensities is given in Ref. [32] discussing the complex intensity dependence by the interplay of direct inter-band optical transitions and Drude-like absorption. The subsequent part of this chapter is dedicated to the photogalvanic currents at low intensities which has been studied in numerous papers [26, 27, 80, 119–121]. However, the study of this effect in bi-layer graphene (BLG), in particular of the photocurrent stemming from the edges, has been missing so far. Therefore, the next section will present the observations of the edge electric currents in bi-layer graphene at zero and at small magnetic fields.

5.2 Edge photocurrents in bi-layer graphene

Bi-layer graphene different to mono-layer graphene has a band structure which can be tuned by the application of a gate voltage. At zero gate voltage its dispersion is parabolic and cannot be described by the zero-mass Dirac equation. Nevertheless, the effect of edge photocurrents is also observed in this material and corresponding results are outlined in the following.

5.2.1 Experimental results

Illumination of the bi-layer graphene sample BLG #1 with continuous wave THz radiation results in a photocurrent which was measured as a voltage drop $U_{x,y} \propto J_{x,y}$ over the sample. The photosignal was picked up between a contact pair lying along the edges during illumination of the square-shaped sample with linearly polarized radiation at normal incident. A typical measurement of the photovoltage as a function of the azimuthal angle α is presented in Fig. 24. It demonstrates that the magnitude as well as the sign of the photosignal $U_{x,y} \propto J_{x,y}$ detected for various effective gate voltages U_g^{eff} depend on the relative orientation of the radiation polarization plane and the direction in which they are measured. Figure 24(a) shows the polarization dependencies measured along the edge in x-direction while in panel (b) the photovoltage

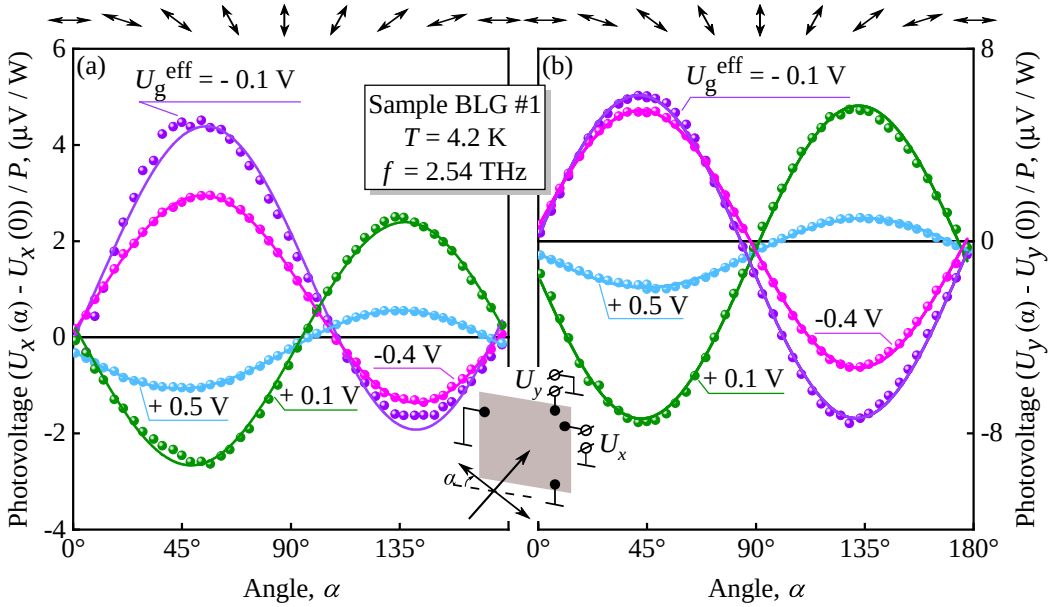

Figure 24: Normalized photovoltage $U_{x,y}/P$ as a function of the azimuthal angle α for various effective gate voltages U_g^{eff}. Data were measured at contact pairs lying along the (a) top, and (b) right edge. The inset illustrates the angle α and the measurement directions. Arrows on top show the relative orientation of the radiation electric field vector $\boldsymbol{E}$ with respect to the sample's edge in x-direction for several angles α. Adapted from Ref. [31]

was measured in y-direction. Similar to the photogalvanic currents in monolayer graphene (see Fig. 22(b)), the data can be well fitted with the following formula

$$U_{x,y} \propto J_{x,y} = J^L_{x,y} \sin(2\alpha + \varphi_0) + J^0_{x,y} \tag{62}$$

with $J^L_{x,y} \propto U^L_{x,y}$ being the polarization-dependent amplitude and ψ the phase shift which is close to zero. A small polarization-independent amplitude $J^0_{x,y}$ was detected in some measurements. A possible reason for this could be the photothermoelectric effect, which was studied previously, e.g. in Ref. [118]. The panels (a) and (b) in Fig. 24, corresponding to the two neighbouring edges, show a similar behaviour and photocurrent sign. At a fixed angle $\alpha = 45°$ the photosignal at both edges is positive for $U_g^{\text{eff}} > 0$ and negative for $U_g^{\text{eff}} < 0$. Considering the angle $\alpha = 135°$ the photocurrent amplitude remains similar but the signal reverses its sign. This indicates that the photocurrents flow either towards or away from the sample's corner.

The dependence of the photocurrent on the effective gate voltage is depicted

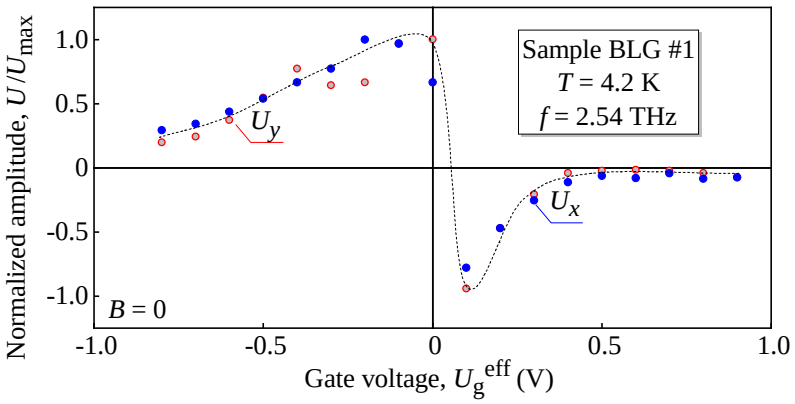

Figure 25: Normalized photovoltage amplitude $U_{x,y}/U_{\max}$ as a function of the effective gate voltage $U_g^{\text{eff}} = U_g - U_g^{\text{CNP}}$. Adapted from Ref. [31]

in Fig. 25. For both, the x- and y-direction, the photocurrent amplitude $U_{x,y} \propto J_{x,y}$ changes its sign upon switching from negative to positive gate voltages, i.e. upon switching the carrier type from holes to electrons.

Moreover, the similar dependence of the photocurrent on the azimuthal angle α (Eq. (62)) measured in the two perpendicular directions, shown in Fig. 24(a) and (b), supports the assumption that the photosignal stems from currents flowing at the edges. Gated bulk bi-layer graphene belonging to the $C_{3\nu}$ point group is non-centrosymmetric, i.e. it lacks a center of space inversion. The trigonal symmetry is the reason why the photocurrents (excited at normal incidence) have orthogonal components which are on the one hand $\propto \cos(2\alpha)$ and on the other hand $\propto \sin(2\alpha)$, i.e. a $\pi/2$ phase shift between the photocurrents in x- and y-direction should be present, for details see Ref. [75]. However, Fig. 24 clearly demonstrates that such a phase shift was not detected, and consequently, the photoresponse can be attributed to carriers residing at the edges of the sample.

Applying a low magnetic field the behaviour of the photocurrent changes upon variation of the azimuthal angle α. Figure 26 shows the polarization dependence of the photovoltage for various magnetic fields. By switching on the magnetic field a phase shift is detected which increases with the field strength. Consequently Eq. (62) changes to $U_{x,y} = U_{x,y}^L(B)\sin(2\alpha + \varphi_0 + \theta_B)$. The inset in Fig. 26 shows the introduced phase θ_B as a function of the magnetic field.

At higher magnetic fields $B \geq 0.5\,\text{T}$ and $U_g^{\text{eff}} > 0$ oscillations periodic in $1/B$ appear in the photoresponse, see Fig. 27. The amplitude of this oscillations is substantially larger than the photovoltage at zero magnetic field and its

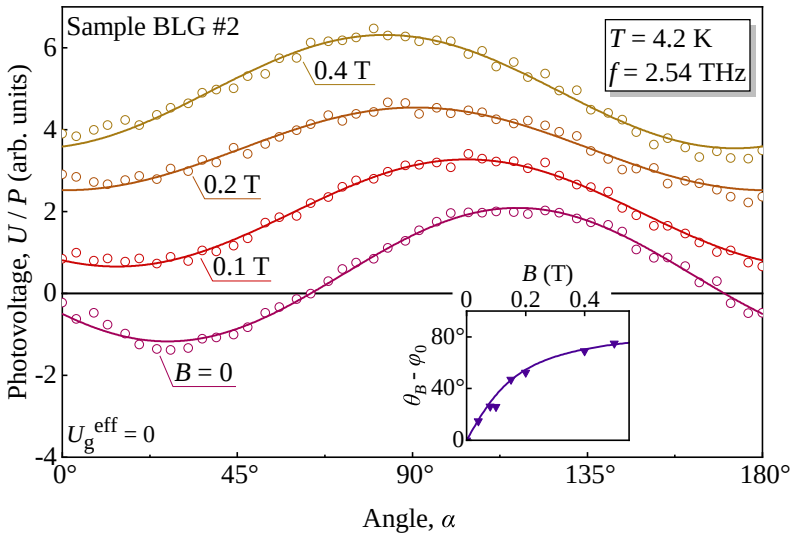

Figure 26: Normalized photovoltage $U/P \propto J/P$ as a function of the azimuthal angle α measured in sample BLG #2 at contact pairs along the edge for various magnetic fields. Solid lines are fits after $U = U^L(B)\sin(2\alpha+\varphi_0+\theta_B)$. The data are vertically shifted for better visibility. The inset shows the phase shift θ_B as a function of the field strength with the solid line calculated after $\theta_B = \arctan(2\omega_c\tau)$ using $\tau = 0.6\,\mathrm{ps}$. Adapted from Ref. [31]

period can be controlled by the gate voltage, see Fig. 27(a)-(c). It is apparent that at the vicinity of the CNP the oscillations are almost absent. Changing the radiation frequency does not influence the period of the oscillations but changes its amplitudes, see Fig. 27(d).

In Fig. 28(a) the photovoltage oscillations are presented together with the first derivative of the magneto resistance $\mathrm{d}R_{xx}/\mathrm{d}B$. The position of the corresponding oscillation maxima B^{-1} are shown in Fig. 28(b). It demonstrates that the oscillations are linked to the detected SdH resistance oscillations since they follow its first derivative. In further measurements with high power pulsed lasers, however, the oscillations in the photovoltage are absent.

5.2.2 Discussion

The experimental findings, presented above, show that the dc edge currents can be controlled by the polarization of the incident THz radiation (Eq. (62)) and the applied gate voltage. Applying classical magnetic fields results in a phase shift in the polarization dependence, while at higher magnetic fields and higher gate voltages $1/B$-periodic oscillations appear which follow the first derivative of the SdH oscillations in the longitudinal resistance. A conversion of an ac THz field into a dc voltage can result from numerous phenomena.

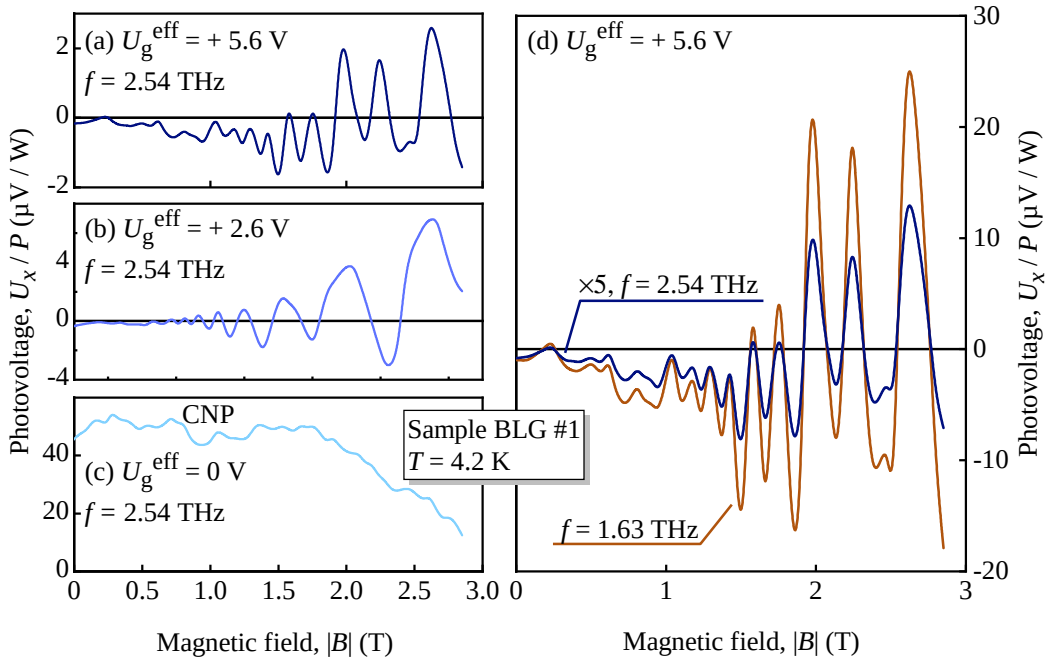

Figure 27: Magnetic field dependencies of the normalized photovoltage U_x/P. Panels (a)-(b) show data for different effective gate voltages U_g^{eff} and panel (d) for two different frequencies at a fixed gate voltage value $U_g^{\text{eff}} = +5.6\,\text{V}$. Note that data for $f = 2.54\,\text{THz}$ were multiplied by a factor 5. Adapted from Ref. [31]

The origin can be for example photogalvanic and photothermoelectric effects or rectification of plasmon-assisted photocurrents [122, 123]. However, in this list only photogalvanics can explain the key properties of the detected edge currents. Importantly, the observed edge currents differ from the photocurrents stemming from edge states in 2D topological insulators [124] because helical edge states are not present in our samples.

As hereinafter provided, the developed microscopic model describes the origin of the observed edge photocurrents in terms of P-symmetry breaking at the edges [80]. Although mono-layer graphene has fundamental differences to bi-layer graphene the description of the photocurrents' cause is quite similar. Therefore, the following model can also be used to describe photocurrents observed in Chap. 5.1 at low intensities. After the discussion of the model a brief introduction of the kinetic theory [27, 31, 80], provided by Dr. M. V. Durnev from Ioffe Institute in St. Petersburg is given, followed by a concluding discussion comparing theory and experimental results.

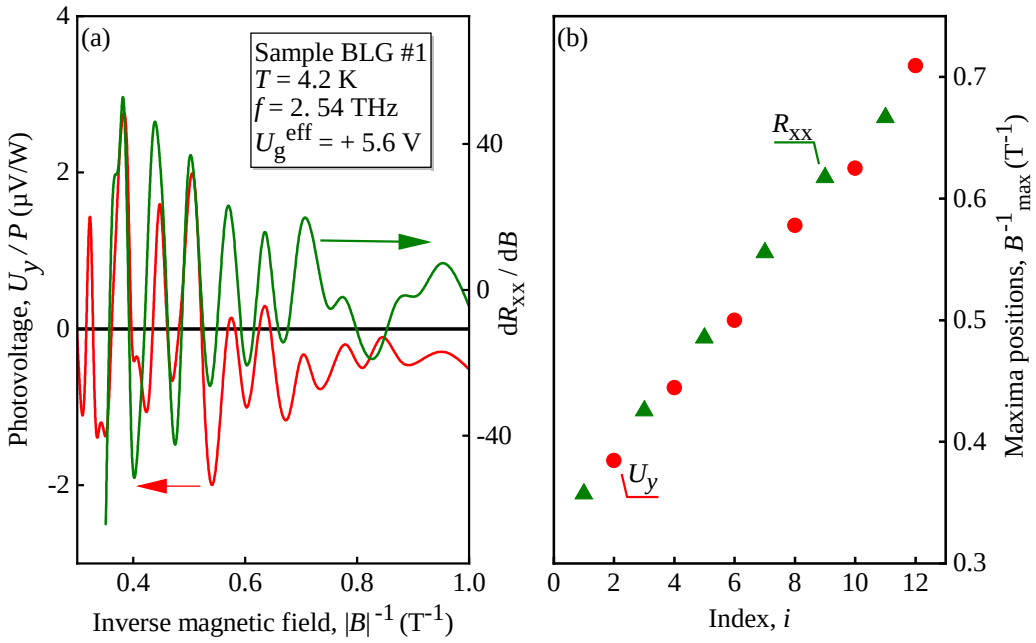

Figure 28: (a) Normalized photovoltage U/P (red curve) together with the first derivative of the longitudinal resistance dR_{xx}/dB (green curve) as a function of the inverse magnetic field. (b) Maxima positions of the photoresponse and resistance against the oscillation numbers. Adapted from Ref. [31]

Microscopic Model The dc edge photocurrent forms as a result of the excitation with the high-frequency electric field of the THz radiation and the broken charge symmetry at the edges. The electric field causes an alignment of the free carrier momenta. A sketch of the photocurrent formation is shown in Fig. 29. After exciting the sample with linearly polarized THz radiation, Drude absorption takes place which results in an alignment of the carrier momenta $\boldsymbol{p}$ and, consequently, its velocities $\boldsymbol{v}$. Subsequently the carriers move predominantly along the orientation of the electric field vector $\boldsymbol{E}$. The herefrom arising distribution is illustrated in Fig. 29(a) for an azimuthal angle $\alpha = 45°$. Note that optical alignment is possible for intraband as well as interband optical transitions. In the case of intraband transitions, considered here, the quasi-momenta are aligned along $\boldsymbol{E}$ [78, 80]. In contrast, in the case of interband transitions they are aligned orthogonally to $\boldsymbol{E}$ [79, 80, 125]. The momentum alignment yields a distribution which is anisotropic and can be described by the second angular harmonic of the distribution function f in $\boldsymbol{p}$-space. The alignment itself does not result in a net electric current but taking into account the symmetry breaking at the edges a photocurrent arises, see Fig. 29(b). In

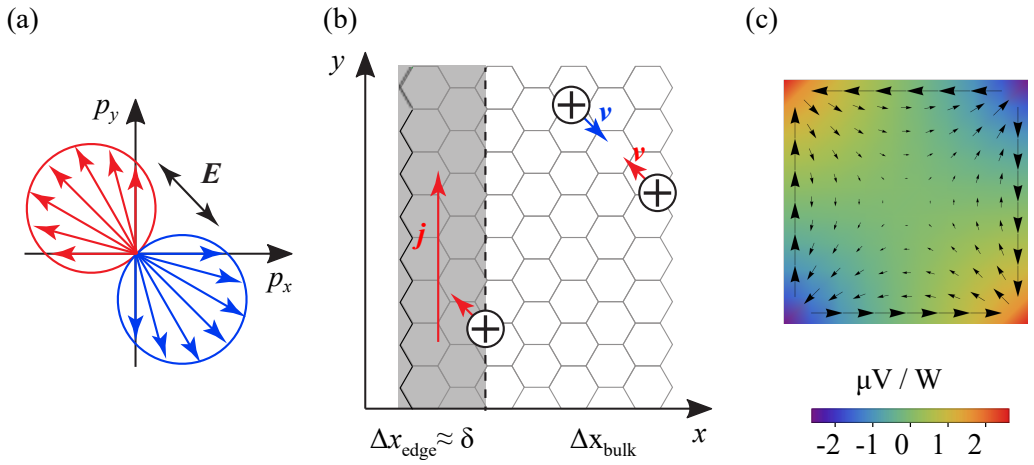

Figure 29: Microscopic model for the edge photocurrent generation illustrated for hole conductivity resulting from Drude absorption of linearly polarized THz radiation with an azimuthal angle $\alpha = 45°$. (a) Distribution of the carrier momenta $\boldsymbol{p}$ where blue and red arrows visualize the induced anisotropy. (b) Carrier fluxes in the vicinity of the sample's edges Δx_{edge} and in the bulk Δx_{bulk} induced by the optical alignment of the carrier momenta. The generated electric current caused by the imbalance of the carrier fluxes at the edges is shown as vertical red arrow. (c) Spatial distribution of the dc photocurrent (arrows) and photoinduced electrostatic potential normalized to the radiation power in a square-shaped sample. Adapted from Ref. [31]

the bulk Δx_{bulk} two carrier fluxes (red and blue arrows) cancel each other and thus no current can be measured[4]. However, the situation changes at the edges. Here two mechanism resulting in a net electric current contribute. The first one is related to imbalances of the carrier fluxes at the edges illustrated in Fig. 29(b). In a stripe of the mean free path width Δx_{edge} the carrier flux coming from bottom right is not compensated by a carrier flux coming from the top left, as is the case for the bulk region. Due to this imbalance a net electric current $\boldsymbol{j}$ flowing along the edges emerges. The second mechanism is based on scattering at the edges and is discussed in more detail in Refs. [27, 28].

Figure 29(b) illustrates the current generation for p-type conductivity. Changing the carrier type does not change the direction of the carrier fluxes at the edge which means that the electric current has the opposite sign. It also demonstrates that the direction and magnitude of the photocurrent can be controlled by the radiation's polarization state. If the electric field vector of

[4]Note that here possible imbalances due to C_{3v} symmetry of the bi-layer graphene are neglected.

the THz field points along or normal to the samples edge, $\alpha = 0°$ or $90°$, the photocurrent vanishes, whereas if it is oriented at $\alpha = 45°$ or $135°$ the current magnitude reaches a maximum. Moreover, it has the opposite sign for these two polarization states. The polarization dependence follows $j_{\text{edge}} \propto \sin(2\alpha)$, which is in good agreement with the experimental findings, see Figs. 22, 24, 26. Note that the small phase shift φ_0 may be caused by photocurrents emerging in the bulk of the bi-layer graphene. The origin of these currents is similar to that observed in TIs based on BiSbTe having the same point group symmetry C_{3v} like gated bi-layer graphene as well as bi-layer graphene on a substrate. Details to this mechanism can be found in chapter 2.3 and in Ref. [75].

Application of a small magnetic field normal to the bi-layer graphene leads to a rotation of the distribution of the electron momenta due to the Lorentz force. This was experimentally observed as a phase shift θ_B in the polarization dependence, see Fig. 26.

All together, the properties of the edge photocurrent observed in experiment, involving the dependence on polarization state of the radiation and on the contributing carrier type, as well as the observed phase shift at classical magnetic fields, can be well explained in terms of the presented microscopic model.

Kinetic theory The microscopic theory explaining the edge photogalvanic effect is based on the Boltzmann kinetic equation [27]

$$\frac{\partial f}{\partial t} + v_x \frac{\partial f}{\partial x} + e\Big(\boldsymbol{\mathcal{E}}(x,t) + \frac{1}{c}\boldsymbol{v} \times \boldsymbol{B}\Big)\frac{\partial f}{\partial \boldsymbol{p}} = \mathrm{St} f. \tag{63}$$

Here, $f(\boldsymbol{p}, x, t)$ is the carrier distribution function, where $\boldsymbol{p}$ and $\boldsymbol{v} = \boldsymbol{p}/m^*$ define the momentum and velocity of the carriers, m^* their effective mass and e their electric charge. $\boldsymbol{B}$ is the magnetic field and $\mathrm{St} f$ the collision integral. The total field $\boldsymbol{\mathcal{E}}(x,t) = \boldsymbol{\mathcal{E}}(x)\exp(-\mathrm{i}\omega t) + \text{c.c.}$ can be divided into the ac electric field of the incoming wave $\boldsymbol{E}\exp(-i\omega t) + \text{c.c.}$ and the local screening field $\delta E_x(x) \propto E$ induced by the dynamical charge accumulation of the electric charge in the vicinity of the edges (see appendix in Ref. [31] for details).

With expansion of the distribution function in a series over the electric field $\boldsymbol{E}$, Eq. (63) can be solved

$$f(\boldsymbol{p}, x, t) = f_0 + [f_1(\boldsymbol{p}, \boldsymbol{x})\exp(-i\omega t) + \text{c.c.}] + f_2(\boldsymbol{p}, \boldsymbol{x}). \tag{64}$$

Here f_0 is the equilibrium distribution function, $f_1 \propto E$ the first-order correction, and $f_2 \propto EE^*$ the time-independent second-order correction describing the dc electric current. The local current density of the dc current $j_y(x)$ can be written as

$$j_y(x) = 4e \sum_{\boldsymbol{p}} v_y f_2(\boldsymbol{p}, \boldsymbol{x}). \tag{65}$$

Here the spin and valley degeneracy is taken into account by the factor 4. The total electric edge current is obtained by

$$J_y = \int_0^\infty j_y(x) \mathrm{d}x. \tag{66}$$

Taking into account boundary conditions $f(p_x, p_y, 0) = f(-p_x, p_y, 0)$ and the relevant experimental conditions $\omega \gg \omega_c$ the photocurrent flowing along the edge is given by [31]

$$\begin{aligned} J_y = & \frac{ne^3\tau^3}{m^{*2}(1+\omega^2\tau^2)} \left[\frac{2\omega_c\tau|\boldsymbol{E}|^2}{1+\omega^2\tau^2} - \frac{i(E_xE_y^* - E_yE_x^*)}{\omega\tau} \right. \\ & \left. - \frac{E_xE_y^* + E_yE_x^*}{1+4\omega_c^2\tau^2} + \frac{2\omega_c\tau(2+\omega^2\tau^2)(|E_x|^2 - |E_y|^2)}{(1+4\omega_c^2\tau^2)(1+\omega^2\tau^2)} \right], \end{aligned} \tag{67}$$

with the cyclotron frequency $\omega_c = eB_z/(m^*c)$ and the momentum relaxation time τ.

Equation (67) shows that the edge photocurrent consists of (i) a polarization independent term $J_y \propto |\boldsymbol{E}|^2$, (ii) a term depending on the circular polarization $J_y \propto S_3 = i(E_xE_y^* - E_yE_x^*)$, and terms which are proportional to the Stokes parameters for linear polarization given by $S_2 = E_xE_y^* + E_yE_x^*$ and $S_1 = |E_x|^2 - |E_y|^2$. If no magnetic field is applied the terms $\propto |\boldsymbol{E}|^2$ and $\propto |E_x|^2 - |E_y|^2$ vanish and the variation of the photocurrent with the polarization is described by $E_xE_y^* + E_yE_x^*$.

If $\omega\tau \gg 1$ the last two terms play the most dominant role in the photocurrent equation. In this particular case the external magnetic field influences only the magnitude of the photocurrent and introduces a phase shift in the polarization dependence given by $\theta_B = \arctan(2\omega_c\tau)$.

Comparison theory and experimental results After the introduction of the kinetic theory based on Boltzmann kinetic equation, a brief discussion follows

in which theory and experimental observations are compared. The developed Eq. (67) describes the photocurrent in the vicinity of the edges for classical magnetic fields. Experimentally relevant conditions are $\omega\tau \gg 1$ and $\omega \gg \omega_c$. The observed polarization dependence measured at contact pairs of neighbouring edges is described by the last two terms of Eq. (67), $J_y \propto (E_x E_y^* + E_y E_y^*)$ and $J_y \propto (|E_x|^2 - |E_y|^2)$. If the magnetic field is absent the edge photocurrent is determined by the Stokes parameters given by $J_y \propto (E_x E_y^* + E_y E_y^*) \propto \sin 2\alpha$ corresponding to Fig. 24, whereas at classical magnetic fields a phase shift appears in the polarization dependence, see Fig. 26. The photocurrent, and consequently, the photovoltage is expressed by $U_y \propto J_y \propto \sin(2\alpha + \theta_B)$ with $\theta_B = \arctan(2\omega_c\tau)$. The calculated phase shift θ_B is compared to the experimental findings in the inset of Fig. 26. It exhibits a good agreement for $m^* = 0.03\, m_0$ and $\tau = 0.6\,\mathrm{ps}$, which are typical values in such samples [126, 127]. Furthermore, the change of the photocurrent sign observed in the experiments (Figs. 24 and 25) is in line with Eq. (67), since $J_y \propto e^3$ implies an opposite current direction for electrons ($e < 0$) and holes ($e > 0$).

Figure 29(c) shows the total dc current spreading in the sample and the spatial distribution of the photocinduced electrostatic potential $\Phi(x, y)$. These were obtained by solving the continuity equation for the total dc current $\nabla \cdot (\boldsymbol{j} + \boldsymbol{j}^{\mathrm{dr}}) = 0$ with $\boldsymbol{j}$ and $\boldsymbol{j}^{\mathrm{dr}}$ being the edge photocurrent and the compensating drift current in the bulk, respectively. The latter one can be written as $j_\alpha^{\mathrm{dr}} = \sum_\beta \sigma_{\alpha\beta}\Delta\Phi$ with the dc conductivity $\sigma_{\alpha\beta}$ at $\omega = 0$. This yields the Poisson equation

$$\frac{\sigma_0}{1 + \omega_c^2\tau_1^2} = \nabla \cdot \boldsymbol{j}, \tag{68}$$

which can be solved numerically using Green's function and taking into account boundary conditions at $x = 0$, where the electric currrent is zero, similar to Ref. [128]. The corresponding solution is shown in Fig. 29(c) for zero magnetic field, $\omega\tau \gg 1$, an azimuthal angle $\alpha = 45°$, an effective mass $m^* = 0.03\, m_0$ and a radiation frequency being $\omega/2\pi = 2.54\,\mathrm{THz}$. The photovoltage magnitude calculated between adjacent edges of the sample is $U/P \approx 4\,\mu\mathrm{V/W}$ and is in good agreement with the experimentally obtained amplitude, see e.g. Fig. 24.

Applying higher magnetic fields Landau levels form which result in an oscillating dependence of the density of states $D(\varepsilon)$ on the Fermi energy. It yields an additional term in the edge photocurrent described by $J_y \propto \mathrm{d}E(\varepsilon)/\mathrm{d}\varepsilon$. This may explain the observed SdH related oscillations at higher magnetic fields and

gate voltages (Figs. 27 and 28). Increasing the temperature results in a suppression of the SdH oscillations, and, consequently of the related photocurrent oscillations. This was also observed experimentally by applying high power pulsed THz radiation, which result in the increased heating of the electron gas. As yet, a microscopic theory of the edge photocurrent in the regime of the SdH oscillations is missing, and therefore, a further discussion of its origin is out of scope of this work.

5.3 Edge photocurrents due to CR and inter Landau level transitions

After the discussion of the edge photocurrents, the following chapter will present results on cyclotron-resonance-induced phenomena in bi-layer graphene. Depending on the gate voltage and on the magnetic field also inter Landau level transitions involving valence and conduction band can be observed.

5.3.1 Experimental results

In this section Hall bar structures prepared from exfoliated bi-layer graphene similar to section 5.2.1 are investigated but in the presence of a strong magnetic field. The photovoltage $U \propto J$ is picked up at contact pairs along the long side of the Hall bar. By irradiating the bi-layer sample with cw THz radiation with frequency $f = 2.54\,\mathrm{THz}$, three resonances in the magnetic field dependence of the photovoltage appear, see Fig. 30(a).

The pronounced resonances, labelled CR1, CR2, and CR3 were detected at contacts A and B, see inset in Fig. 30(a). Their positions remain unchanged during the variation of the azimuthal α; however, the amplitude changes slightly. Strikingly, measuring at the opposite edge (contacts C and D) the photosignal has consistantly the opposite sign, see Fig. 30(b) and inset in panel (a) for the measurement setup. In the used electric setup the signal picked up at contacts AB is negative whilst the one picked up at CD is positive indicating that the photocurrents along opposite edges flow in opposite directions. This observation allows the conclusion that the photocurrents are generated at the edges and not in the bulk since in the latter U_{AB} and U_{CD} should have equal directions. This conclusion together with the fact that the amplitudes have almost the same magnitude indicates that the photocurrents flow along the sample's edges. To extract the edge contribution

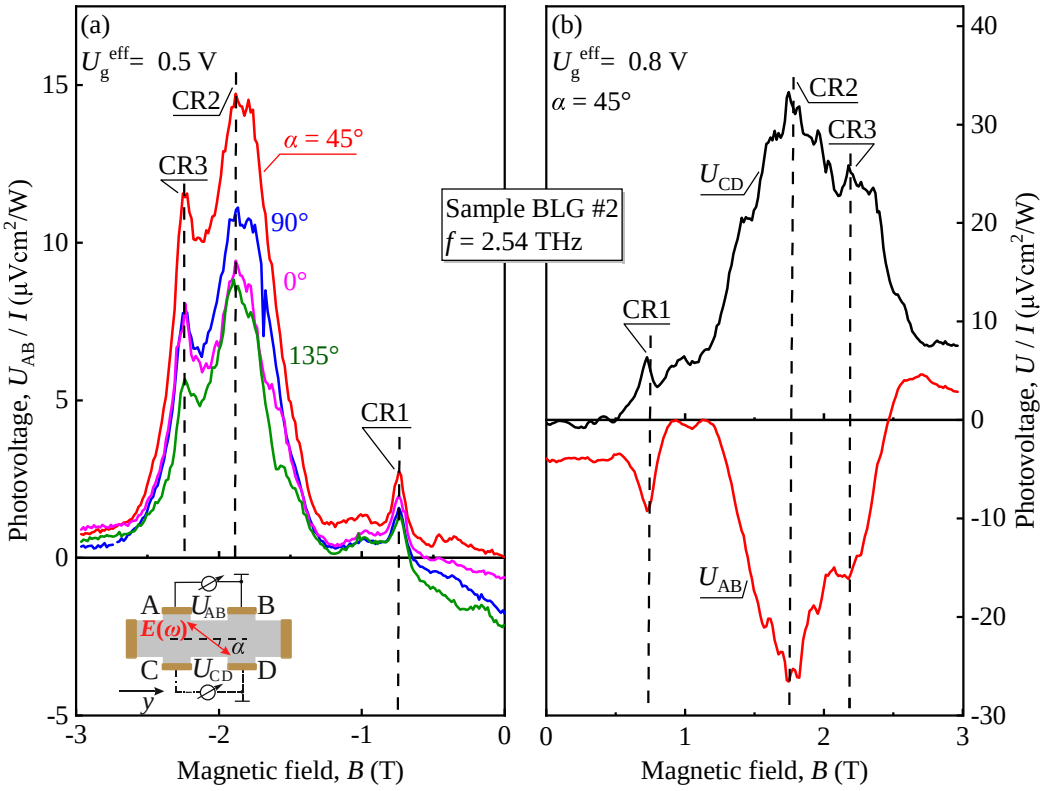

Figure 30: (a) Normalized photovoltage U_{AB}/I as a function of the magnetic field obtained for different azimuthal angles α. Inset shows the experimental setup with contact names and an illustration of the angle α. (b) U_{AB} and U_{CD} picked up from contact pairs at opposing edges. The normally incident radiation has an intensity of $I = 2\,\mathrm{W/cm^2}$. Adapted from Ref. [33]

$U_{edge} \propto J_{edge}$ from the measured photosignals, U_{AB} and U_{CD} are subtracted after $U_{edge} = (U_{CD} - U_{AB})/2$.

Figure 31(a) presents a magnetic field dependency of the normalized edge photosignal U_{edge}/U_{edge}^{max}. It shows that the resonances, indicated by CR1,CR2 and CR3, have opposite signs for opposite field polarities. Furthermore, by changing the applied back gate voltage, i.e. the Fermi level position, the traces of CR1 and CR3 get weaker wherease CR2 is still very pronounced, see Fig. 31(b). However, the positions of the three resonances stay almost the same for small gate voltage ranges. Going to even higher voltages results in a full disappearance of CR1 and CR3, see Figs. 33 and 35(a). To investigate the origin of these resonant traces further measurements at different radiation frequencies were performed, see Fig. 31(c). It demonstrates that by changing the frequency from $f = 2.54$ to $0.69\,\mathrm{THz}$ a shift of CR2 and CR1 by an factor 3.7 can be observed, which indicates that the resonance positions depend

linearly on the radiation frequency. The third resonance CR3 was not detected at the lower frequency. These properties, shown in Fig. 31, are typical for cyclotron resonance; however, a discussion on whether these traces stem from CR-involving transitions is provided in Sec. 5.3.2.

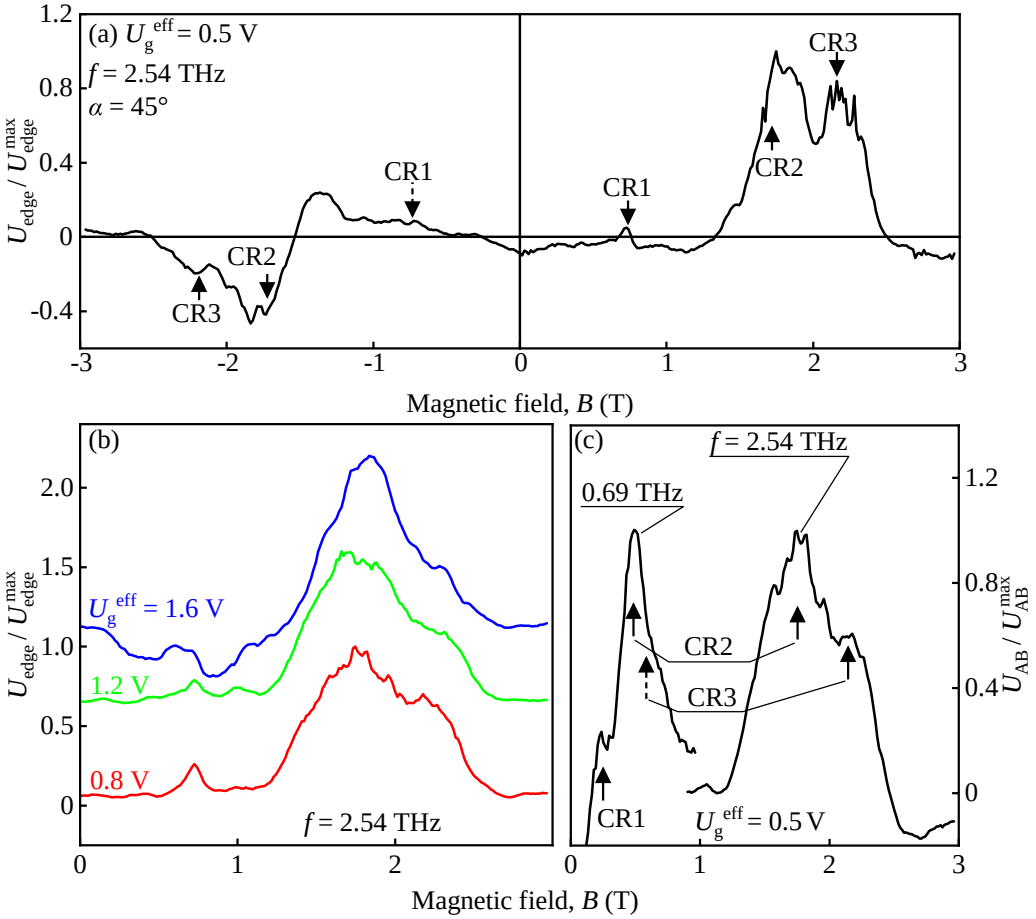

Figure 31: Edge contribution of the photosignal $U_{edge} = (U_{CD} - U_{AB})/2$ normalized to its maximum value U_{edge}^{max} as a function of the magnetic field obtained in sample BLG #2. Panel (a) was measured for both B-field polarities. CR1, CR2, and CR3 indicate the resonance positions. Data in panel (b) were measured for different effective gate voltages U_g^{eff}. Curves are vertically shifted by 0.2 for better visibility. (c) Photosignal U_{AB}/U_{AB}^{max} at two different frequencies $f = 2.54$ and 0.69 THz. Adapted from Ref. [33]

Moreover, the photocurrent amplitudes at resonance position can be controlled by the relative orientation of the electric field to the edges defined by the angle α, see Fig. 32. Here the polarization dependence of the photovoltage U_{AB}/I was measured at resonance positions B_{CR2} and B_{CR3}. The data can be

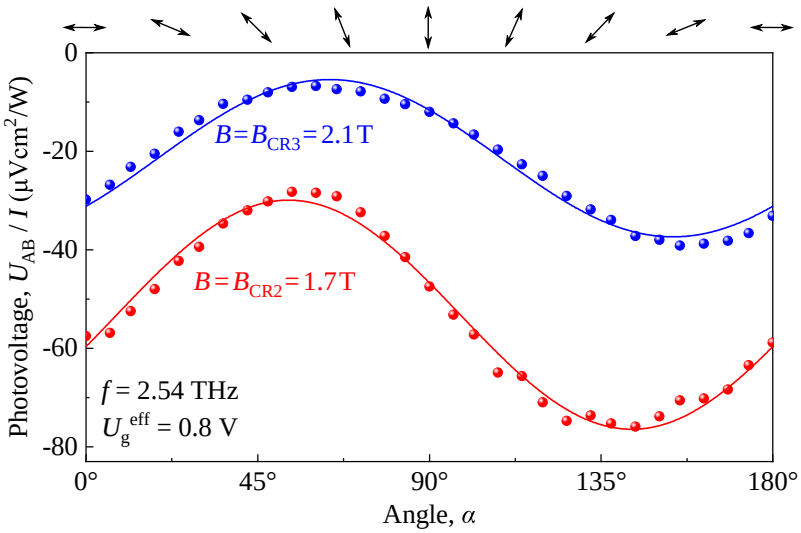

Figure 32: Normalized photovoltage U_{AB}/I as a function of the azimuthal angle α obtained at fixed magnetic fields $B_{\mathrm{CR2}} = 1.7\,\mathrm{T}$ and $B_{\mathrm{CR3}} = 2.1\,\mathrm{T}$ in sample BLG #2. Full lines are fits after Eq. (69) and arrows on top illustrate the relative orientation of the electric field vector $\boldsymbol{E}$ to the long side of the Hall bar for different values of α, see inset of Fig. 30. Adapted from Ref. [33]

well fitted by

$$U \propto J = J_{\mathrm{L}} \sin(2\alpha + \psi) + J_0 \tag{69}$$

with the polarization-dependent and -independent amplitudes, J_{L} and J_0, respectively as well as the phase shift ψ being almost zero at the resonance positions. Figure 32 also demonstrates that on the one hand the magnitude of the photocurrent varies with the azimuthal angle α and on the other hand the direction of the current remains unchanged.

So far, the data discussed were measured at low back gate voltages (below 1.6 V), corresponding to carrier densities below $0.7 \times 10^{11}\,\mathrm{cm}^{-2}$. The situation changes for higher carrier densities as shown in Fig. 33. At a certain back gate voltage SdH-related oscillations superimpose the resonances and make the analysis of their positions more complex. These $1/B$-periodic photocurrent oscillations are already observed in the sample BLG #1 and discussed in Sec. 5.2.1. Their periods reveal the carrier densities of the sample providing an excellent agreement with the ones obtained in the magnetotransport measurements. However, a strong enhancement of the oscillations at certain magnetic fields can be found with a position varying for the different carrier densities

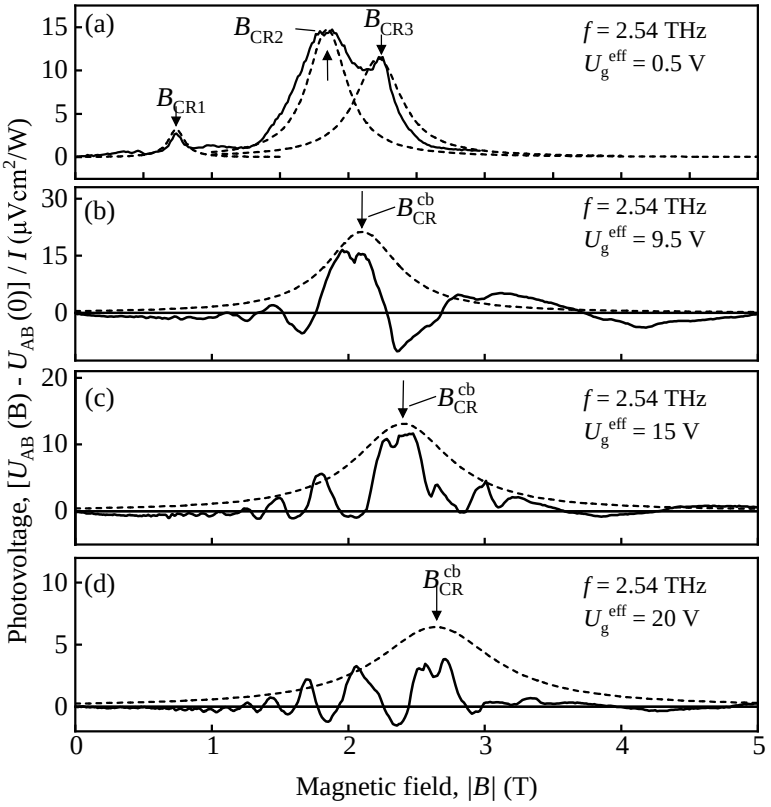

Figure 33: Photovoltage $[U_{\mathrm{AB}}(B) - U_{\mathrm{AB}}(0)]$ as a function of the magnetic field for various gate voltages $U_{\mathrm{g}}^{\mathrm{eff}}$ obtained in sample BLG #2. From (a) $U_{\mathrm{g}}^{\mathrm{eff}} = 0.5\,\mathrm{V}$ to (d) $U_{\mathrm{g}}^{\mathrm{eff}} = 20\,\mathrm{V}$. Dashed lines are fits after Eq. (4). The resonance positions B_{CR1} (LL transitions $(2-) \rightarrow (3+)$ and $(3-) \rightarrow (2+)$) and B_{CR3} ($(2-) \rightarrow (1)$) used for fits are calculated after Eqs. (71). For the calculations of B_{CR2} and $B_{\mathrm{CR}}^{\mathrm{cb}}$ values Eq. (72) was used. Here, following LL transitions are considered: $(1) \rightarrow (2+)$ (a), $(2+) \rightarrow (3+)$ (b), $(4+) \rightarrow (5+)$ (c), and $(5+) \rightarrow (6+)$ (d). The calculated resonance positions are indicated by vertical arrows. The transport width used for calculations was $1/\tau = 1.4\,\mathrm{ps}$ and the superradiant decay rates Γ' are given in Tab. 4. Adapted from Ref. [33]

between $B = 1.8$ and $2.6\,\mathrm{T}$. As will be discussed in further details below, it is assumed that a single resonance caused by intraband optical transitions is responsible for this enhancement.

5.3.2 Discussion

The above presented experimental findings show a photocurrent flowing along the samples edges which exhibits three resonances CR1, CR2, and CR3 in the magnetic field dependency. The position of the resonances depend linearly on the radiation frequency, while their magnitude can be controlled by the

radiation's polarization state. At small carrier densities the resonance positions are resistant against variations of the back gate voltage. At carrier densities larger than $n = 0.7 \cdot 10^{11}\,\mathrm{cm}^{-2}$ it seems that the position of CR2 shifts to higher magnetic fields, while CR1 and CR3 vanish. The precise determination of the peak position is, however, difficult due to $1/B$-periodic oscillations which superimpose the resonances.

In the following an analysis of the positions and shape of the resonances is given, including the identification of CR-induced transitions and comparison of the developed semi-classical theoretical description based on Boltzmann kinetic equation with the experimental results.

Identification of optical transitions To find possible optical transitions which induce the resonantly enhanced edge photocurrents the energy dispersion of bilayer graphene was calculated by Dr. S. Slizovskiy from Manchester University. The calculations are based on the Slonczewski–Weiss–McClure tight-binding model, for review see e.g. [129–131]. From a four-band tight-binding model the Landau level spectrum was found numerically, see Fig. 34, with following parameters: hopping parameters $\gamma_0 = 3.16\,\mathrm{eV}$, $\gamma_1 = 0.35\,\mathrm{eV}$, $\gamma_3 = 0.3\,\mathrm{eV}$, $\gamma_4 = 0.14\,\mathrm{eV}$, and the sublattice energy difference $\Delta_{A_iB_i} = 0.05\,\mathrm{eV}$. The top-bottom asymmetry parameter Δ induced by a gate-dependent vertical electric displacement field defines the energy gap emerging between valence and conduction band. Within the Hartree approximation it is given by [16, 61, 132]

$$\Delta = \frac{4\pi e^2 c_0}{\epsilon}\left[n_2 - \frac{\epsilon+1}{4}(n_1 - n_2)\right] \tag{70}$$

with the interlayer separation $c_0 = 0.335\,\mathrm{nm}$, the permittivity of graphene $\epsilon \approx 2.7$, and the electron densities $n_{1,2}$ ($n = n_1 + n_2$) of the two graphene sheets which can be found from the wave functions of the occupied Landau levels (LLs).

To obtain an analytical equation of the LL spectrum the four band model was reduced to an effective two-band model where the trigonal warping term was neglected. This yields exemplary for the $\boldsymbol{K}^+$ valley

$$E_{\pm l} = \frac{2l-1}{l_B^2}\hbar^2 V_4 \pm \frac{\sqrt{l(l-1) + m^2(V_4 + l_B^2\Delta/(2\hbar^2))^2}}{\hbar^{-2} l_B^2 m} \tag{71}$$

with the LL label l, where positive and negative values correspond to con-

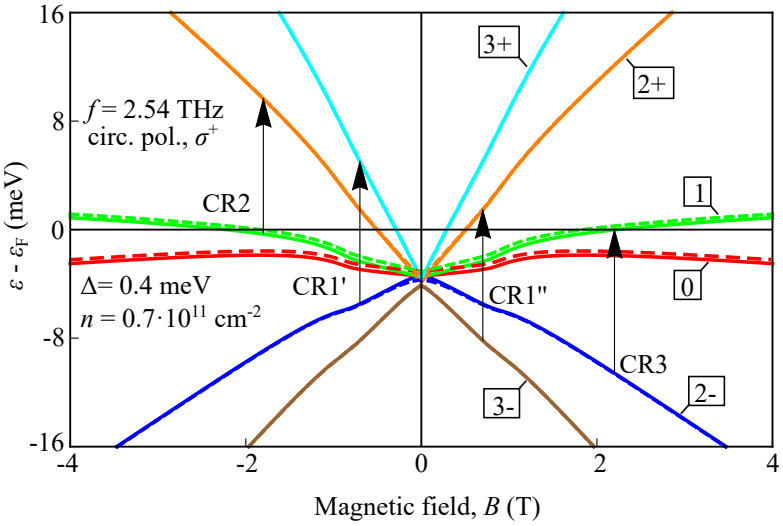

Figure 34: Calculated Landau-level spectra for a gate-induced doping of $n = 0.7 \times 10^{11}\,\mathrm{cm}^{-2}$ with $\Delta = 0.4\,\mathrm{meV}$. The levels are labelled according to Eq. (71). Solid and dashed lines correspond to $\boldsymbol{K}^+$ and $\boldsymbol{K}^-$ valleys, respectively. The allowed optical transitions are illustrated by vertical arrows and are shown for right-handed circular polarization (σ^+) with a frequency $f = 2.54\,\mathrm{THz}$. The transitions are labelled corresponding to the experimentally detected resonances CR1', CR1", CR2 and CR3. Note that the transitions CR1' and CR1" have positions very close to each other and can not be resolved as two resonances in the photovoltage and are therefore labelled as CR1. For linearly polarized radiation the transitions appear at both magnetic field polarities. Adapted from Ref. [33].

duction and valence band, respectively. The magnetic length is given by $l_B = \sqrt{\hbar c/eB}$ and V_4 accounts for the electron-hole asymmetry of the spectrum. To obtain the LL spectra for the $\boldsymbol{K}^-$ valley, Δ has to be replaced by $-\Delta$.

Considering the selection rules presented in Ref. [133], possible optical transitions between the LLs can be found. Assuming circular polarization and $\boldsymbol{B}$ being parallel to the direction of the light angular momentum ($\boldsymbol{B} > 0$) the allowed transitions are

$$(2-) \to (1), (3-) \to (2\pm), (4-) \to (3\pm)...$$

whereas for the case $\boldsymbol{B}$ being antiparallel to the direction of the light angular momentum ($\boldsymbol{B} < 0$) they are

$$...(3\mp) \to (4+), (2\mp) \to (3+), (1) \to (2+)... \,.$$

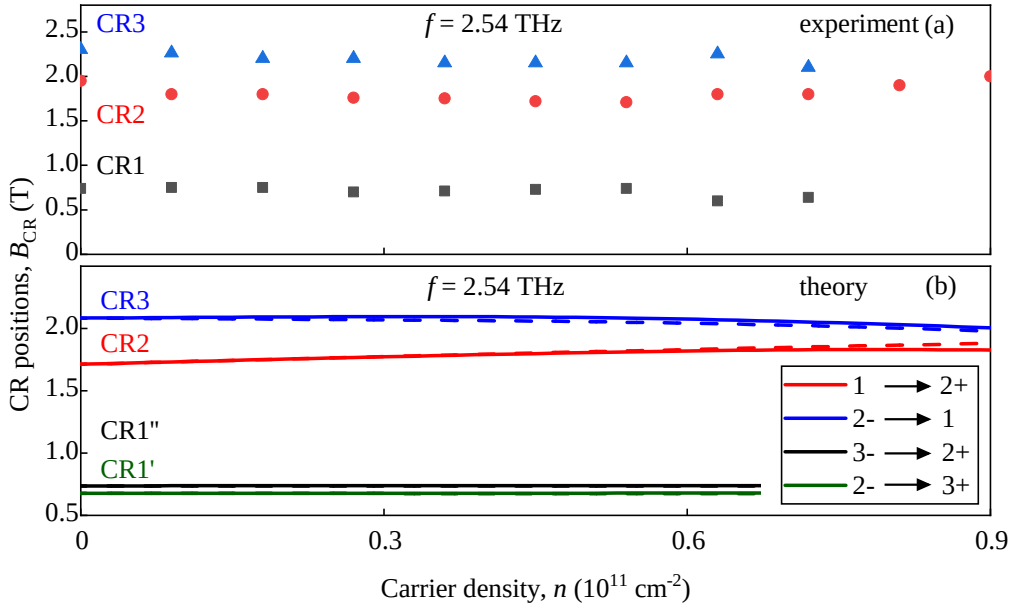

Figure 35: (a) Dependencies of the experimentally obtained resonance positions B_{CR1}, B_{CR2}, and B_{CR3} on the charge carrier density. (b) Resonance positions calculated from possible transitions between Landau levels by taking into account optical selection rules. Solid and dashed lines correspond to $\boldsymbol{K}^+$ and $\boldsymbol{K}^-$ valley, respectively. The plot legend assigns the optical transitions. Adapted from Ref. [33]

The valley splitting of the transitions is negligible except for the transitions $(1) \rightarrow (2+)$ and $(2-) \rightarrow (1)$ when $\Delta \neq 0$, here a small energy-splitting is present. Classical CR transitions appear for holes at $(l-) \rightarrow ((l-1)-)$ for $l \gg 1$ while the other transitions are quantum interband transitions. It should be noted here, that the transitions from or to level (0) are not possible in case of a small asymmetry parameter Δ, see Ref. [133]. Additionally, one has to take into account that for transitions the initial (final) states have to be at least partially filled (empty). Considering this requirement together with the selection rules four possible resonances CR1', CR1", CR2, and CR3 for low electron densities and frequency $f = 2.54\,\mathrm{THz}$ can be found, indicated by vertical arrows in Fig. 34.

The theoretical positions as a function of the carrier density are presented in Fig. 35 together with the experimentally obtained ones. Comparison of the calculated and the experimental values as well as their behaviour with variation of the back gate voltage reveal a very good agreement. In Fig. 34 the resonances are shown for an excitation with circular polarized radiation. Using linearly polarized radiation, as it was done in the experiment, the resonances

at positive (negative) magnetic fields also appear for negative (positive) fields. The transitions CR1' and CR1" appear at B-field positions very close to each other which makes it almost impossible to resolve them as two separate resonances in the photovoltage measurement. Therefore, they are treated as one resonance CR1. The greater mass of holes resulting from electron-asymmetry in the spectrum is the reason why the resonance positions of CR2 and CR3 are slightly different. Going to higher carrier densities results in a full occupation of the final states involved in transitions CR3, CR1', and CR1", and therefore, these resonances vanish. Indeed, the corresponding photocurrent traces become weaker in Fig. 31(b) and vanish in Fig. 33. Furthermore, the decrease in frequency also involves an occupation of the final state ($l = 1$) responsible for the transition CR3. This was also experimentally observed, see Fig. 31(c).

In the semi-classical regime, i.e. at higher densities ($l \gg 1$), the LL spectrum is given by

$$E_{l+1} - E_l \approx \frac{2\hbar^2 V_4}{l_B^2}\mathrm{sign}(l) + \frac{\hbar^2}{l_B^2 m\sqrt{1 + m^2(V_4 + l_B^2\Delta/(2\hbar^2))^2/l^2}}. \qquad (72)$$

This equation was used to calculate the resonant magnetic field, whereas at a low carrier density Eq. (71) was used. The obtained values are parameters necessary to fit the data in Fig. 33. At high carrier densities, in contrast to the low density regime, the resonance position B_{CR} shifts to higher fields with increasing gate-induced doping, which results from the almost linear growth of Δ with the carrier density and, consequently, a reduction of the LL separation.

The resonantly enhanced photocurrents can be well described by the semi-classical shape of cyclotron resonance in the absorbance which is given as

$$\eta \propto \sum_{\pm} \frac{1}{(\Gamma' + 1/\tau)^2 + (\omega \pm \omega_c)^2} \qquad (73)$$

with $1/\tau$ characterized by the momentum relaxation time and the radiative decay parameter $\Gamma' = 2\pi e^2 n/(c m_{\mathrm{CR}})$ [96–99, 134] determined by the charge carrier density n and the cyclotron mass m_{CR} (see also chapter 4). Equation (73) was used to fit the data in Fig. 33 shown by dashed lines. Corresponding B_{CR} values for low carrier densities were obtained from Eq. (71) describing transitions between the lowest LL, including fields for interband (B_{CR1} and B_{CR3}) and intraband transitions (B_{CR2}) , see Fig. 72(a). For higher densities

Eq. (72) holds, describing CR-induced intraband transitions between neighbouring LL within the conduction band. These transitions are labelled with $B_{\mathrm{CR}}^{\mathrm{cb}}$, see Figs. 72(b)-(d). The calculated radiative decay parameter Γ' used for the fits in Fig. 33 and associated cyclotron masses m_{CR}/m_0 obtained from the peak positions B_{CR} are presented in Tab. 4. Overall, the calculated fit curves reveal a good agreement with the experimental data.

$U_{\mathrm{g}}^{\mathrm{eff}}$ (V)	$n\,(10^{11}\,\mathrm{cm}^{-2})$	$B_{\mathrm{CR}}(T)$	m_{CR}/m_0	$\Gamma'\,(\mathrm{ps})^{-1}$
0.5	0.23	$B_{\mathrm{CR2}} = 1.8$	0.020	0.06
9.5	4.37	$B_{\mathrm{CR}}^{\mathrm{cb}} = 2.1$	0.023	1.00
15	6.90	$B_{\mathrm{CR}}^{\mathrm{cb}} = 2.4$	0.026	1.40
29	9.20	$B_{\mathrm{CR}}^{\mathrm{cb}} = 2.7$	0.029	1.70

Table 4: Magnetic field positions of the resonances B_{CR2} and $B_{\mathrm{CR}}^{\mathrm{cb}}$ with corresponding cyclotron masses m_{CR}/m_0 and radiative decay parameter Γ'. The values correspond to the fits in Fig. 33 together with the transport width $1/\tau = 1.4\,\mathrm{ps}^{-1}$.

Strikingly, at low carrier densities (Fig. 33(a)) the calculated fitting curve corresponding to the radiative decay parameter $\Gamma' = 0.06\,\mathrm{ps}^{-1}$ exhibits a smaller CR halfwidth as experimentally detected for that gate voltage $U_{\mathrm{g}}^{\mathrm{eff}} = 0.5\,\mathrm{V}$. In this case, the momentum relaxation rate of the electrons in the edge channel $(1/\tau)$ determines the width of the resonance. The used value of $\tau \approx 0.7\,\mathrm{ps}$ corresponds well to the relaxation times reported in Ref. [127] but is half as much as estimated for the samples studied in this work with mobilities being approximately $\mu \approx 1.5 \times 10^5\,\mathrm{cm}^2/\mathrm{Vs}$ and a cyclotron mass of $m_{\mathrm{CR}} = 0.02\,m_0$, see Table 4. This differences in the relaxation times obtained by means of transport and photocurrent measurements at the edge may result from the fact that the relaxation times in the vicinity of the edges are shorter than the ones in the bulk of the sample.

At higher carrier densities the situation changes. In this regime Γ' increases and exceeds the relaxation rate τ^{-1}. Therefore, the halfwidth of the resonances is determined by the radiative decay parameter (see Table 4) and an extraction of the momentum relaxation time from the CR width is not possible.

Concluding, while at higher electron densities a good agreement between the semi-classical calculations and experimental observations is found, at lower densities, this approach becomes less reliable. Here contributions from elec-

trodynamic effects (Γ') are negligible; however, Landau quantisation effects should be taken into account [135]. Furthermore, the observed resonances can be attributed to interband transitions (B_{CR1} and B_{CR3}) as well as CR-involving intraband transitions (B_{CR2} and $B_{\mathrm{CR}}^{\mathrm{cb}}$).

Microscopic Description The formation of the edge current induced by THz radiation is well described in terms of the microscopic description explained in chapter 5.2.2 which was developed in collaboration with Dr. M. V. Durnev and is based on Boltzmann kinetic equation valid for frequencies $\omega \ll \varepsilon_{\mathrm{F}}/\hbar$. Within this approach the edge photocurrent is given by

$$\begin{aligned} J_y = &\frac{e\tau^2\sigma_0}{m} \\ &\times [\mathcal{A}|\boldsymbol{E}|^2 + i\mathcal{B}(E_xE_y^* - E_yE_x^*) + \mathcal{C}(E_xE_y^* + E_yE_x^*) + \mathcal{D}(|E_x|^2 - |E_y|^2)] \end{aligned} \tag{74}$$

with

$$\begin{aligned} \mathcal{A} &= \frac{2\omega_c\tau}{1 + 2(\omega^2 + \omega_c^2)\tau^2 + (\omega^2 - \omega_c^2)^2\tau^4}, \\ \mathcal{B} &= \frac{1 + (\omega^2 + \omega_c^2)\tau^2}{\omega\tau[1 + 2(\omega^2 + \omega_c^2)\tau^2 + (\omega^2 - \omega_c^2)^2\tau^4]}, \\ \mathcal{C} &= -\frac{1 + (\omega^2 - 5\omega_c^2)\tau^2}{(1 + 4\omega_c^2\tau^2)[1 + 2(\omega^2 + \omega_c^2)\tau^2 + (\omega^2 - \omega_c^2)^2\tau^4]}, \\ \mathcal{D} &= \frac{2\omega_c\tau[2 + (\omega^2 - \omega_c^2)\tau^2]}{(1 + 4\omega_c^2\tau^2)[1 + 2(\omega^2 + \omega_c^2)\tau^2 + (\omega^2 - \omega_c^2)^2\tau^4]}. \end{aligned} \tag{75}$$

Here, σ_0 is the conductivity of the 2DEG without magnetic field and ω_c is the cyclotron frequency. Equation (74) demonstrates that in the presence of a magnetic field the edge photocurrent consists of nonzero terms $\propto E_xE_y^* + E_yE_x^*$ or $|E_x|^2 - |E_y|^2$ describing linear polarized radiation and a term $\propto i(E_xE_y^* - E_yE_x^*)$ which is the Stokes parameter for circular polarized radiation as well as a polarization independent term $\propto |\boldsymbol{E}|^2$. Following, the total current induced by linearly polarized radiation near the CR, under the condition ($|\omega - |\omega_c|| \ll |\omega_c|$), flowing along the edges, can be found

$$J_y^{\mathrm{lin}} = \frac{\mathrm{sign}(B_z)c\tau\eta I}{2B_{\mathrm{CR}}} \times \left[1 + \frac{\sqrt{1 + (\omega - |\omega_c|^2)\tau^2}}{2|\omega_c|\tau}\sin(2\alpha + \theta_B)\right] \tag{76}$$

for the condition $|\omega_c|\tau \gg 1$. In this case cyclotron resonance appears for both magnetic field polarities at positions $B_{\mathrm{CR}} = m_{\mathrm{CR}}\omega_C/|e|$. The azimuthal angle

α describes the relative orientation of the electric field vector with respect to the edges, see e.g. inset in Fig. 30(a). The absorbance η in the vicinity of the CR is given by

$$\eta = \frac{2\pi\sigma_0}{n_\omega c}\frac{1}{1+(\omega-|\omega_c|)^2\tau^2} \tag{77}$$

for regions far from the edge and nonpolarized radiation. The intensity of the incoming wave is given by $I = cn_\omega|\boldsymbol{E}|^2/(2\pi)$ with the refractive index of the dielectric medium n_ω in which the bi-layer graphene is located. The magnetic-field-induced phase shift is given by

$$\tan\theta_B = \frac{1+|\omega_c|(\omega-|\omega_c|)\tau^2}{\omega_c\tau}. \tag{78}$$

Equations (76) and (77) demonstrate that for CR condition the edge photocurrent is proportional to the absorbed energy. This yields an increase in the electric current resulting from the increased absorbance η. Not only the magnitude but also the sign and the polarization dependence are determined by Eq. (76). This description is in accordance with the experimental findings, shown in Figs. 30, 31, and 32. In particular, the sign of the dc edge current can be controlled by the magnetic field polarity which is in agreement with the experimental observations presented in Figs. 30 and 31. Strikingly, the direction of the photocurrent remains when changing from electron transport to hole transport. This behaviour was also reported for edge currents in monolayer graphene subjected to a strong magnetic field in the quantum Hall regime [28].

Equation (76) consists of a polarization-independent and a polarization-dependent contribution. The second term $\propto \sin(2\alpha+\theta_B)$ is sensitive to the orientation of the electric field vector, and, therefore, determines the polarization dependence of the photocurrent. The introduced phase shift θ_B (Eq. (78)) vanishes if $\omega = \omega_c$ which yields a polarization dependence of the linear photocurrent J_y^{lin} being $\propto \sin(2\alpha)$. Indeed, this behaviour was experimentally observed, see Fig. 32, showing a dependency of the photosignal on the angle α well fitted by an equation $\propto \sin(2\alpha)$. In the case $|\omega-|\omega_c||\tau \gg 1$, i.e. away from the CR condition, the phase shift $\theta_B = \pi/2$ yields a polarization dependence $\propto \cos(2\alpha)$.

The dc edge current induced by circularly polarized radiation is determined by the two contributions $\propto |\boldsymbol{E}|^2$ and $\propto i(E_xE_y^* - E_yE_x^*)$ in Eq. (74).

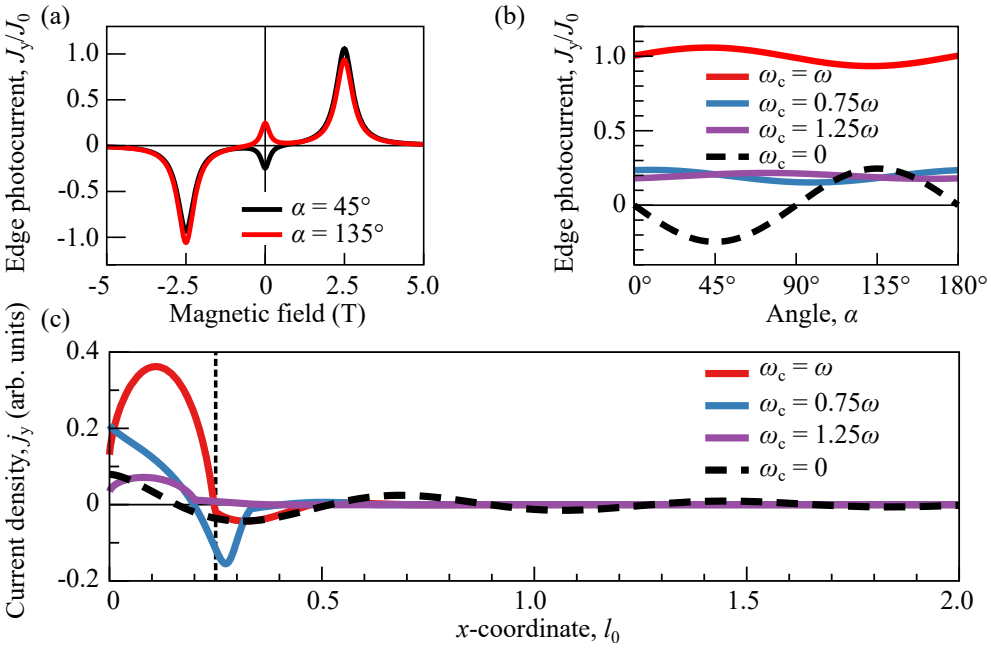

Figure 36: (a) Magnetic field dependence of the edge electric current calculated after Eqs. (74) and (75) for linear polarized radiation with $\alpha = 45°$ and 135°. Sharp CR features appear at $B_{\rm CR} = \pm 2.4\,\mathrm{T}$. (b) Polarization dependence of the edge photocurrent for various magnetic fields. At $\omega_c = 0$, at CR $\omega_c = \omega$ as well as away from the CR condition, $\omega_c = 0.75\omega$ and $\omega_c = 1.25\omega$. (c) Edge current density $j_y(x)$ calculated for circularly polarized radiation. The dashed vertical line illustrates the cyclotron orbit $l_c = 2l_0/(\omega_c\tau)$ at CR. The parameters used for calculations are: $\omega/2\pi = 2.54\,\mathrm{THz}$, $\tau = 0.7\,\mathrm{ps}$, $B_{\rm CR} = 2.4\,\mathrm{T}$, and $\omega\tau = 11$. Adapted from Ref. [33]

Cyclotron resonance appears for a certain polarity of the magnetic field at $B_z = -(e/|e|)P_{\rm circ}B_{\rm CR}$ with $P_{\rm circ} = i(E_xE_y^* - E_yE_x^*)/|\boldsymbol{E}|^2$ equals +1(-1) for right-(left-) handed circularly polarized radiation. The photocurrent (Eq. (74)) in the vicinity of the CR is given by

$$J_y^{\rm circ} = \frac{\mathrm{sign}(B_z)c\tau\eta I}{B_{\rm CR}}. \tag{79}$$

The edge photocurrent calculated after Eqs. (74) and (75) as a function of the magnetic field is presented in Fig. 36(a). It shows the electric current for two linear polarization states where $(E_xE_y^* + E_yE_x^*)/|\boldsymbol{E}|^2 = \pm 1$ which is the case for $\alpha = 45°$ and 135°. For the calculations similar parameters are used as for the fit in Fig. 33(c) showing the photovoltage for $U_{\rm g}^{\rm eff} = 15\,\mathrm{V}$, see also Tab. 4. The edge photocurrent exhibits two sharp CRs at $B = \pm 2.4\,\mathrm{T}$ with a

magnitude weakly depending on the polarization state and a sign varying with the magnetic field polarity. The polarization dependence of the edge current for different magnetic field strengths is presented in Fig. 36(b). While the photocurrent at $B = 0$ ($\omega_c = 0$) has an opposite sign for $\alpha = 45°$ and $135°$, at CR ($\omega_c = \omega$) it is the same for both polarisation states. These calculations are in good agreement with the experimental observations, see Figs. 22 and 24 for zero magnetic field and Figs. 30(a) and 32 for $\omega = \omega_c$. Note that the experimental results are presented for low carrier densities, i.e. in the quantum mechanical limit, because of superimposing SdH-related oscillations at higher densities. Therefore, the data can not be fully compared to the curves in Fig. 36 which were calculated for the semi-classical case. Nevertheless, it can be concluded that the photocurrent has a weak polarization dependence $\propto \sin(2\alpha)$. Above and below the fields for the CR ($\omega_c = 0.75\,\omega$ and $\omega_c = 1.25\,\omega$) the edge current follows $\cos(2\alpha)$. Numerical calculations of the edge current density $j_y(x)$ are presented in Fig. 36(c) obtained for circularly polarized light at $\omega_c\tau \gg 1$. It demonstrates that the current flows mainly along the edges within a region as wide as the cyclotron diameter $l_c = 2l_0/(\omega_c\tau)$. The latter is much smaller than the mean free path l_0 at these conditions. Different to that, at zero magnetic field, i.e. $\omega_c = 0$, the current distribution extends over a much larger length being $\sim l_0$.

6 THz induced circular Hall effect in graphene

Beside the effects which are quadratic in the electric field $\boldsymbol{E}$, shown in Chap. 5, also phenomena proportional to higher orders of $\boldsymbol{E}$ have been observed. These include μ-photoconductivity (see Chap. 2.3) and a circular Hall effect excited in the absence of a magnetic field. In this chapter the observation of this effect in mono-layer graphene is reported. The dc Hall effect manifests the time inversion symmetry breaking induced by circularly polarized terahertz radiation.

In the following the corresponding results on transverse photoconductivity measurements in mono-layer graphene samples MLG #2 and #4 using circularly polarized THz radiation are presented. It starts with the experimental results and concludes with a subsequent discussion. The results are published in Ref. [34].

6.1 Experimental results

Illumination of the samples with circularly polarized THz radiation in the presence of a static electric field, provided by an applied bias voltage V^{dc}, results in a helicity-sensitive Hall photoresponse, see Fig. 37. The signals are picked up across the sample between contact pairs in y-direction, while the bias voltage is applied in x-direction [5], see Setup in Fig. 14(b) in Chap. 3. It is important to mention that in all measurements shown in this chapter the magnetic field is zero.

Figure 37(a) shows the transverse photosignal U_y as a function of the applied bias voltage V_x^{dc} for right- and left-handed circularly polarized radiation, σ^+ and σ^-, respectively. It shows that at a fixed radiation helicity the signals' magnitude and sign can be controlled by the applied bias voltage. The signal vanishes at $V_x^{\mathrm{dc}} = 0$ and increases (decreases) almost linearly up to $V_x^{\mathrm{dc}} \approx \pm 0.2\,\mathrm{V}$, while at higher bias voltages it tends to saturate. Importantly, the signal has consistently the opposite sign for opposite bias voltage polarity. This demonstrates that the main signal comes from the change of the sample's dc conductivity [6].

[5] Note that in some measurements the bias voltage was applied between contacts neighbouring the source and drain contacts which were broken. This, however, had no apparent effect on the signal detected across the sample in the middle of the Hall bar.

[6] Note that excitation of graphene may also produce photogalvanic currents [26, 32]. Since this chapter is devoted to the photoconductivity, no further discussion will be provided here. Experimental results and discussion on the photocurrent can be found in Ref. [32].

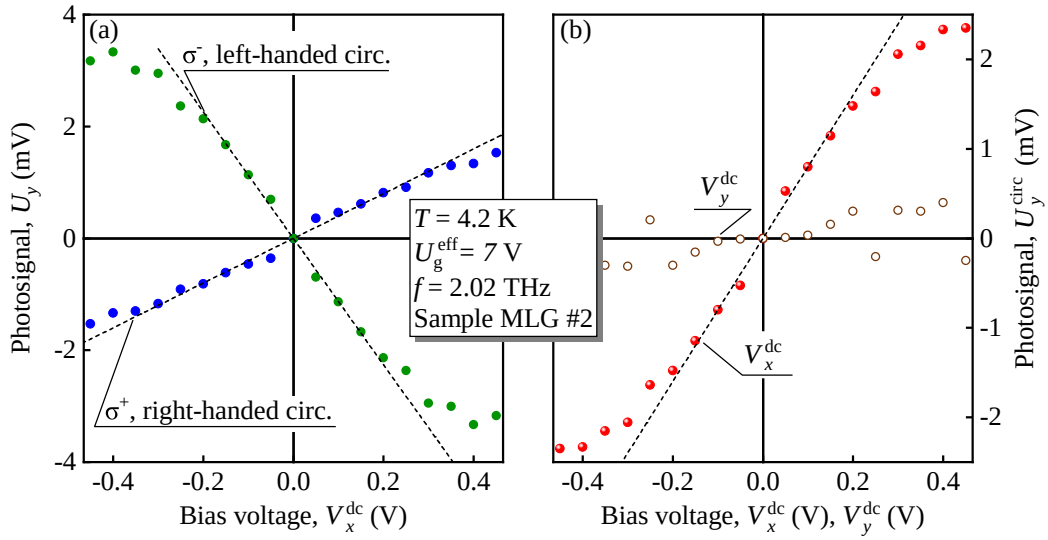

Figure 37: (a) Hall photosignal picked up perpendicular to the applied dc bias voltage V_x^{dc} as a function of V_x^{dc} for right-and left-handed circularly polarized radiation. (b) Helicity dependent contribution $U_y^{\mathrm{circ}} = (U_y^{\sigma^+} - U_y^{\sigma^-})/2$ of the Hall signal (full dots) and the longitudinal signal (open dots). The dashed lines are linear fits as guide for the eye. Adapted from Ref. [34]

Strikingly, the inversion of the radiation helicities from σ^+ to σ^- also results in an inversion of the photosignal, see Fig. 37(a). Measurements with the usage of a rotating $\lambda/4-$plate revealed a behaviour of the signal which closely follows the degree of circular polarization $P_{\mathrm{circ}} = (I^{\sigma^+} - I^{\sigma^-})/(I^{\sigma^+} + I^{\sigma^-})$, i.e. $U_y \propto P_{\mathrm{circ}}$ (not shown). Here, I^{σ^+,σ^-} are corresponding intensities. It is important to note, that such a helicity dependent signal was only detected for the transverse (Hall) configuration, i.e. signal U_y detected normal to the applied dc voltage V_x^{dc}. For the longitudinal photoresponse, i.e. signal detected in same direction as the bias voltage, the situation is different. Here, the signals for right- and left-handed circularly polarized radiation are almost identical. This becomes apparent in Fig. 37(b), where the helicity dependent signal was extracted as

$$U_y^{\mathrm{circ}} = \frac{U_y^{\sigma^+} - U_y^{\sigma^-}}{2} \tag{80}$$

with $U_y^{\sigma^+}$ and $U_y^{\sigma^-}$ corresponding to photosignals excited by right- and left-handed circularly polarization, respectively. Figure 37(b) shows the circular photoresponse as a function of the bias voltage V_x^{dc} for the Hall as well as for the longitudinal signal. The latter one is almost zero and has an opposite sign for opposite V_x^{dc} polarities, similar to the Hall response.

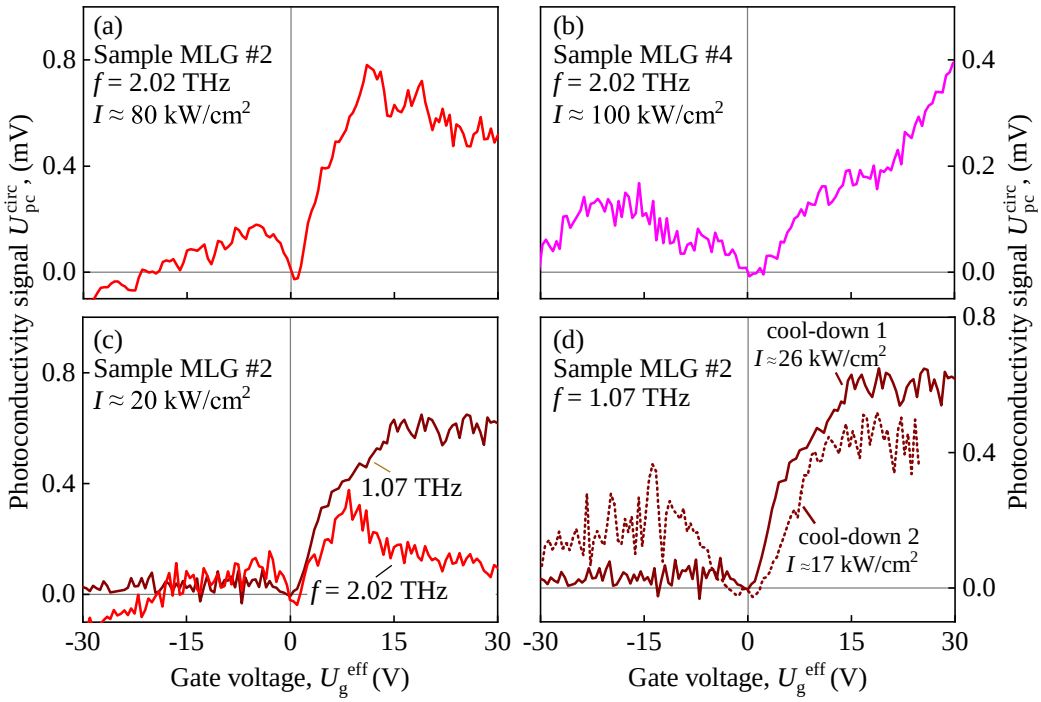

Figure 38: The transversal photoconductivity $U_{\rm pc}^{\rm circ}$ calculated after Eqs. (80) and (81) as a function of the gate voltage $U_{\rm g}^{\rm eff}$. (a) $U_{\rm pc}^{\rm circ}$ detected in sample MLG #2 at a frequency of $f = 2.02\,\mathrm{THz}$ and with an intensity of $I \approx 80\,\mathrm{kW/cm^2}$. (b) $U_{\rm pc}^{\rm circ}$ measured in sample MLG #4 at the same frequency and $I \approx 100\,\mathrm{kW/cm^2}$. (c) $U_{\rm pc}^{\rm circ}$ in sample MLG #1 as a function of $U_{\rm g}^{\rm eff}$ for two different frequencies $f = 2.02$ and $f = 1.07\,\mathrm{THz}$ at $I \approx 20\,\mathrm{kW/cm^2}$. (d) $U_{\rm pc}^{\rm circ}$ measured after two different sample cooldown on sample MLG #2 at a frequency $f = 1.07\,\mathrm{THz}$. $U_{\rm pc}^{\rm circ}$ was calculated using data measured at $V_x^{\rm dc} = \pm 0.2$ V for sample MLG #2 and $V_x^{\rm dc} = \pm 0.1$ V for sample MLG #4 at $T = 4.2\,\mathrm{K}$. Adapted from Ref. [34]

As demonstrated in Fig. 37 the sign change of the signal upon switching the bias voltage polarity is consistent and was detected in all measurements. The signals' magnitude, however, was slightly different for negative and positive bias voltages. This can be attributed to possible contributions coming from photocurrent generation [26, 32], which will not be further discussed in this chapter. Since the photogalvanic current is insensitive to the bias voltage polarity, the photoconductivity contribution $U_{\rm pc}^{\rm circ}$ can be extracted from the measured signal following

$$U_{\rm pc}^{\rm circ} = \frac{U_y^{\rm circ}(V_x^{\rm dc}) - U_y^{\rm circ}(-V_x^{\rm dc})}{2}. \tag{81}$$

Note that in the following only this helicity dependent photocductivity signal

is considered.

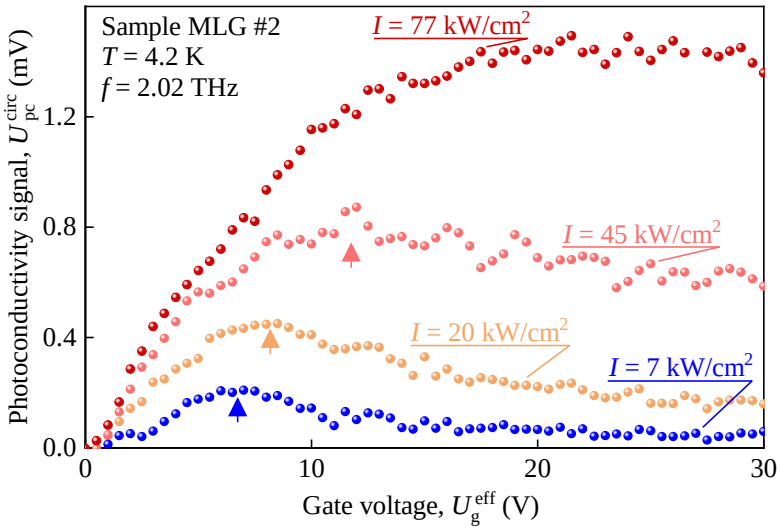

Figure 39: Helicity dependent contribution of the Hall photoconductivity signal $U_{\mathrm{pc}}^{\mathrm{circ}}$ as a function of the effective gate voltage $U_{\mathrm{g}}^{\mathrm{eff}}$ presented for four different radiation intensities I. The maxima of $U_{\mathrm{pc}}^{\mathrm{circ}}(U_{\mathrm{g}}^{\mathrm{eff}})$ are indicated by vertical arrows. The applied dc bias voltage was $V_x^{\mathrm{dc}} = \pm 0.2\,\mathrm{V}$. Adapted from Ref. [34]

Changing the applied gate voltage $U_{\mathrm{g}}^{\mathrm{eff}}$ qualitatively changes the behaviour of the signal, see Fig. 38. Here, the circular photoconductivity signal $U_{\mathrm{pc}}^{\mathrm{circ}}$ is presented as a function of $U_{\mathrm{g}}^{\mathrm{eff}}$ for the samples MLG #2 and MLG #4, panel (a) and (b), respectively. It shows that in both samples the signal almost vanishes at the CNP, increases linearly at low $U_{\mathrm{g}}^{\mathrm{eff}}$, and than saturates or even decreases at higher $U_{\mathrm{g}}^{\mathrm{eff}}$. At low $U_{\mathrm{g}}^{\mathrm{eff}}$ the dependence is almost symmetric with the gate voltage, while at higher densities it is asymmetric. This becomes apparent, e.g. in Fig. 38(a): On positive gate voltages the signal first increases further up to $\approx 12\,\mathrm{V}$ and than decreases; at negative gate voltages it starts to decrease at much lower $U_{\mathrm{g}}^{\mathrm{eff}}$ and than even changes its sign. A similar dependence was observed for different radiation frequencies and lower intensities, shown in Fig. 38(c). Moreover, the asymmetry of the photoconductive signal with respect to the gate voltage was different for different sample cool-downs, see Fig. 38(d). While at positive gate voltages functional behaviour as well as the amplitude is almost the same for both cool-downs, it is different for negative voltages exhibiting an almost zero signal for the second cool down. In the following discussion the focus lies on positive gate voltages.

Figure 39 presents the gate voltage dependence of the circular photoconductive signal $U_{\mathrm{pc}}^{\mathrm{circ}}$ for various radiation intensities I. For all intensities the signal

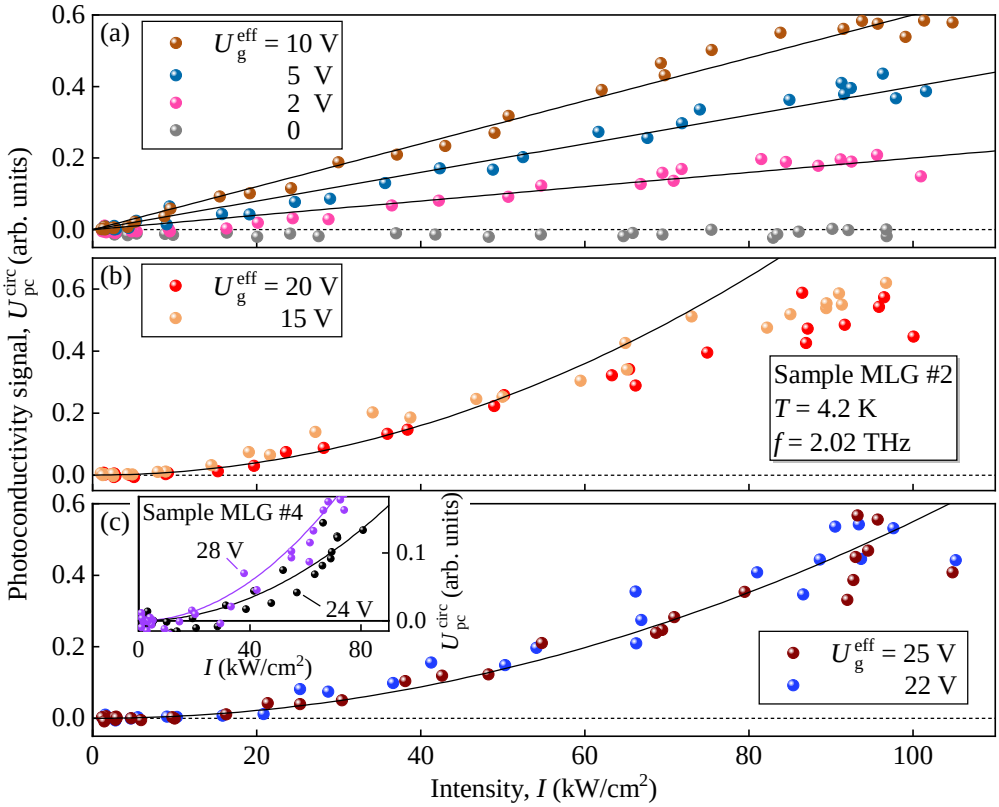

Figure 40: U_{pc}^{circ} as a function of the radiation intensity for various U_g^{eff} at f = 2.02 THz and $V_x^{dc} = \pm 0.2$ V detected in sample MLG #2. Panel (a) shows the data for $U_g^{eff} \leqq 10$ V. Solid lines are linear fits after $U_{pc}^{circ} = aI$ with a = 2, 4 and 6 μV cm^2/kW. Panels (b) and (c) present data at higher U_g^{eff} where solid lines are fits after $U_{pc}^{circ} = AI^2$. The inset presents the intensity dependences at U_g^{eff} = 24 and 28 V measured on sample MLG #4 under f = 2.02 THz excitation and $V_x^{dc} = \pm 0.1$ V dc bias. The obtained coefficients are A = 0.1 (b), 0.055 (c), 0.021 and 0.036 (inset), in units of μV cm^4/kW^2. Adapted from Ref. [34]

first increases up to a maximum value, then saturates and decreases at high U_g^{eff}. The position of the maximum slightly shifts to lower gate voltages for lower radiation intensities. This is visualized by vertical arrows indicating the maximum position.

To further analyse the dependence of the photoconductivity signal on the radiation intensity, measurements at fixed gate voltages were done, where the radiation intensity was varied up to $I \approx 100$ kW/cm^2 for f = 2.02 THz, see Fig. 40. Panel (a) presents the intensity dependence in the low density regime $U_g^{eff} \leq 10$ V exhibiting a linear behaviour. At higher gate voltages the situation changes, see Fig. 40(b) and (c). Here, the dependence becomes superlinear. In particular, at voltages > 20 V, the behaviour of U_{pc}^{circ} can be well fitted by

$U_{\mathrm{pc}}^{\mathrm{circ}} = A(f) \times I^2$ with the frequency dependent fit parameter $A(f)$. Similar results as in sample MLG #2 are obtained in sample MLG #4, shown in the inset of Fig. 40.

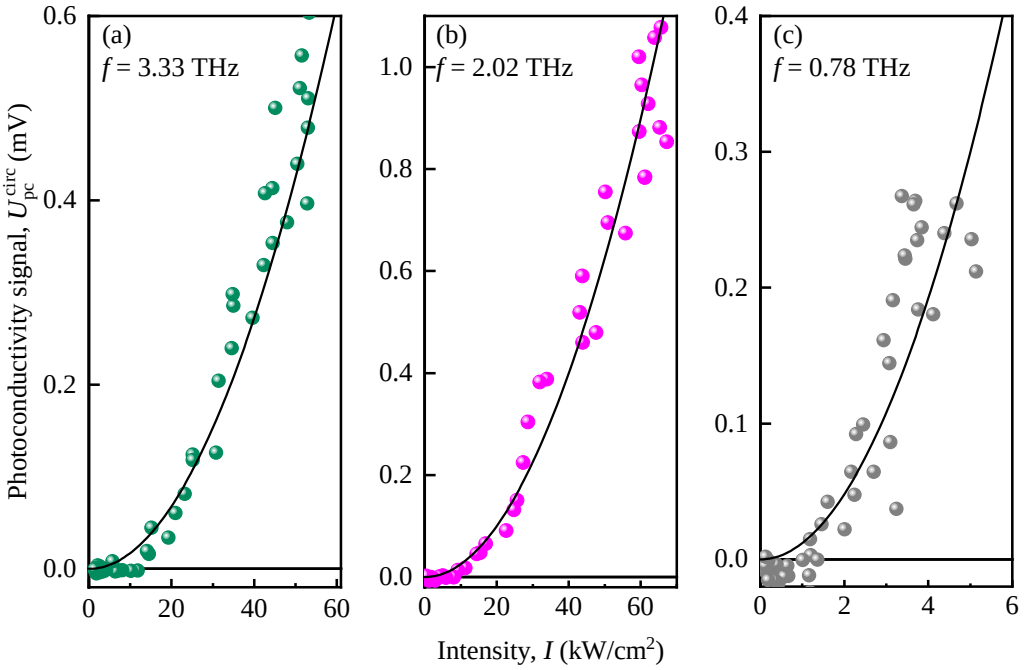

Figure 41: Photoconductivity signal $U_{\mathrm{pc}}^{\mathrm{circ}}$ as a function of the radiation intensity for three different radiation frequencies at $V_x^{\mathrm{dc}} = \pm 0.2\,\mathrm{V}$ and $U_{\mathrm{g}}^{\mathrm{eff}} = 30\,\mathrm{V}$. (a) $f = 3.33\,\mathrm{THz}$, (b) $f = 2.02\,\mathrm{THz}$, and (c) $f = 0.78\,\mathrm{THz}$. The solid lines are fits after $U_{\mathrm{pc}}^{\mathrm{circ}} = AI^2$ yielding the parameters $A = 0.17$, 0.25, and 12, with units $\mu\mathrm{V\ cm^4/kW^2}$, in panels (a), (b), and (c), respectively. Adapted from Ref. [34]

By variation of the radiation frequency the superlinearity at high gate voltages remains, but the coefficient $A(f)$ changes, see Fig. 41. It increases with decreasing radiation frequency, e.g. for $f = 3.33\,\mathrm{THz}$ (panel (a)) $A = 0.17\,\mu\mathrm{Vcm^4/kW^2}$ while for $f = 0.78\,\mathrm{THz}$ $A = 12\,\mu\mathrm{Vcm^4/kW^2}$ yielding a ratio $A(0.78\,\mathrm{THz})/A(3.33\,\mathrm{THz}) \approx 70$. It is important to note that the peak intensities of the laser radiation decrease with decreasing laser frequency at the laser system used in this work.

Beside investigation of the Hall response also the longitudinal photoconductivity was studied. Figure 42(a) presents the longitudinal photoconductivity detected in a two-terminal measurement setup where two contacts along the Hall bar where used (see also Fig. 23). It shows the longitudinal photoconductivity signal $U_{\mathrm{pc},xx}$ calculated using the voltage drops U_x measured at $V_x^{\mathrm{dc}} = \pm 0.3\,\mathrm{V}$ for right- and left-handed circular polarization. The inten-

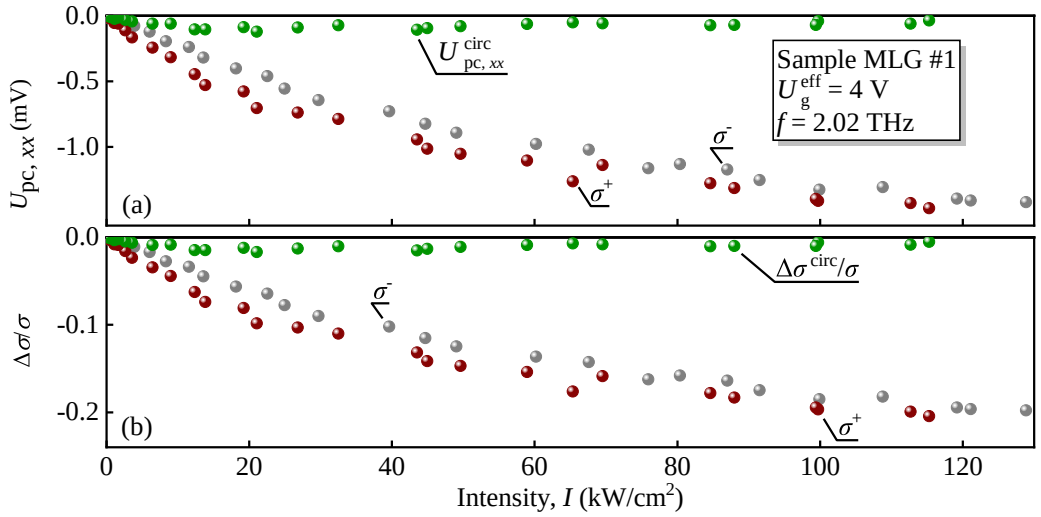

Figure 42: The intensity dependence of (a) the longitudinal two terminal photoconductivity signal $U_{\mathrm{pc},xx}$ and (b) the corresponding normalized longitudinal photoconductivity $\Delta\sigma/\sigma$ for σ^+ and σ^- polarization. The helicity dependent signal (Equ. (80)) and photoconductivity, $U^{\mathrm{CR}}_{\mathrm{pc},xx}$ and $\Delta\sigma^{\mathrm{circ}}/\sigma$, respectively, are also shown in both panels (marked by superscript circ) demonstrating that the helicity dependent part of the longitudinal photoconductivity is vanishingly small in comparison with the total signal. These data were obtained in sample MLG #1 at $V_x^{\mathrm{dc}} = \pm 0.3\,\mathrm{V}$. Adapted from Ref. [34]

sity dependence shows a linear behaviour at low intensities and a saturation at higher ones. In Fig. 42(b) the corresponding calculated relative photo-induced change of the longitudinal conductivity normalized to the dark conductivity $\Delta\sigma/\sigma$ is shown. The behaviour of $\Delta\sigma/\sigma$ reveals that the conductivity decreases upon irradiation. This is consistent with the negative μ-photoconductivity phenomenon where electron gas heating results in a reduction of the carrier mobilities, see Chap. 2.3 and for review Refs. [29, 136–141].

Moreover, Fig. 42 demonstrates that the longitudinal signal does not depend on the radiation helicity. Indeed, the helicity dependent part $U^{\mathrm{circ}}_{\mathrm{pc},xx}$ is close to zero. This is in sharp contrast to the transverse photoconductivity signal shown above. The small difference between the signal for σ^+ and σ^- may result from imperfections or misalignments of the implemented $\lambda/4$-plate.

6.2 Discussion

In the discussion of the experimental results a phenomenological theory based on general symmetry arguments will be introduced and compared to the exper-

imental observations. When a biased isotropic system is excited with spatially homogeneous terahertz radiation at normal incidence the lowest-order dc photocurrent is linear in the dc electric field E_x^{dc} and quadratic in the radiation electric field given by $\boldsymbol{E}\exp(-i\omega t)+\boldsymbol{E}^*\exp(i\omega t)$, see Eq. 41 in Chap. 2. The generated photocurrent can be fully characterized by three transport coefficients γ_k, given by [74]

$$\begin{aligned} j_x &= (\gamma_1+\gamma_2 S_1)|\boldsymbol{E}|^2 E_x^{\mathrm{dc}}, \\ j_y &= (\gamma_2 S_2+\gamma_3 S_3)|\boldsymbol{E}|^2 E_x^{\mathrm{dc}} \end{aligned} \tag{82}$$

where S_1 and S_2 are the Stokes parameters for linear polarization and S_3 the one describing circular polarization. In the case of circular polarization relevant for this work the anisotropic terms $\propto S_1 = S_2 = 0$ vanish. Therefore, the photoresponse reduces to

$$\begin{aligned} j_x &= \gamma_1|\boldsymbol{E}|^2 E_x^{\mathrm{dc}}, \\ j_y &= \eta\gamma_3|\boldsymbol{E}|^2 E_x^{\mathrm{dc}}. \end{aligned} \tag{83}$$

Here, $\eta = \pm 1$ corresponds to the helicity of the radiation field representing the two possible values for $S_3 = \pm 1$ for right- and left-handed circular polarization. Equation (83) yields a form of j_y which is equivalent to the description of the conventional Hall effect with the circular polarized radiation being the time-reversal breaking field instead of the magnetic field. The corresponding diagonal and Hall components of the photoconductivity tensor are even and odd with respect to the helicity η. This is in good agreement with the experimental observations of the Hall photoresponse shown in Figs. 37-41 and the longitudinal response presented in Fig. 37(b)[7].

In general, the THz radiation induced photoconductivity may result from either direct interband or indirect intraband optical transitions resulting from scattering-assisted free carrier absorption. At low temperatures, however, interband processes require photon energies larger than twice the Fermi energy and thus this contribution should be maximal around the CNP and vanish for higher $U_{\mathrm{g}}^{\mathrm{eff}}$. Strikingly, the experimental results show a contrary behaviour (see, e.g. Fig. 38), and, therefore, interband optical transitions can be ne-

[7]Note that in Fig. 37(b) the longitudinal signal j_y was measured while the bias voltage was applied across the Hall bar, along $y-$direction. An example for the longitudinal component detected in $x-$ direction with bias applied along the long side of the Hall bar is provided in Fig. 23.

glected.

High intensity radiation may also lead to a significant modification of the energy spectrum of graphene [142]. But due to the low THz photon energies such effects are neglected here. Therefore, the following discussion focusses on photosignals arising from scattering-assisted intraband processes.

At low carrier densities ($U_{\mathrm{g}}^{\mathrm{eff}} < 10\,\mathrm{V}$) the observed photoconductivity signal $U_{\mathrm{pc}}^{\mathrm{circ}}$ increases linearly with $U_{\mathrm{g}}^{\mathrm{eff}}$ and is almost symmetric around the CNP, see Fig. 38. Furthermore, in agreement with Eq. (83) $U_{\mathrm{pc}}^{\mathrm{circ}}$ has a linear dependence on the radiation intensity $I \propto |\boldsymbol{E}|^2$, see Fig. 40(a).

Quite recently, the kinetic theory of the lowest-order transverse photoconductivity in two-dimensional systems was developed, see Ref. [143]. This semi-classical approach based on the Boltzmann equation shows that the Hall photocurrent j_y given by Eq. (83) involves two contributions. The first one corresponds to optical alignment of the carrier momenta associated with the second angular harmonic of the distribution function expanded in a series over the electric field, and the second one to dynamic heating and cooling of the electron gas corresponding to the zeroth angular harmonic. Both contributions oscillate with time and appear at the second pertubation order to the equilibrium Fermi distribution, perturbed by the THz and static electric fields. Corresponding perturbation magnitudes depend on the dynamic relaxation rates $\tau_{n\omega}^{-1} = \tau_n^{-1} - i\omega$ with τ_n^{-1} being the relaxation rate of the nth static angular harmonics. In Ref. [143] the explicit form of Eq. (83) for graphene was found

$$\gamma_3 = \sigma_0 e^2 v^2 \mathrm{Im}\left\{\alpha_\omega \tau_{0\omega}\Big[\frac{\tau_1}{\varepsilon} + \frac{\varepsilon}{2}\Big(\frac{\tau_1}{\varepsilon}\Big)'\Big]' - \frac{\alpha_\omega \varepsilon^2}{2}\Big[\frac{\tau_{2\omega}}{\varepsilon}\Big(\frac{\tau_1}{\varepsilon}\Big)'\Big]' - 2\alpha_\omega \tau_{2\omega}\Big(\frac{\tau_1}{\varepsilon}\Big)'\right\}_{\varepsilon=\varepsilon_{\mathrm{F}}}, \tag{84}$$

with the static conductivity $\sigma_0 = e^2\varepsilon_{\mathrm{F}}\tau_1/\pi\hbar^2$, the elementary charge e, the Fermi energy ε_{F}, and $\alpha_\omega = 1 + (1 - i\omega\tau_1)^{-1}$. The primes indicate derivatives with respect to the kinetic energy ε taken at $\varepsilon = \varepsilon_{\mathrm{F}}$.

Equation (84) demonstrates that the circular photoconductivity $\sigma_{x,y} = -\eta\gamma_3|\boldsymbol{E}|^2$ is determined by the scattering rates $\tau_1^{-1}(\varepsilon)$ and $\tau_2^{-1}(\varepsilon)$ in the vicinity of the Fermi surface. These rates depend on the microscopic nature of the scattering. In particular, in case of Coulomb scattering $\tau_1 = 2\tau_2 \propto \varepsilon$ the term γ_3 vanishes. Such scattering events are dominant in graphene at low carrier densities near the CNP. This is in good agreement with the experimental ob-

servations where the photoconductivity signal is almost zero at the CNP, see Figs. 38, 39.

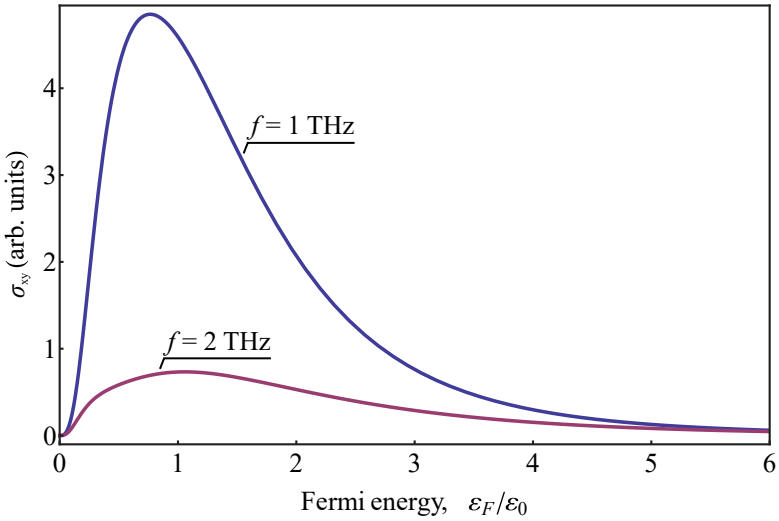

Figure 43: Circular Hall photoconductivity $\sigma_{xy} = -\eta\gamma_3|E|^2$ calculated with Eq. (84) for the model $\tau_1 = 2\tau_2 \propto \varepsilon/(\varepsilon^2+\varepsilon_0^2)$ combining short-range and Coulomb scattering at $f = 1$ and 2 THz, $\omega\tau_n \gg 1$, and $\eta = 1$. Adapted from Ref. [34]

Since the relevant scattering times $\tau_0 \gg \tau_1 \sim \tau_2 \sim 1\,\mathrm{ps}$ are much longer thant $1/\omega$ the limit $\omega\tau_n \gg 1$ is most important in this work. In this regime, where $\alpha_\omega \approx 1$ and $\tau_{0\omega}, \tau_{2\omega} \approx i\omega^{-1}$, the terms corresponding to dynamic heating $\propto \tau_{0\omega}$ and optical alignment $\propto \tau_{2\omega}$ cancel each other in Eq. (84). This results in a frequency dependence of γ_3 being $\propto \omega^{-3}$. In the particular case where $\tau_1 = 2\tau_2 \propto \varepsilon^{-1}$ describing short-range scattering, Eq. (84) reduces to $\gamma_3 = -6e^4v^2/\pi\hbar^2\omega^3\varepsilon_\mathrm{F}$ in the high-frequency limit. A mixture of Coulomb and short-range scattering is given at $\tau_1 = 2\tau_2 \propto \varepsilon/(\varepsilon^2+\varepsilon_0^2)$ [143] where ε_0 is a parameter. The corresponding calculated circular Hall photoconductivity σ_{xy} exhibits a maximum at an intermediate carrier density where $\varepsilon_\mathrm{F} = \varepsilon_0$ and decreases towards the CNP as well as towards higher carrier densities, see Fig. 43.

The theory introduced above qualitatively describes well the experimental observations at low and intermediate gate voltages. Indeed, the detected circular Hall photoconductivity has the following properties: It reverses its sign with the change of the radiation helicity and scales linearly with the intensity, see Fig. 40(a). The signal is almost zero in the vicinity of the CNP and increases almost symmetrically with increasing $U_\mathrm{g}^\mathrm{eff}$, see Figs. 38 and 39. Moreover, at low radiation intensities the model also fits well to the experimental data at higher carrier densities. Figure 39 shows that at low radiation

intensities the photoconductivity signal increases with increasing $U_{\mathrm{g}}^{\mathrm{eff}}$ up to a maximum and than decreases with higher $U_{\mathrm{g}}^{\mathrm{eff}}$, in agreement with Fig. 43.

The situation, however, changes at higher radiation intensities and high carrier densities. The increase of $U_{\mathrm{g}}^{\mathrm{eff}}$ qualitatively changes the intensity dependence, see Figs. 40(b), 40(c) and Fig. 41. Importantly, the circular Hall photoconductivity scales with the squared radiation intensity $\propto |\boldsymbol{E}|^4$, and therefore, can no longer be described by Eqs. (83) and (84). In the description of the photoconductivity in this regime higher-order terms $\propto \gamma_3^{(4)}|\boldsymbol{E}|^4$ should be taken into account within the semi-classical approach of Ref. [143]. Such a theory should consider excitation of a larger number of different time and angular harmonics of the distribution function. Moreover, it should explain the dominance of the term $\propto \gamma_3^{(4)}|\boldsymbol{E}|^4$ over $\gamma_3^{(2)}|\boldsymbol{E}|^2$ at increasingly lower gate voltages for lower intensities which would produce the observed shift of the photosignals' maxima with the radiation intensity, see Fig. 39.

7 Conclusion

Within this work terahertz radiation-induced optoelectronic phenomena in HgTe-based, three-dimensional topological insulators and graphene-based systems were studied. Both materials can be described within the Dirac theory in the zero-mass limit, but while the spin-orbit interaction in HgTe is fairly large, it is vanishingly small in graphene. In the framework of this thesis several novel phenomena excited by THz radiation were observed in these materials, including edge photocurrents in mono- and bi-layer graphene [31, 32], cyclotron resonance in bi-layer graphene [33] as well as in 3D HgTe TIs [30], and the circular Hall effect at zero magnetic field in mono-layer graphene [34]. In particular, it was shown that homogeneous illumination with THz radiation effectively results in a photocurrent proportional to the second order of the electric field. Most of the observed phenomena have been studied in a regime where the photon energy is smaller than the Fermi energy, which allowed the development of a semi-classical theory based on the Boltzmann kinetic equation. Furthermore, in bi-layer graphene photocurrents due to inter Landau level transitions were detected at small Fermi energies which belong to the quantum mechanical regime. In mono-layer graphene, an effect proportional to the third order of the electric field was observed, the circular Hall effect. Here, the time-reversal symmetry breaking is induced by circularly polarized THz radiation and not by a magnetic field. The experimental results and subsequent discussions corresponding to the observed effects are provided in Chaps. 4, 5, and 6.

Chapter 4 is devoted to the observation of cyclotron resonance of top and bottom surface states in 200 nm thick partially strained HgTe films and focusses on the photocurrent and transmission data [30]. It was shown that excitation with continuous wave terahertz radiation results in a strong enhancement of the photogalvanic current at cyclotron resonance. In the performed magnetogalvanic measurements two separate resonances were detected which show characteristic cyclotron resonance behaviour, like helicity and linear frequency dependence. An additional detection of the magnetotransmission revealed dips at very similar positions. It was verified, that these resonances stem from top and bottom surface states of the HgTe film. This conclusion is supported on the one hand, by photocurrent measurements at various gate voltages revealing a shifting of one of the resonances. On the other hand, it is supported by previous measurements on 80 nm HgTe films [38] as well as mag-

netotransport and capacitance data obtained from samples of the same 200 nm HgTe wafer [40]. All these findings demonstrate that despite the film being larger than the estimated critical thickness for lattice relaxation, topologically protected surface states persist. In accordance with the results, the microscopic theory, developed in cooperation with Dr. G. V. Budkin, describes the formation of the cyclotron-resonance-assisted photocurrents in the framework of asymmetric energy relaxation of photoexcited carriers [30].

Chapter 5 presents the experimental findings on edge photocurrents in mono- and bi-layer graphene induced by linearly polarized terahertz radiation. It was shown that in the absence of a magnetic field, the edge current is controlled by the orientation of the polarization plane of the THz field [31]. An additionally applied small magnetic field normal to the graphene plane leads to a phase shift in the polarization dependence. It was demonstrated that the current is generated in the vicinity of the edges within a strip limited by the mean free path and the screening length of the terahertz field. The microscopic theory, developed parallel to the experiments by Dr. M. V. Durnev from Ioffe Institute in St. Petersburg, describes the current formation with optical alignment of the free carrier momenta and P-symmetry breaking at the edges. In quantizing magnetic fields and at higher gate voltages, $1/B$-periodic oscillations in the photocurrent were detected which are linked to SdH-oscillations in the magnetoresistance [31]. Further measurements in bi-layer graphene exposed to strong magnetic fields revealed resonant features in the edge photocurrent [33]. A variety of experiments established that these resonances result from transitions between Landau levels. At low carrier densities, inter- and intralevel transitions take place. In the semi-classical regime, i.e. at high carrier densities, classical cyclotron-resonance-induced intralevel transitions appear. An interesting topic for further studies of terahertz-radiation-induced edge currents in graphene-based systems is the investigation of the $1/B$-periodic oscillations. Although their existence was observed in several measurements, their origin is not fully understood to date.

The observation of a dc Hall effect in mono-layer graphene induced by circularly polarized THz radiation and in the absence of an applied magnetic field, is reported in Chap. 6 [34]. It was demonstrated that the photoconductivity response is caused by free carrier absorption and reverses its sign upon switching the radiation helictiy. At low and intermediate carrier densities, the photoconductivity signal is shown to be proportional to the radiation intensity. In this regime the photosignal can be well described within an analytical

theory [143] taking into account the alignment of the carrier momenta as well as dynamic heating and cooling of the electron gas. In the high-carrier density regime the intensity-dependent photoresponse becomes superlinear and varies with the square of the radiation intensity. The understanding of this unusual behaviour at higher gate voltages is an interesting task for the future. It may be explained by an interplay between second- and fourth-order effects in the radiation electric field.

References

[1] M. Z. Hasan and C. L. Kane, *Colloquium: Topological Insulators*, Rev. Mod. Phys. **82**, 3045 (2010).

[2] C. L. Kane and E. J. Mele, *Z_2 Topological Order and the Quantum Spin Hall Effect*, Phys. Rev. Lett. **95**, 146802 (2005).

[3] A. H. C. Neto, F. Guinea, N. M. R. Peres, K. S. Novoselov, and A. K. Geim, *The electronic properties of graphene*, Rev. Mod. Phys. **81**, 109–162 (2009).

[4] K. S. Novoselov, A. K. Geim, S. V. Morozov, D. Jiang, Y. Zhang, S. V. Dubonos, I. V. Grigorieva, and A. A. Firsov, *Electric Field Effect in Atomically Thin Carbon Films*, Science **306**, 666 (2004).

[5] N. G. R. Ashoori and P. Jarillo-Herrero, *Graphene and Topological Insulators*, MIT Physics Annual (2015).

[6] X.-L. Qi, T. L. Hughes, S. Raghu, and S.-C. Zhang, *Time-Reversal-Invariant Topological Superconductors and Superfluids in Two and Three Dimensions*, Phys. Rev. Lett. **102** (2009).

[7] S.-Q. Shen, "Majorana Fermions in Topological Insulators", in *Springer Series in Solid-State Sciences* (Springer Singapore, 2017), pp. 189–206.

[8] M. I. Katsnelson, K. S. Novoselov, and A. K. Geim, *Chiral tunnelling and the Klein paradox in graphene*, Nat. Phys. **2**, 620–625 (2006).

[9] B. A. Bernevig and S.-C. Zhang, *Quantum Spin Hall Effect*, Phys. Rev. Lett. **96**, 106802 (2006).

[10] S. D. Ganichev, D. Weiss, and J. Eroms, *Terahertz Electric Field Driven Electric Currents and Ratchet Effects in Graphene*, Ann. Phys. **529**, 1600406 (2017).

[11] F. Xia, T. Mueller, Y. ming Lin, A. Valdes-Garcia, and P. Avouris, *Ultrafast graphene photodetector*, Nat. Nanotechnol. **4**, 839–843 (2009).

[12] P. A. M. Dirac, *The quantum theory of the electron*, Proceedings of the Royal Society of London. Series A, Containing Papers of a Mathematical and Physical Character **117**, 610–624 (1928).

[13] E. Malic and A. Knorr, *Graphene and Carbon Nanotubes: Ultrafast Relaxation Dynamics and Optics* (Wiley-VCH, 2013).

[14] S. Das Sarma, S. Adam, E. H. Hwang, and E. Rossi, *Electronic Transport in Two-dimensional Graphene*, Rev. Mod. Phys. **83**, 407 (2011).

[15] E. V. Castro, N. M. R. Peres, J. M. B. L. dos Santos, F Guinea, and A. H. C. Neto, *Bilayer graphene: gap tunability and edge properties*, J. Phys. Conf. Ser. **129**, 012002 (2008).

[16] E. McCann and V. I. Fal'ko, *Landau-level Degeneracy and Quantum Hall Effect in a Graphite Bilayer*, Phys. Rev. Lett. **96**, 086805 (2006).

[17] L. Fu and C. L. Kane, *Topological Insulators with Inversion Symmetry*, Phys. Rev. B **76**, 045302 (2007).

[18] J. E. Moore and L. Balents, *Topological Invariants of Time-reversal-invariant Band Structures*, Phys. Rev. B **75**, 121306(R) (2007).

[19] R. Roy, *Topological Phases and the Quantum Spin Hall Effect in Three Dimensions*, Phys. Rev. B **79**, 195322 (2009).

[20] F. Ortmann, S. Roche, and S. O. Valenzuela, eds., *Materials Topological Insulators: Fundamentals and Perspectives* (Wiley-VCH, 2015).

[21] E. L. Ivchenko and S. D. Ganichev, *Spin-photogalvanics*, edited by M. I. Dyakonov (Springer, Berlin Heidelberg, 2017).

[22] J. W. McIver, D. Hsieh, H. Steinberg, P. Jarillo-Herrero, and N. Gedik, *Control Over Topological Insulator Photocurrents with Light Polarization*, Nat. Nanotechnol. **7**, 96 (2012).

[23] P. Olbrich, C. Zoth, P. Vierling, K.-M. Dantscher, G. V. Budkin, S. A. Tarasenko, V. V. Bel'kov, D. A. Kozlov, Z. D. Kvon, N. N. Mikhailov, S. A. Dvoretsky, and S. D. Ganichev, *Giant Photocurrents in a Dirac Fermion System at Cyclotron Resonance*, Phys. Rev. B **87**, 235439 (2013).

[24] C. Kastl, C. Karnetzky, H. Karl, and A. W. Holleitner, *Ultrafast Helicity Control of Surface Currents in Topological Insulators with Near-unity Fidelity*, Nat. Commun. **6**, 7617 (2015).

[25] Z. D. Kvon, K. M. Dantscher, C. Zoth, D. A. Kozlov, N. N. Mikhailov, S. A. Dvoretsky, and S. D. Ganichev, *Terahertz Electron Transport in a Two-dimensional Topological Insulator in a HgTe Quantum Well*, JETP Lett. **99**, 290–294 (2014).

[26] M. M. Glazov and S. D. Ganichev, *High Frequency Electric Field Induced Nonlinear Effects in Graphene*, Phys. Rep. **535**, 101 (2014).

[27] J. Karch, C. Drexler, P. Olbrich, M. Fehrenbacher, M. Hirmer, M. M. Glazov, S. A. Tarasenko, E. L. Ivchenko, B. Birkner, J. Eroms, D. Weiss, R. Yakimova, S. Lara-Avila, S. Kubatkin, M. Ostler, T. Seyller, and S. D. Ganichev, *Terahertz Radiation Driven Chiral Edge Currents in Graphene*, Phys. Rev. Lett. **107**, 276601 (2011).

[28] H. Plank, M. V. Durnev, S. Candussio, J. Pernul, K.-M. Dantscher, E. Mönch, A. Sandner, J. Eroms, D. Weiss, V. V. Bel'kov, S. A. Tarasenko, and S. D. Ganichev, *Edge Currents Driven by Terahertz Radiation in Graphene in Quantum Hall Regime*, 2D Mater. **6**, 011002 (2018).

[29] S. D. Ganichev and W. Prettl, *Intense Terahertz Excitation of Semiconductors* (Oxford University Press, Oxford, Dec. 2005).

[30] S. Candussio, G. V. Budkin, M. Otteneder, D. A. Kozlov, I. A. Dmitriev, V. V. Bel'kov, Z. D. Kvon, N. N. Mikhailov, S. A. Dvoretsky, and S. D. Ganichev, *Cyclotron-resonance-induced photogalvanic effect in surface states of 200-nm-thick strained HgTe films*, Phys. Rev. Mater **3**, 054205 (2019).

[31] S. Candussio, M. V. Durnev, S. A. Tarasenko, J. Yin, J. Keil, Y. Yang, S.-K. Son, A. Mishchenko, H. Plank, V. V. Bel'kov, S. Slizovskiy, V. Fal'ko, and S. D. Ganichev, *Edge Photocurrent Driven by Terahertz Electric Field in Bilayer Graphene*, Phys. Rev. B **102**, 045406 (2020).

[32] S. Candussio, L. E. Golub, S. Bernreuter, T. Jötten, T. Rockinger, K. Watanabe, T. Taniguchi, J. Eroms, D. Weiss, and S. D. Ganichev, *Nonlinear intensity dependence of edge photocurrents in graphene induced by terahertz radiation*, Phys. Rev. B **104**, 155404 (2021).

[33] S. Candussio, M. V. Durnev, S. Slizovskiy, T. Jötten, J. Keil, V. V. Bel'kov, J. Yin, Y. Yang, S.-K. Son, A. Mishchenko, V. Fal'ko, and S. D. Ganichev, *Edge Photocurrent in Bilayer Graphene Due to Inter-landau-level Transitions*, Phys. Rev. B **103**, 125408 (2021).

[34] S. Candussio, S. Bernreuter, T. Rockinger, K. Watanabe, T. Taniguchi, J. Eroms, I. A. Dmitriev, D. Weiss, and S. D. Ganichev, *Terahertz radiation induced circular Hall effect in graphene*, Phys. Rev. B **105**, 155416 (2022).

[35] H. Zhang, C.-X. Liu, X.-L. Qi, X. Dai, Z. Fang, and S.-C. Zhang, *Topological Insulators in Bi_2se_3, Bi_2te_3 and Sb_2te_3 with a Single Dirac Cone on the Surface*, Nat. Phys. **5**, 438 (2009).

[36] X. Dai, T. L. Hughes, X.-L. Qi, Z. Fang, and S.-C. Zhang, *Helical Edge and Surface States in HgTe Quantum Wells and Bulk Insulators*, Phys. Rev. B **77**, 125319 (2008).

[37] C. Brüne, C. X. Liu, E. G. Novik, E. M. Hankiewicz, H. Buhmann, Y. L. Chen, X. L. Qi, Z. X. Shen, S. C. Zhang, and L. W. Molenkamp, *Quantum Hall Effect from the Topological Surface States of Strained Bulk HgTe*, Phys. Rev. Lett. **106**, 126803 (2011).

[38] K.-M. Dantscher, D. A. Kozlov, P. Olbrich, C. Zoth, P. Faltermeier, M. Lindner, G. V. Budkin, S. A. Tarasenko, V. V. Bel'kov, Z. D. Kvon, N. N. Mikhailov, S. A. Dvoretsky, D. Weiss, B. Jenichen, and S. D. Ganichev, *Cyclotron-resonance-assisted Photocurrents in Surface States of a Three-dimensional Topological Insulator Based on a Strained High-mobility HgTe Film*, Phys. Rev. B **92**, 165314 (2015).

[39] A. M. Shuvaev, G. V. Astakhov, C. Brüne, H. Buhmann, L. W. Molenkamp, and A. Pimenov, *Terahertz Magneto-optical Spectroscopy in HgTe Thin Films*, Semicond. Sci. Technol. **27**, 124004 (2012).

[40] M. L. Savchenko, D. A. Kozlov, N. N. Vasilev, Z. D. Kvon, N. N. Mikhailov, S. A. Dvoretsky, and A. V. Kolesnikov, *Topological surface states in thick partially relaxed HgTe films*, Phys. Rev. B **99**, 195423 (2019).

[41] A. H. Castro Neto, F. Guinea, N. M. R. Peres, K. S. Novoselov, and A. K. Geim, *The Electronic Properties of Graphene*, Rev. Mod. Phys. **81**, 109 (2009).

[42] S.-Q. Shen, W.-Y. Shan, and H.-Z. Lu, *Topological Insulator and the Dirac Equation*, SPIN **01**, 33 (2011).

[43] S.-Q. Shen, *Topological Insulators: Dirac Equation in Condensed Matters* (Springer, Berlin Heidelberg, 2012).

[44] W. Nolting, *Grundkurs Theoretische Physik 5/2 Quantenmechanik - Methoden und Anwendungen* (Springer Berlin Heidelberg, Berlin, Heidelberg, 2012).

[45] H. Weyl, *Elektron Und Gravitation. I*, Z. Phys. **56**, 330 (1929).

[46] K. v. Klitzing, G. Dorda, and M. Pepper, *New Method for High-accuracy Determination of the Fine-structure Constant Based on Quantized Hall Resistance*, Phys. Rev. Lett. **45**, 494–497 (1980).

[47] L. Fu, C. L. Kane, and E. J. Mele, *Topological Insulators in Three Dimensions*, Phys. Rev. Lett. **98**, 106803 (2007).

[48] B. Zhou, H.-Z. Lu, R.-L. Chu, S.-Q. Shen, and Q. Niu, *Finite Size Effects on Helical Edge States in a Quantum Spin-Hall System*, Phys. Rev. Lett. **101**, 246807 (2008).

[49] H.-Z. Lu, W.-Y. Shan, W. Yao, Q. Niu, and S.-Q. Shen, *Massive Dirac fermions and spin physics in an ultrathin film of topological insulator*, Phys. Rev. B **81**, 115407 (2010).

[50] W.-Y. Shan, H.-Z. Lu, and S.-Q. Shen, *Effective continuous model for surface states and thin films of three-dimensional topological insulators*, New J. Phys. **12**, 043048 (2010).

[51] Y. Hatsugai, *Chern Number and Edge States in the Integer Quantum Hall Effect*, Phys. Rev. Lett. **71**, 3697 (1993).

[52] B. A. Bernevig, T. L. Hughes, and S.-C. Zhang, *Quantum Spin Hall Effect and Topological Phase Transition in HgTe Quantum Wells*, Science **314**, 1757–1761 (2006).

[53] M. König, S. Wiedmann, C. Brüne, A. Roth, H. Buhmann, L. W. Molenkamp, X.-L. Qi, and S.-C. Zhang, *Quantum Spin Hall Insulator State in HgTe Quantum Wells*, Science **318**, 766 (2007).

[54] M. König, H. Buhmann, L. W. Molenkamp, T. Hughes, C.-X. Liu, X.-L. Qi, and S.-C. Zhang, *The Quantum Spin Hall Effect: Theory and Experiment*, J. Phys. Soc. Jpn. **77**, 031007 (2008).

[55] P. R. Wallace, *The Band Theory of Graphite*, Phys. Rev. **71**, 622 (1947).

[56] N. M. R. Peres, *Colloquium: The transport properties of graphene: An introduction*, Rev. Mod. Phys. **82**, 2673–2700 (2010).

[57] R. S. Deacon, K.-C. Chuang, R. J. Nicholas, K. S. Novoselov, and A. K. Geim, *Cyclotron resonance study of the electron and hole velocity in graphene monolayers*, Phys. Rev. B **76**, 081406(R) (2007).

[58] E. V. Castro, K. S. Novoselov, S. V. Morozov, N. M. R. Peres, J. M. B. L. dos Santos, J. Nilsson, F. Guinea, A. K. Geim, and A. H. C. Neto, *Electronic Properties of a Biased Graphene Bilayer*, J. Phys. Condens. Matter **22**, 175503 (2010).

[59] K. S. Novoselov, E. McCann, S. V. Morozov, V. I. Fal'ko, M. I. Katsnelson, U. Zeitler, D. Jiang, F. Schedin, and A. K. Geim, *Unconventional Quantum Hall Effect and Berry's Phase of 2π in Bilayer Graphene*, Nat. Phys. **2**, 177–180 (2006).

[60] J. Nilsson, A. H. C. Neto, F. Guinea, and N. M. R. Peres, *Electronic properties of bilayer and multilayer graphene*, Phys. Rev. B **78**, 045405 (2008).

[61] E. McCann and M. Koshino, *The Electronic Properties of Bilayer Graphene*, Rep. Prog. Phys. **76**, 056503 (2013).

[62] E. V. Castro, K. S. Novoselov, S. V. Morozov, N. M. R. Peres, J. M. B. L. dos Santos, J. Nilsson, F. Guinea, A. K. Geim, and A. H. C. Neto, *Biased Bilayer Graphene: Semiconductor with a Gap Tunable by the Electric Field Effect*, Phys. Rev. Lett. **99**, 216802 (2007).

[63] T. Ihn, *Semiconductor Nanostructures* (Oxford University Press, 2010).

[64] M. Otteneder, "Terahertz magnetospectroscopy of HgTe-based heterostructure materials", PhD thesis (Universität Regensburg, 2021).

[65] K. Seeger, *Semiconductor Physics: An Introduction* (Springer, 2004).

[66] S. Hunklinger, *Festkörperphysik* (Oldenbourg Wissenschaftsverlag, 2009).

[67] W. Demtröder, *Experimentalphysik 3* (Springer Berlin Heidelberg, 2016).

[68] T. Numai, *Fundamentals of Semiconductor Lasers* (Springer-Verlag, 2004).

[69] C. Hamaguchi, *Basic Semiconductor Physics* (Springer-Verlag GmbH, Feb. 9, 2010).

[70] N. M. R. Peres, F. Guinea, and A. H. C. Neto, *Electronic properties of disordered two-dimensional carbon*, Phys. Rev. B **73**, 125411 (2006).

[71] A. M. Witowski, M. Orlita, R. Stepniewski, A. Wysmołek, J. M. Baranowski, W. Strupiński, C. Faugeras, G. Martinez, and M. Potemski, *Quasiclassical cyclotron resonance of Dirac fermions in highly doped graphene*, Phys. Rev. B **82**, 165305 (2010).

[72] M. L. Sadowski, G. Martinez, M. Potemski, C. Berger, and W. A. de Heer, *Landau Level Spectroscopy of Ultrathin Graphite Layers*, Phys. Rev. Lett. **97**, 266405 (2006).

[73] H. Plank, *Optoelectronic Phenomena Induced by Terahertz/infrared Laser Radiation in Topological Insulators and Graphene*, PhD thesis, University of Regensburg, 2018.

[74] V. I. Belinicher and B. I. Sturman, *The Photogalvanic Effect in Media Lacking a Center of Symmetry*, Phys. Usp. **23**, 199 (1980).

[75] P. Olbrich, L. E. Golub, T. Herrmann, S. N. Danilov, H. Plank, V. V. Bel'kov, G. Mussler, C. Weyrich, C. M. Schneider, J. Kampmeier, D. Grützmacher, L. Plucinski, M. Eschbach, and S. D. Ganichev, *Room-temperature High-frequency Transport of Dirac Fermions in Epitaxially Grown Sb_2Te_3- and Bi_2Te_3-based Topological Insulators*, Phys. Rev. Lett. **113**, 096601 (2014).

[76] B. I. Sturman and V. M. Fridkin, *The Photovoltaic and Photorefractive Effects in Non-centrosymmetric Materials* (Gordon and Breach Science Publishers, New York, 1992).

[77] W. Weber, L. E. Golub, S. N. Danilov, J. Karch, C. Reitmaier, B. Wittmann, V. V. Bel'kov, E. L. Ivchenko, Z. D. Kvon, N. Q. Vinh, A. F. G. van der Meer, B. Murdin, and S. D. Ganichev, *Quantum Ratchet Effects Induced by Terahertz Radiation in GaN-based Two-dimensional Structures*, Phys. Rev. B **77**, 245304 (2008).

[78] S. A. Tarasenko, *Direct Current Driven by Ac Electric Field in Quantum Wells*, Phys. Rev. B **83**, 035313 (2011).

[79] L. E. Golub and E. L. Ivchenko, *Shift Photocurrent Induced by Two-quantum Transitions*, Zh. Eksp. Teor. Fiz. **139**, 175–183 (2011).

[80] M. V. Durnev and S. A. Tarasenko, *Edge Photogalvanic Effect Caused by Optical Alignment of Carrier Momenta in Two-dimensional Dirac Materials*, Phys. Rev. B **103**, 165411 (2021).

[81] E. L. Ivchenko and G. E. Pikus, *Superlattices and Other Heterostructures* (Springer, 1997).

[82] P. M. Valov, B. S. Ryvkin, I. D. Yaroshetskii, and I. N. Yassievich, *Intraband Photoconductivity in N-type Ge Caused by Optical Heating of Electrons*, Fiz. Tekh. Poluprovodn. **5**, 904–910 (1971).

[83] D. A. Kozlov, Z. D. Kvon, E. B. Olshanetsky, N. N. Mikhailov, S. A. Dvoretsky, and D. Weiss, *Transport Properties of a 3D Topological Insulator Based on a Strained High-mobility HgTe Film*, Phys. Rev. Lett. **112**, 196801 (2014).

[84] D. Kozlov, D. Bauer, J. Ziegler, R. Fischer, M. Savchenko, Z. Kvon, N. Mikhailov, S. Dvoretsky, and D. Weiss, *Probing Quantum Capacitance in a 3D Topological Insulator*, Phys. Rev. Lett. **116**, 166802 (2016).

[85] C. R. Dean, A. F. Young, I. Meric, C. Lee, L. Wang, S. Sorgenfrei, K. Watanabe, T. Taniguchi, P. Kim, K. L. Shepard, and J. Hone, *Boron Nitride Substrates for High-quality Graphene Electronics*, Nat. Nanotechnol. **5**, 722 (2010).

[86] L. Wang, I. Meric, P. Y. Huang, Q. Gao, Y. Gao, H. Tran, T. Taniguchi, K. Watanabe, L. M. Campos, D. A. Muller, J. Guo, P. Kim, J. Hone, K. L. Shepard, and C. R. Dean, *One-dimensional Electrical Contact to a Two-dimensional Material*, Science **342**, 614 (2013).

[87] A. Sandner, T. Preis, C. Schell, P. Giudici, K. Watanabe, T. Taniguchi, D. Weiss, and J. Eroms, *Ballistic Transport in Graphene Antidot Lattices*, Nano Lett. **15**, 8402 (2015).

[88] K. Renk, *Basics of Laser Physics* (Springer, Berlin Heidelberg, 2012).

[89] G. W. Chantry, *Long-wave Optics : The Science and Technology of Infrared and Near-millimetre Waves* (Academic Press, London Orlando, 1984).

[90] P. Olbrich, "THz radiation induced spin polarized currents in low dimensionalsemiconductor structures", PhD thesis (University of Regensburg, 2010).

[91] S. D. Ganichev, *Tunnel Ionization of Deep Impurities in Semiconductors Induced by Terahertz Electric Fields*, Physica B **273-274**, 737–742 (1999).

[92] H. Fujiwara, *Spectroscopic Ellipsometry: Principles and Applications* (John Wiley and Sons, J, Chichester, UK, 2007).

[93] D. Meschede, *Gerthsen Physik, 22. Auflage* (Springer, Berlin, 2004).

[94] A. M. Shuvaev, G. V. Astakhov, G. Tkachov, C. Brüne, H. Buhmann, L. W. Molenkamp, and A. Pimenov, *Terahertz quantum Hall effect of Dirac fermions in a topological insulator*, Phys. Rev. B **87**, 121104(R) (2013).

[95] T. Herrmann, I. A. Dmitriev, D. A. Kozlov, M. Schneider, B. Jentzsch, Z. D. Kvon, P. Olbrich, V. V. Bel'kov, A. Bayer, D. Schuh, D. Bougeard, T. Kuczmik, M. Oltscher, D. Weiss, and S. D. Ganichev, *Analog of Microwave-induced Resistance Oscillations Induced in GaAs Heterostructures by Terahertz Radiation*, Phys. Rev. B **94**, 081301 (2016).

[96] G. Abstreiter, J. P. Kotthaus, J. F. Koch, and G. Dorda, *Cyclotron Resonance of Electrons in Surface Space-charge Layers on Silicon*, Phys. Rev. B **14**, 2480 (1976).

[97] T. K. L. K. W. Chiu and J. J. Quinn, *Quantum oscillations in screening in a two-dimensional electron gas*, Surf. Sci. **58** (1976).

[98] S. A. Mikhailov, *Microwave-induced Magnetotransport Phenomena in Two-dimensional Electron Systems: Importance of Electrodynamic Effects*, Phys. Rev. B **70**, 165311 (2004).

[99] Q. Zhang, T. Arikawa, M. A. Zudov, J. L. Reno, W. Pan, J. D. Watson, M. J. Manfra, and J. Kono, "Superradiant Decay of Coherent Cyclotron Resonance in Ultrahigh-Mobility Two-Dimensional Electron Gases", in CLEO: 2014 (2014).

[100] B. Wittmann, S. N. Danilov, V. V. Bel'kov, S. A. Tarasenko, E. G. Novik, H. Buhmann, C. Brüne, L. W. Molenkamp, Z. D. Kvon, N. N. Mikhailov, S. A. Dvoretsky, N. Q. Vinh, A. F. G. van der Meer, B. Murdin, and S. D. Ganichev, *Circular Photogalvanic Effect in HgTe/CdHgTe Quantum Well Structures*, Semicond. Sci. Technol. **25**, 095005 (2010).

[101] J. W. Matthews, *Defects associated with the accommodation of misfit between crystals*, J. Vac. Sci. Technol. A **12**, 126–133 (1975).

[102] B Pichaud, N Burle, M Putero-Vuaroqueaux, and C Curtil, *Low misfit systems as tools for understanding dislocation relaxation mechanisms in semiconducting heteroepitaxial films*, J. Phys.: Condens. Matter **14**, 13255–13267 (2002).

[103] R. France and A. J. Ptak, *Low-misfit epilayer analyses using in situ wafer curvature measurements*, J. Vac. Sci. Technol. B **29**, 03C115 (2011).

[104] Y. B. Bolkhovityanov, O. P. Pchelyakov, and S. I. Chikichev, *Silicon – germanium epilayers: physical fundamentals of growing strained and fully relaxed heterostructures*, Phys. Usp. **44**, 655–680 (2001).

[105] J. H. Basson and H. Booyens, *The introduction of misfit dislocations in HgCdTe epitaxial layers*, Phys. Status Solidi (a) **80**, 663–668 (1983).

[106] P. Ballet, C. Thomas, X. Baudry, C. Bouvier, O. Crauste, T. Meunier, G. Badano, M. Veillerot, J. P. Barnes, P. H. Jouneau, and L. P. Levy, *MBE Growth of Strained HgTe/CdTe Topological Insulator Structures*, J. Electron. Mater. **43**, 2955–2962 (2014).

[107] M. A. Berding, W. D. Nix, D. R. Rhiger, S. Sen, and A. Sher, *Critical thickness in the HgCdTe/CdZnTe system*, J. Electron. Mater. **29**, 676–679 (2000).

[108] Y. G. Sidorov, M. V. Yakushev, V. S. Varavin, A. V. Kolesnikov, E. M. Trukhanov, I. V. Sabinina, and I. D. Loshkarev, *Density of dislocations in CdHgTe heteroepitaxial structures on GaAs(013) and Si(013) substrates*, Phys. Solid State **57**, 2151–2158 (2015).

[109] S. Stachel, G. V. Budkin, U. Hagner, V. V. Bel'kov, M. M. Glazov, S. A. Tarasenko, S. K. Clowes, T. Ashley, A. M. Gilbertson, and S. D. Ganichev, *Cyclotron-resonance-assisted photon drag effect in InSb/InAlSb quantum wells excited by terahertz radiation*, Phys. Rev. B **89**, 115435 (2014).

[110] V. V. Bel'kov and S. D. Ganichev, *Magneto-gyrotropic Effects in Semiconductor Quantum Wells*, Semicond. Sci. Technol. **23**, 114003 (2008).

[111] V. Gantmakher and Y. Levinson, *Carrier Scattering in Metals and Semiconductors*, Modern Problems in Condensed Matter Sciences (Elsevier Science, Amsterdam, 2012).

[112] S. A. Tarasenko, *Electron Scattering in Quantum Wells Subjected to an In-plane Magnetic Field*, Phys. Rev. B **77**, 085328 (2008).

[113] N. S. Averkiev, L. E. Golub, and M Willander, *Spin relaxation anisotropy in two-dimensional semiconductor systems*, J. Phys.: Condens. Matter **14**, R271–R283 (2002).

[114] S. A. Tarasenko and E. L. Ivchenko, *Pure spin photocurrents in low-dimensional structures*, J. Exp. Theor. Phys. **81**, 231–235 (2005).

[115] E. L. Ivchenko and S. A. Tarasenko, *Monopolar Optical Orientation of Electron Spins in Bulk Semiconductors and Heterostructures*, J. Exp. Theor. Phys. **99**, 379–385 (2004).

[116] E. G. Novik, A. Pfeuffer-Jeschke, T. Jungwirth, V. Latussek, C. R. Becker, G. Landwehr, H. Buhmann, and L. W. Molenkamp, *Band Structure of Semimagnetic $Hg_{1-y}Mn_yTe$ Quantum Wells*, Phys. Rev. B **72**, 035321 (2005).

[117] M. Zholudev, F. Teppe, M. Orlita, C. Consejo, J. Torres, N. Dyakonova, M. Czapkiewicz, J. Wróbel, G. Grabecki, N. Mikhailov, S. Dvoretskii, A. Ikonnikov, K. Spirin, V. Aleshkin, V. Gavrilenko, and W. Knap, *Magnetospectroscopy of Two-dimensional HgTe-based Topological Insulators around the Critical Thickness*, Phys. Rev. B **86** (2012).

[118] S. Castilla, B. Terrés, M. Autore, L. Viti, J. Li, A. Y. Nikitin, I. Vangelidis, K. Watanabe, T. Taniguchi, E. Lidorikis, M. S. Vitiello, R. Hillenbrand, K.-J. Tielrooij, and F. H. L. Koppens, *Fast and Sensitive Terahertz Detection Using an Antenna-Integrated Graphene pn Junction*, Nano Lett. **19**, 2765–2773 (2019).

[119] H. Plank, J. Pernul, S. Gebert, S. N. Danilov, J. König-Otto, S. Winnerl, M. Lanius, J. Kampmeier, G. Mussler, I. Aguilera, D. Grützmacher, and S. D. Ganichev, *Infrared/terahertz Spectra of the Photogalvanic Effect in (Bi,Sb)Te Based Three-dimensional Topological Insulators*, Phys. Rev. Materials **2**, 024202 (2018).

[120] M. V. Durnev and S. A. Tarasenko, *High-frequency Nonlinear Transport and Photogalvanic Effects in 2D Topological Insulators*, Ann. Phys. **531**, 1800418 (2019).

[121] M. V. Durnev and S. A. Tarasenko, *Rectification of AC Electric Current at the Edge of 2d Electron Gas*, Phys. Status Solidi B **258**, 2000291 (2020).

[122] D. A. Bandurin, D. Svintsov, I. Gayduchenko, S. G. Xu, A. Principi, M. Moskotin, I. Tretyakov, D. Yagodkin, S. Zhukov, T. Taniguchi, K. Watanabe, I. V. Grigorieva, M. Polini, G. N. Goltsman, A. K. Geim, and G. Fedorov, *Resonant Terahertz Detection Using Graphene Plasmons*, Nat. Commun. **9**, 5392 (2018).

[123] M. Dyakonov and M. Shur, *Detection, Mixing, and Frequency Multiplication of Terahertz Radiation by Two-dimensional Electronic Fluid*, IEEE Trans. Electron Devices **43**, 380–387 (1996).

[124] K.-M. Dantscher, D. A. Kozlov, M. T. Scherr, S. Gebert, J. Bärenfänger, M. V. Durnev, S. A. Tarasenko, V. V. Bel'kov, N. N. Mikhailov, S. A. Dvoretsky, Z. D. Kvon, J. Ziegler, D. Weiss, and S. D. Ganichev, *Photogalvanic Probing of Helical Edge Channels in Two-dimensional HgTe Topological Insulators*, Phys. Rev. B **95**, 201103 (2017).

[125] R. R. Hartmann and M. E. Portnoi, *Optoelectronic Properties of Carbon-based Nanostructures: Steering Electrons in Graphene by Electromagnetic Fields* (LAP LAMBERT Academic Publishing, Saarbrucken, 2011).

[126] J. Li, L. Z. Tan, K. Zou, A. A. Stabile, D. J. Seiwell, K. Watanabe, T. Taniguchi, S. G. Louie, and J. Zhu, *Effective mass in bilayer graphene at low carrier densities: The role of potential disorder and electron-electron interaction*, Phys. Rev. B **94** (2016).

[127] C. Cobaleda, S. Pezzini, E. Diez, and V. Bellani, *Temperature- and Density-dependent Transport Regimes in a h-BN/bilayer Graphene/h-BN Heterostructure*, Phys. Rev. B **89**, 121404(R) (2014).

[128] G. V. Budkin and S. A. Tarasenko, *Ratchet Transport of a Two-dimensional Electron Gas at Cyclotron Resonance*, Phys. Rev. B **93**, 075306 (2016).

[129] J. C. Slonczewski and P. R. Weiss, *Band Structure of Graphite*, Phys. Rev. **109**, 272 (1958).

[130] J. W. McClure, *Band Structure of Graphite and De Haas-van Alphen Effect*, Phys. Rev. **108**, 612 (1957).

[131] M. S. Dresselhaus and G. Dresselhaus, *Intercalation Compounds of Graphite*, Adv. Phys. **51**, 1–186 (2002).

[132] S. Slizovskiy, A. Garcia-Ruiz, A. I. Berdyugin, N. Xin, T. Taniguchi, K. Watanabe, A. K. Geim, N. D. Drummond, and V. I. Fal'ko, *Out-of-Plane Dielectric Susceptibility of Graphene in Twistronic and Bernal Bilayers*, Nano Lett. (2021).

[133] D. S. L. Abergel and V. I. Fal'ko, *Optical and Magneto-optical Far-infrared Properties of Bilayer Graphene*, Phys. Rev. B **75**, 155430 (2007).

[134] V. I. Fal'ko and D. E. Khmel'nitskii, *Mesoscopic Photogalvanic Effect in Microjunctions*, Sov. Phys. JETP **68**, 1150 (1989).

[135] I. A. Dmitriev, A. D. Mirlin, D. G. Polyakov, and M. A. Zudov, *Nonequilibrium Phenomena in High Landau Levels*, Rev. Mod. Phys. **84**, 1709–1763 (2012).

[136] A. V. Muraviev, S. L. Rumyantsev, G. Liu, A. A. Balandin, W. Knap, and M. S. Shur, *Plasmonic and Bolometric Terahertz Detection by Graphene Field-effect Transistor*, Appl. Phys. Lett. **103**, 181114 (2013).

[137] M. Freitag, T. Low, W. Zhu, H. Yan, F. Xia, and P. Avouris, *Photocurrent in Graphene Harnessed by Tunable Intrinsic Plasmons*, Nat. Commun. **4**, 1951 (2013).

[138] A. C. Betz, F. Vialla, D. Brunel, C. Voisin, M. Picher, A. Cavanna, A. Madouri, G. Fève, J.-M. Berroir, B. Plaçais, and E. Pallecchi, *Hot Electron Cooling by Acoustic Phonons in Graphene*, Phys. Rev. Lett. **109**, 056805 (2012).

[139] J. N. Heyman, J. D. Stein, Z. S. Kaminski, A. R. Banman, A. M. Massari, and J. T. Robinson, *Carrier heating and negative photoconductivity in graphene*, J. Appl. Phys. **117**, 015101 (2015).

[140] V. Ryzhii, D. S. Ponomarev, M. Ryzhii, V. Mitin, M. S. Shur, and T. Otsuji, *Negative and positive terahertz and infrared photoconductivity in uncooled graphene*, Opt. Mater. Express **9**, 585 (2019).

[141] R. Jago, E. Malic, and F. Wendler, *Microscopic origin of the bolometric effect in graphene*, Phys. Rev. B **99**, 035419 (2019).

[142] T. Oka and H. Aoki, *Photovoltaic Hall effect in graphene*, Phys. Rev. B **79**, 081406(R) (2009).

[143] M. V. Durnev, *Photovoltaic Hall effect in the two-dimensional electron gas: Kinetic theory*, Phys. Rev. B **104**, 085306 (2021).

8 Acknowledgements

Finally, I would like to thank everyone who supported me on my way to this thesis.

Special thanks go to my doctoral supervisor Sergey, who gave me the fantastic opportunity to do my PhD. Thank you for your great support and your encouragement throughout the entire thesis. You were always open for discussion and created a great working atmosphere for which I am really grateful.

Many thanks go to Vanya for the theoretical support, enlightening discussions, and proofreading of my work. In addition, my thanks go to Sergey A. Tarasenko, Mikhail V. Durnev, Leonid E. Golub and Grigory V. Budkin from the Ioffe Institute in St. Petersburg for a great collaboration and theory support. I would also like to thank Jonathan Eroms, Robin Huber, and Tobias Rockinger for providing the graphene samples. Thank you for taking the time to answer transport related questions and helping me out with broken contacts. Representing all other group members, I want to thank Artem Mishchenko from Manchester University for providing the bi-layer graphene samples as well as for helpful discussions. On top of that I want to thank Sergey Slizovskiy and Vladimier Fal'ko for providing theoretical calculations and support. Further thanks go to our regularly visiting guests Dima Kozlov, Dima Kvon, Maxim Savchenko, Ivan Yahniuk and Vasily Bel'kov for useful discussions and support. Representing the whole HgTe growth group in Novosibirsk, my thanks go to Nikolai Mikhailov and Sergey Dvoretsky.

For the great time, my thanks go to Stefan, Max, Erwin and Marcel. Thank you for the fruitful discussions we had, the ice cream sessions, and the fun during trips and excursions. Thank you also for careful proofreading of my work. Likewise many thanks go out to Christian for the technical support during my lab works. Furthermore, kind and open-hearted thanks go to the alumni Helene, Tobi, Kathrin, and Philipp which were responsible for the great working atmosphere right from the beginning of my PhD. I also want to thank especially you, Helene, for handing over your knowledge to me. Furthermore, I want to thank the rest of our group members, Sergey Danilov, Philipp Euringer, Philip Soul, Anna Fuhrmann and Maximilian Stegerer. In addition, thanks go to my former bachelor and master students, Sonja Bernreuter, Tania Joetten, Anna Fuhrmann, Johannes Keil, and Anna Krinner for the productive time and good teamwork. For the great administrative help I want to thank Claudia Moser, Toni Siegmund, and Hannelore Lanz.

Moreover, I want to thank my whole family, especially my mother, who always supported and encouraged me to go my own way. At last but not least I want to thank my boyfriend Tom. Thank you so much for being my best friend, for always cheering me up and being by my side even in hard times.